



This is a repository copy of *The European Space Agency BIOMASS mission: Measuring forest above-ground biomass from space*.

White Rose Research Online URL for this paper:
<http://eprints.whiterose.ac.uk/148945/>

Version: Accepted Version

Article:

Qeegan, S. orcid.org/0000-0003-4452-4829, Le Toan, T., Chave, J. et al. (17 more authors) (2019) The European Space Agency BIOMASS mission: Measuring forest above-ground biomass from space. *Remote Sensing of Environment*, 227. pp. 44-60. ISSN 0034-4257

<https://doi.org/10.1016/j.rse.2019.03.032>

Article available under the terms of the CC-BY-NC-ND licence
(<https://creativecommons.org/licenses/by-nc-nd/4.0/>).

Reuse

This article is distributed under the terms of the Creative Commons Attribution-NonCommercial-NoDerivs (CC BY-NC-ND) licence. This licence only allows you to download this work and share it with others as long as you credit the authors, but you can't change the article in any way or use it commercially. More information and the full terms of the licence here: <https://creativecommons.org/licenses/>

Takedown

If you consider content in White Rose Research Online to be in breach of UK law, please notify us by emailing eprints@whiterose.ac.uk including the URL of the record and the reason for the withdrawal request.



eprints@whiterose.ac.uk
<https://eprints.whiterose.ac.uk/>

Sensing of Environment

Elsevier Editorial System(tm) for Remote

Manuscript Draft

Manuscript Number: RSE-D-18-01357R1

Title: The European Space Agency BIOMASS mission: measuring forest above-ground biomass from space

Article Type: Research Paper

Keywords: biomass, forest height, forest disturbance, carbon cycle, Pol-InSAR, polarimetry, tomographic SAR, P-band SAR, sub-surface imaging, unbiased DTM, icesheet and glacier motion, ionospheric effects

Corresponding Author: Professor Shaun Quegan,

Corresponding Author's Institution: University of Sheffield

First Author: Shaun Quegan

Order of Authors: Shaun Quegan; Thuy Le Toan; Jorgen Dall; Jerome Chave; Jean-Francois Exbrayat; Mauro Mariotti D'Alessandro; Philippe Paillou; Kostas Papathanassiou; Fabio Rocca; Sassan Saatchi; Klaus Scipal; hank Shugart; Luke Smallman; Maciej Soja; Stefano Tebaldini; Lars Ulander; Ludovic Villard; Dinh Ho Tong Minh, PhD; Mathew Williams; Mark Lomas, PhD

1 **The European Space Agency BIOMASS mission: measuring forest above-ground biomass from**
2 **space**

3

4 **Shaun Quegan¹, Thuy Le Toan², Jerome Chave³, Jorgen Dall⁴, Jean-François Exbrayat⁵, Dinh**
5 **Ho Tong Minh⁶, ~~Dinh Ho Tong Minh⁶~~, Mark Lomas¹, Mauro Mariotti D'Alessandro⁷, Philippe**
6 **Paillou⁸, Kostas Papathanassiou⁹, Fabio Rocca⁷, Sassan Saatchi¹⁰, Klaus Scipal¹¹, Hank**
7 **Shugart¹², T. Luke Smallman⁵, Maciej J. Soja¹³, Stefano Tebaldini⁷, Lars Ulander¹⁴, Ludovic**
8 **Villard² and Mathew Williams⁵**

9 1. University of Sheffield and National Centre for Earth Observation, UK

10 2. Centre d'Etudes Spatiales de la Biosphère, CNRS-CNES-Université Paul Sabatier-IRD,
11 Toulouse, France

12 3. Université Toulouse III Paul Sabatier, Laboratoire Evolution & Diversité Biologique, Toulouse,
13 France

14 4. Technical University of Denmark, National Space Institute, Denmark

15 5. University of Edinburgh, School of GeoSciences and National Centre for Earth
16 Observation, UK

17 6. UMR TETIS, IRSTEA, University of Montpellier, 34093 Montpellier, France

18 7. Dipartimento di Elettronica Informazione e Bioingegneria, Politecnico di Milano, Italy

19 8. Université de Bordeaux, Pessac Cedex, France

20 9. German Aerospace Center e.V. (DLR), Wessling, Germany

21 10. Jet Propulsion Laboratory, Pasadena, USA
22 10. Mission Science Division, ESA-ESTEC, the
Netherlands

23 11. Mission Science Division, ESA-ESTEC, the Netherlands

24 12. University of Virginia, Charlottesville, Virginia USA

25 13. MJ Soja Consulting, Hobart, Tasmania, Australia and University of Tasmania, Hobart,
26 Tasmania, Australia

27 14. Chalmers University of Technology, Sweden

28

29 Corresponding author

30 Shaun Quegan

31 School of Mathematics and Statistics

32 Hicks Building, University of Sheffield,

33 Hounsfield Rd

34 Sheffield S3 7RH

35 UK

36 Tel: +44 114 2223778

Fax: + 44 114 2223809

37 Email: s.quegan@sheffield.ac.uk

38

39 **Abstract**

40 The primary objective of the European Space Agency's 7th Earth Explorer mission, BIOMASS, is to
41 determine the worldwide distribution of forest above-ground biomass (AGB) in order to reduce the
42 major uncertainties in calculations of carbon stocks and fluxes associated with the terrestrial
43 biosphere, including carbon fluxes associated with Land Use Change, forest degradation and forest
44 regrowth. To meet this objective it will carry, for the first time in space, a fully polarimetric P-band
45 synthetic aperture radar (SAR). Three main products will be provided: global maps of both AGB and
46 forest height, with a spatial resolution of 200 m, and maps of severe forest disturbance at 50 m
47 resolution (where "global" is to be understood as subject to Space Object tracking radar restrictions).
48 After launch in 2022, there will be a 3-month commissioning phase, followed by a 14-month phase
49 during which there will be global coverage by SAR tomography. In the succeeding interferometric
50 phase, global polarimetric interferometry Pol-InSAR coverage will be achieved every 7 months up to
51 the end of the 5-year mission. Both Pol-InSAR and TomoSAR will be used to eliminate scattering
52 from the ground (both direct and double bounce backscatter) in forests. In dense tropical forests AGB
53 can then be estimated from the remaining volume scattering using non-linear inversion of a
54 backscattering model. Airborne campaigns in the tropics also indicate that AGB is highly correlated
55 with the backscatter from around 30 m above the ground, as measured by tomography. In contrast,
56 double bounce scattering appears to carry important information about the AGB of boreal forests, so
57 ground cancellation may not be appropriate and the best approach for such forests remains to be
58 finalized. Several methods to exploit these new data in carbon cycle calculations have already been
59 demonstrated. In addition, major mutual gains will be made by combining BIOMASS data with data
60 from other missions that will measure forest biomass, structure, height and change, including the
61 NASA Global Ecosystem Dynamics Investigation lidar deployed on the International Space Station
62 after its launch in December 2018, and the NASA-ISRO NISAR L- and S-band SAR, due for launch
63 in 2022. More generally, space-based measurements of biomass are a core component of a carbon
64 cycle observation and modelling strategy developed by the Group on Earth Observations. Secondary
65 objectives of the mission include imaging of sub-surface geological structures in arid environments,
66 generation of a true Digital Terrain Model without biases caused by forest cover, and measurement of

67 glacier and icesheet velocities. In addition, the operations needed for ionospheric correction of the
68 data will allow very sensitive estimates of ionospheric Total Electron Content and its changes along
69 the dawn-dusk orbit of the mission.

70

71 **1. Introduction: The role of biomass in the global carbon cycle and climate**

72 For millennia, humanity has depended on woody biomass from forests as a source of materials and
73 energy (Rackham and Moody, 1996; Radkau, 2012), and this dependence shows no sign of abating.
74 For example, around a third of the world’s population relies on biomass for energy, and in sub-
75 Saharan Africa around 81% of the energy use by households is provided by burning woody biomass
76 (World Bank, 2011). At the same time, forest, and its associated biomass, has often been treated as an
77 impediment to development, and huge tracts have been cleared, and continue to be cleared, to make
78 way for agriculture, pasture and agro-forestry (FAO, 2016). However, a significant shift in the
79 relationship between mankind and biomass has occurred as climate change has become of pressing
80 international concern and the role of forest biomass within this process has become clearer (IPCC,
81 2007, 2013).

82 Climate change is intimately connected with the global carbon balance and the fluxes of greenhouses
83 gases, especially carbon dioxide (CO₂), between the Earth’s surface and the atmosphere
84 (Intergovernmental Panel on Climate Change (IPCC), 2007, 2013). In particular, an unequivocal
85 indication of man’s effect on our planet is the accelerating growth of atmospheric CO₂. The principal
86 contribution (around 88%) to this growth is emissions from fossil fuel burning, with most of the
87 remainder arising from Land Use Change in the tropics (Le Quéré, 2018). However, the increase in the
88 concentration of atmospheric CO₂ between 2007 and 2016 is only about half (44%) of the emissions.
89 Because CO₂ is chemically inert in the atmosphere, the “missing” half of the emissions must flow back
90 into the Earth’s surface.

91 Current estimates (Le Quéré et al., 2018) suggest that around 28% of the total emissions are taken up
92 by the land and 22% by the oceans (leaving around 6% unaccounted for), but there are large

Formatted: Line spacing: Double

93 uncertainties in these values, especially the land uptake, whose value has usually been estimated as a
94 residual that ensures the total amount of carbon is conserved, as expressed in eq. (1):

95
$$U_{\text{land}} = E_{\text{ff}} + E_{\text{lb}} - (\Delta C_{\text{atmos}} + U_{\text{ocean}}). \quad (1)$$

96 Here E_{ff} denotes fossil fuel emissions; E_{lb} is net land biospheric emissions, comprising both Land Use
97 Change and ecosystem dynamics, and including alterations to biomass stocks linked to process
98 responses to climate change, nitrogen deposition and rising atmospheric CO_2 ; ΔC_{atmos} is the change in
99 atmospheric CO_2 ; and U_{land} and U_{ocean} are net average uptake by the land and ocean respectively. In eq.
100 (1) the quantities on the right-hand side are typically estimated on an annual basis or as a decadal
101 average, using a mixture of measurements and models, to yield U_{land} . However, in Le Quéré et al.
102 (2018) U_{land} is estimated independently using dynamic global vegetation models.

103 ~~Current estimates (Le Quéré et al., 2018) suggest that around 28% of the total emissions are taken up~~
104 ~~by the land and 22% by the oceans (leaving around 6% unaccounted for), but there are large~~
105 ~~uncertainties in these values, especially the land uptake, whose value has usually been estimated as a~~
106 ~~residual that ensures the total amount of carbon is conserved, as expressed in eq. (1):~~

107 ~~$$U_{\text{land}} = E_{\text{ff}} + E_{\text{lb}} - (\Delta C_{\text{atmos}} + U_{\text{ocean}}). \quad (1)$$~~

108 ~~Here E_{ff} denotes fossil fuel emissions; E_{lb} is net land biospheric emissions, comprising both Land Use~~
109 ~~Change and ecosystem dynamics, and including alterations to biomass stocks linked to process~~
110 ~~responses to climate change, nitrogen deposition and rising atmospheric CO_2 ; ΔC_{atmos} is the change in~~
111 ~~atmospheric CO_2 ; and U_{land} and U_{ocean} are net average uptake by the land and ocean respectively. In eq.~~
112 ~~(1) the quantities on the right hand side are typically estimated on an annual basis or as a decadal~~
113 ~~average, using a mixture of measurements and models, to yield U_{land} . However, in Le Quéré et al.~~
114 ~~(2018) U_{land} is estimated independently using dynamic global vegetation models. Under both~~

115 approaches U_{land} has the largest uncertainty of any term in eq. (1), estimated as 0.8 GtC/yr, which is
116 26% of its estimated value of 3.0 GtC/yr (1 GtC = 10^9 t of C which is equivalent to 3.67×10^9 t of CO_2).
117 Moreover, the Land Use Change flux (which is the difference between emissions from forest loss and
118 uptake of CO_2 by forest regrowth) has an uncertainty of 0.7 GtC/yr, which is 54% of its estimated

119 value of 1.3 GtC/yr. Since the fractional carbon content of dry biomass is around 50% (though with
120 significant inter-species differences [Thomas and Martin, 2012]), biomass change is a fundamental
121 component in these two land fluxes, controlling the emissions from forest disturbance and the uptake
122 of carbon by forest growth (e.g. Pan et al. 2011). This is why above-ground biomass (AGB) is
123 recognised as an Essential Climate Variable (ECV) within the Global Climate Observing System
124 (2015, 2017).

125 Climate change concerns have therefore made it imperative to obtain accurate estimates of biomass
126 and its changes. Unfortunately, where this information is most needed – the tropics – is where almost
127 no data have been gathered (Schimel et al., 2015). This is in contrast to forests in the temperate and
128 southern parts of the boreal zones whose economic importance has driven the development of
129 extensive national inventories (although there are vast areas of Alaska, Northern Canada, and East
130 Eurasia that do not have forest inventories because of their low economic importance).
131 ~~This is in contrast to forests in the temperate and southern parts of the boreal zones whose economic~~
132 ~~importance has driven the development of extensive national inventories (although there are vast areas~~
133 ~~of Alaska, Northern Canada, and East Eurasia that do not have forest inventories because of their low~~
134 ~~economic importance).~~The tropical forests cover an enormous area (~18 million km²) and offer huge
135 logistical challenges for ground-based biomass inventory. They are also crucial in political efforts to
136 mitigate climate change. In particular, the United Nations Convention on Climate Change (UNFCCC)
137 through its Reduction of Emissions from Deforestation and Degradation (REDD+) initiative
138 (UNFCCC, 2016) aims to use market and financial incentives to transfer funds from the developed
139 world to the developing countries in the tropical belt to help them reduce emissions by preservation
140 and management of their forests (UN-REDD Programme, 2008).

141 Estimates of biomass losses have focused on deforestation, i.e. conversion of forest land to other land
142 use, which results in complete removal of AGB. However, also significant, but missing from most
143 current estimates, is forest degradation. This is the loss of part of biomass, for instance removal of
144 large stems for timber or of understorey plants for replacement by cocoa, or through increased fire
145 along forest edges.

Formatted: Line spacing: Double

146 UN-REDD and related programmes have given significant impetus to the acquisition of more in situ
147 data in developing countries and this adds to the information available in the periodic reports of the
148 United Nations (UN) Food and Agriculture Organisation (FAO) (FAO 2006, 2010, 2016). However
149 national data in many cases have large gaps, sampling biases, inconsistency of methods, lack spatially
150 explicit information and contain unrepresentative samples, particularly in developing countries. As a
151 result, major efforts have been made to formulate more consistent global approaches that combine
152 forest inventory and satellite data to estimate AGB. Such endeavours have been greatly hampered by
153 the fact that, up until the launch of the Global Ecosystem Dynamics Investigation (GEDI) instrument
154 (see below), there has never been any spaceborne sensor designed to measure biomass, so space-based
155 estimates of biomass have relied on opportunistic methods applied to non-optimal sensors, with the
156 limitations this implies.

157 In the tropics, the most significant developments have been based on forest height estimates derived
158 from the Geoscience Laser Altimeter System (GLAS) onboard the Ice, Cloud and land Elevation
159 Satellite (ICESat) before its failure in 2009 (Lefsky, 2005, 2010). Combining GLAS data with other
160 EO and environmental datasets and in situ biomass measurements has led to the production of two
161 pan-tropical biomass maps (Saatchi et al. 2010; Baccini et al. 2012) at grid scales of 1 km and 500 m
162 respectively; differences between these maps and differences between the maps and in situ data are
163 discussed in Mitchard et al. (2013, 2014). Refinements of these maps have been produced by
164 Avitabile et al. (2016) and Baccini et al. (2017) based on essentially the same satellite datasets.

165 For boreal and temperate forests, methods have been developed to estimate Growing Stock Volume
166 (GSV, defined as the volume of wood in all living trees in an area with diameter at breast height above
167 a given threshold) from very long time series of C-band Envisat satellite radar data (Santoro et al.
168 2011). Multiplying these GSV estimates by wood density allowed Thurner et al. (2014) to estimate the
169 carbon stock of forests north of 30°N. Reliable GSV estimates using these methods are only possible
170 at spatial resolutions much coarser than the underlying radar data: by averaging to 0.5°, the relative
171 RMS difference between estimated GSV and reference data was consistently found to lie in the range
172 20–30% (Santoro et al. 2013). Further refinements to the methodology and its combination with

Formatted: Line spacing: Double

173 ALOS PALSAR-2 data are given in the Final Report of the ESA GlobBiomass project (Schmullius et
174 al., 2017).

175 L-band radar offers access to biomass values up to around 100 t/ha before losing sensitivity (e.g.
176 Mitchard et al., 2009). Under the JAXA Kyoto and Carbon Initiative, the ALOS L-band PALSAR-1
177 acquired a systematic five-year archive of forest data before its failure in April 2011 (Rosenqvist et
178 al., 2014). PALSAR-2 launched in spring 2014 and has continued this systematic acquisition strategy,
179 but current JAXA data policy makes scene data very expensive. Annual mosaics are freely available
180 and have been used to map woodland savanna biomass at continental scale (Bouvet et al., 2018), but
181 the mosaics combine data from different times and environmental conditions, so further processing
182 may be needed to exploit them for biomass estimation (Schmullius et al., 2017). L-band data will also
183 be acquired by the two Argentinian Microwave Observation Satellites (SAOCOM), the first of which
184 was launched on October 8, 2018, with the second due in 2019. Their main objectives are
185 measurements of soil moisture and monitoring of hazards, such as oil spills and floods, and their value
186 for global forest observations is not yet clear.

187 C-band (Sentinel-1, Radarsat) and X-band (Tandem-X) radar instruments are in orbit but at these
188 frequencies most of the backscatter is from the leaves and small twigs, so they have limited value for
189 biomass estimation except within the context of long time series at C-band (Santoro et al. 2011) and,
190 for TanDEM-X, when a ground Digital Terrain Model (DTM) is available and the height-to-biomass
191 allometry is robust (Persson et al., 2017; Askne et al., 2017).

192 ~~For boreal and temperate forests, methods have been developed to estimate Growing Stock Volume~~
193 ~~(GSV, defined as the volume of wood in all living trees in an area with diameter at breast height above~~
194 ~~a given threshold) from very long time series of C-band Envisat satellite radar data (Santoro et al.~~
195 ~~2011). Multiplying these GSV estimates by wood density allowed Thurner et al. (2014) to estimate the~~
196 ~~carbon stock of forests north of 30°N. Reliable GSV estimates using these methods are only possible~~
197 ~~at spatial resolutions much coarser than the underlying radar data: by averaging to 0.5°, the relative~~
198 ~~RMS difference between estimated GSV and reference data was consistently found to lie in the range~~
199 ~~20–30% (Santoro et al. 2013). Further refinements to the methodology and its combination with~~

200 ~~ALOS PALSAR 2 data are given in the Final Report of the ESA GlobBiomass project (Schmullius et~~
201 ~~al., 2017).~~

202 ~~L-band radar offers access to biomass values up to around 100 t/ha before losing sensitivity (e.g.~~
203 ~~Mitchard et al., 2009). Under the JAXA Kyoto and Carbon Initiative, the ALOS L-band PALSAR 1~~
204 ~~acquired a systematic five year archive of forest data before its failure in April 2011 (Rosenqvist et~~
205 ~~al., 2014). PALSAR 2 launched in spring 2014 and has continued this systematic acquisition strategy,~~
206 ~~but current JAXA data policy makes scene data very expensive. Annual mosaics are freely available~~
207 ~~and have been used to map woodland savanna biomass at continental scale (Bouvet et al., 2018), but~~
208 ~~the mosaics combine data from different times and environmental conditions, so further processing~~
209 ~~may be needed to exploit them for biomass estimation (Schmullius et al., 2017). L-band data will also~~
210 ~~be acquired by the two Argentinian Microwave Observation Satellites (SAOCOM), the first of which~~
211 ~~was launched on October 8, 2018, with the second due in 2019. Their main objectives are~~
212 ~~measurements of soil moisture and monitoring of hazards, such as oil spills and floods, and their value~~
213 ~~for global forest observations is not yet clear.~~

214 ~~C-band (Sentinel 1, Radarsat) and X-band (Tandem X) radar instruments are in orbit but at these~~
215 ~~frequencies most of the backscatter is from the leaves and small twigs, so they have limited value for~~
216 ~~biomass estimation except within the context of long time series at C-band (Santoro et al. 2011) and,~~
217 ~~for TanDEM X, when a ground Digital Terrain Model (DTM) is available and the height to biomass~~
218 ~~allometry is robust (Persson et al., 2017; Askne et al., 2017).~~

219 An exciting new development is the deployment on the International Space Station of the NASA
220 GEDI lidar instrument after its launch on December 5, 2018 (see Section 10). This mission aims to
221 sample forest vertical structure across all forests between 51.5° S and 51.5° N, from which estimates
222 of the mean and variance of AGB on a 1 km grid will be derived. In addition, ICESat-2 launched on
223 September 15, 2018; although it is optimised for icesheet, cloud and aerosol applications, and uses a
224 different technical approach from ICESat-1 based on photon counting, preliminary results suggest that
225 it can provide information on both forest height and structure.

226 It is against this scientific and observational background that BIOMASS was selected by the
227 European Space Agency (ESA) in 2013 as its 7th Earth Explorer mission, and the satellite is now
228 under production by a consortium led by Airbus UK for launch in 2022. The initial mission concept is
229 described in Le Toan et al. (2011), but there have been major developments since that time in almost
230 all aspects of the mission: the measurement and calibration concepts, the scientific context, the
231 methods to recover biomass from the satellite data, the exploitation of biomass in carbon cycle and
232 climate modelling, the availability of P-band airborne campaign data and high quality in situ data, and
233 the overall capability to estimate biomass from space. It is therefore timely to provide a
234 comprehensive description of the current mission concept, and this paper sets out to do so.

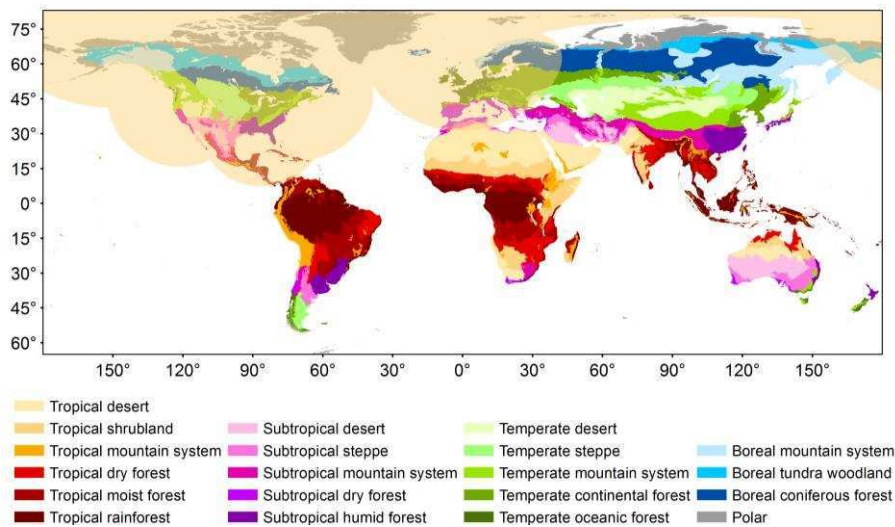
235 After a review of the mission objectives (Section 2), the associated measurement techniques
236 (polarimetry, polarimetric interferometry [Pol-InSAR] and SAR tomography [TomoSAR]) are
237 described in Section 3. Pol-InSAR and TomoSAR require the combination of multi-temporal stacks
238 of data; this imposes very strong conditions on the BIOMASS orbit pattern, with significant
239 consequences for the production of global biomass products (Section 4). The orbit pattern also
240 imposes strong requirements on the ability of the AGB and height inversion techniques, discussed in
241 Section 5, to adapt to changing environmental conditions. Section 6 deals with the use of BIOMASS
242 data to estimate severe forest disturbance, while Section 7 describes the development of the reference
243 datasets to be used for algorithm calibration and product validation. In Section 8 we discuss
244 developments in how BIOMASS data can be used to estimate key carbon cycle and climate variables.
245 Section 9 addresses a range of secondary objectives. Section 10 provides a view on how BIOMASS
246 complements other upcoming missions devoted to forest structure and biomass, in particular the
247 GEDI lidar and the NASA-ISRO NISAR L- and S-band mission. Finally, Section 11 discusses how
248 BIOMASS will contribute to an overall system for measuring biomass and its changes in the context
249 of a global carbon cycle management scheme and presents our general conclusions.

250 **2. BIOMASS mission objectives and data properties**

251 The primary objective of the BIOMASS mission is to determine the worldwide distribution of forest
252 above-ground biomass (AGB) in order to reduce the major uncertainties in calculations of carbon

253 stocks and fluxes associated with the terrestrial biosphere, including carbon fluxes associated with
 254 Land Use Change, forest degradation and forest regrowth. In doing so, it will provide support for
 255 international agreements such as REDD+ and UN Sustainable Development Goals (#13: climate
 256 action; #15: life on land). In addition it has several secondary objectives, including mapping sub-
 257 surface geology, measuring terrain topography under dense vegetation and estimating glacier and
 258 icesheet velocities (ESA, 2012).

259 Although BIOMASS aims at full global coverage, it will at least cover forested areas between 75° N
 260 and 56° S, subject to US Department of Defense Space Object Tracking Radar (SOTR) restrictions.
 261 These restrictions do not currently allow BIOMASS to operate within line-of-sight of the SOTR
 262 radars and mainly exclude the North American continent and Europe (Fig. 1, reproduced from
 263 Carreiras et al., 2017). For secondary applications, if global coverage is not possible, data will be
 264 collected on a best effort basis after covering the primary objectives, with priorities defined as in ESA
 265 (2015).



266
 267 **Fig. 1.** Global ecological regions of the world (FAO 2012) with the area affected by Space Objects
 268 Tracking Radar (SOTR) stations highlighted in yellow. Only land areas between 65° South and 85°
 269 North are represented (figure reproduced courtesy of Joao Carreiras).

270

271 The BIOMASS data product requirements to meet the primary mission objectives are (ESA, 2015):

- 272 1. Above-ground forest biomass (AGB), defined as the dry weight of live organic matter above
273 the soil, including stem, stump, branches, bark, seeds and foliage woody matter per unit area,
274 expressed in $t\ ha^{-1}$ (FAO, 2009). It does not include dead mass, litter and below-ground
275 biomass. Biomass maps will be produced with a grid-size of 200m x 200m (4 ha).
- 276 2. Forest height, defined as upper canopy height according to the H100 standard used in forestry
277 expressed in m, mapped using the same 4 ha grid as for biomass. H100 is defined as the
278 average height of the 100 tallest trees/ha (Philip, 1994).
- 279 3. Severe disturbance, defined as an area where an intact patch of forest has been cleared,
280 expressed as a binary classification of intact vs deforested or logged areas, with detection of
281 forest loss being fixed at a given level of statistical significance.

282 Further properties of these products are defined in Table 1. Note that:

- 283 • The biomass and height products will be produced on a 4 ha grid, while the disturbance
284 product is at the full resolution of the instrument after averaging to 6 looks in azimuth, i.e.,
285 around 50 m x 50 m, while the disturbance product is at the full resolution of the instrument
286 after averaging to 6 looks in azimuth, i.e., around 50 m x 50 m. This is because the large
287 changes in backscatter associated with forest clearance mean that disturbance can be detected
288 using less precise estimates of the polarimetric covariance and coherence matrices than are
289 needed for biomass and height estimation.
- 290 • If the true AGB exceeds $50\ t\ ha^{-1}$ then the RMS error (RMSE) of its estimate is expected to
291 depend on biomass and be less than $AGB/5$. For all values of $AGB < 50\ t\ ha^{-1}$ the RMSE is
292 stipulated to be $10\ t\ ha^{-1}$ or better, though it is likely that changes in ground conditions, such
293 as soil moisture, may cause the RMSE to increase beyond this value. Similarly, the RMSE of
294 estimates of forest height should be less than 30% of the true forest height for trees higher
295 than 10 m.

296 • Below-ground biomass cannot be measured by BIOMASS (or any other remote sensing
 297 instrument), but can be inferred from above-ground biomass using allometric relations
 298 combined with climate data (Cairn et al., 1997; Mokany et al., 2006; Thurner et al., 2014). In
 299 particular, Ledo et al. (2018) used an extensive tropical, temperate and boreal forest dataset to
 300 develop a regression, with just tree size and mean water deficit as predictor variables, which
 301 explains 62% of the variance in the root-to-shoot ratio. Therefore, throughout this paper,
 302 ‘biomass’ denotes ‘above-ground biomass’~~Below-ground biomass cannot be measured by~~
 303 ~~BIOMASS (or any other remote sensing instrument), but can be inferred from above-ground~~
 304 ~~biomass using allometric relations combined with climate data (Cairn et al., 1997; Mokany et~~
 305 ~~al., 2006; Thurner et al., 2014). In particular, Ledo et al. (2018) used an extensive tropical,~~
 306 ~~temperate and boreal forest dataset to develop a regression, with just tree size and mean water~~
 307 ~~deficit as predictor variables, which explains 62% of the variance in the root to shoot ratio.~~
 308 ~~Therefore, throughout this paper, ‘biomass’ denotes ‘above-ground biomass’.~~

309 **Table 1** Summary of primary BIOMASS Level 2 products. Achieving global coverage requires 425
 310 days during the initial Tomographic Phase and 228 days for each cycle of the subsequent
 311 Interferometric Phase. RMSE indicates Root Mean Square Error. “Global” is to be understood as
 312 subject to Space Object Tracking Radar restrictions (Carreiras et al., 2017).

313

Level 2 Product	Definition	Information Requirements
Forest biomass	Above-ground biomass expressed in $t\ ha^{-1}$.	<ul style="list-style-type: none"> • 200 m resolution • RMSE of 20% or $10\ t\ ha^{-1}$ for biomass $< 50\ t\ ha^{-1}$ • 1 biomass map every observation cycle • global coverage of forested areas
Forest height	Upper canopy height defined according to the H100 standard	<ul style="list-style-type: none"> • 200 m resolution • accuracy required is biome-dependent, but

		<p>RMSE should be better than 30% for trees higher than 10 m</p> <ul style="list-style-type: none"> • 1 height map every observation cycle • global coverage of forested areas
Severe disturbance	Map product showing areas of forest clearance	<ul style="list-style-type: none"> • 50 m resolution • detection at a specified level of significance • 1 map every observation cycle • global coverage of forested areas

314

315 **3. The BIOMASS system and measurement techniques**

316

317 BIOMASS will be a fully polarimetric SAR mission operating at P-band (centre frequency 435 MHz)
318 with 6 MHz bandwidth, as permitted by the International Telecommunications Union under a
319 secondary allocation (the primary allocation is to the SOTR system). The choice of P-band is
320 mandatory for measuring biomass with a single radar satellite (necessary for affordability within the
321 ESA cost envelope) for three main reasons (ESA, 2008, 2012; Le Toan et al., 2011):

322 1. P-band radiation can penetrate the canopy in all forest biomes and interacts preferentially with
323 the large woody vegetation elements in which most of the biomass resides;

324 2. Backscatter at P-band is more sensitive to biomass than at higher frequencies (X-, C-, S- and
325 L-bands); lower frequencies (e.g. VHF) display even greater sensitivity (Fransson et al.,
326 2000) but present formidable challenges for spaceborne SAR because of ionospheric
327 effects~~Backscatter at P-band is more sensitive to biomass than at higher frequencies (X-, C-,~~
328 ~~S- and L bands); lower frequencies (e.g. VHF) display even greater sensitivity (Fransson et~~
329 ~~al., 2000) but present formidable challenges for spaceborne SAR because of ionospheric~~
330 ~~effects;~~

331 3. P-band displays high temporal coherence between passes separated by several weeks, even in
332 dense forest (Ho Tong Minh et al., 2012), allowing the use of Pol-InSAR to estimate forest
333 height and retrieval of forest vertical structure using tomography.

334 Here (1) is the crucial physical condition: it underlies the sensitivity in point (2) and, through the
335 relative positional stability of the large woody elements, combined with the greater phase tolerance at
336 longer wavelengths, permits the long-term coherence needed for (3).

337 The satellite will carry a 12 m diameter reflector antenna, yielding a single-look azimuth resolution of
338 ~7.9 m. A polarimetric covariance product will also be generated by averaging 6 looks in azimuth,
339 giving pixels with azimuth resolution ~50 m. Because of the allotted 6 MHz bandwidth, the single-
340 look slant range resolution will be 25 m, equivalent to a ground range resolution of 59.2 m at an
341 incidence angle of 25°. Roll manoeuvres will allow the satellite to successively generate three sub-
342 swaths of width 54.32, 54.41 and 46.06 km, giving a range of incidence angles across the combined
343 swath from 23° to 33.9°. It will be in a sun-synchronous orbit with a near dawn-dusk (06:00 ± 15 min)
344 equatorial crossing time; the Local Time of the Ascending Node (LTAN) will be on the dawn-side,
345 the system will be left-looking and the orbit inclination will be 98°, with the highest latitude in the
346 northern hemisphere attained on the night-side. This orbit is chosen to avoid the severe scintillations
347 that occur in the post-sunset equatorial ionosphere (Rogers et al., 2013). Observations will be made
348 during both the ascending and descending passes.

349 BIOMASS displays major advances compared to all previous SAR missions in its use of three
350 complementary technologies to provide information on forest properties: polarimetry (PolSAR), Pol-
351 InSAR and TomoSAR. All acquisitions will be fully polarimetric, i.e. the amplitude and phase of the
352 HH, VV, HV & VH channels will be measured (HV indicates horizontal polarization on transmit and
353 vertical polarization on receive, with the other channels being similarly defined). This is in itself an
354 advance, but BIOMASS will also be the first mission to systematically employ the Pol-InSAR
355 technique to measure forest height. Even more innovative is its tomographic capability, which will
356 allow three-dimensional imaging of forests.

357 The Tomographic Phase will immediately follow the initial 3-month Commissioning Phase, and will
358 provide tomographic mapping of all imaged forest areas. Global coverage requires 425 days (~14
359 months) in order to provide 7 passes, each separated by 3 days, for each tomographic acquisition. The
360 remainder of the 5-year mission will be taken up by the Interferometric Phase, during which 3 passes,
361 each separated by 3 days, will be combined in 3-baseline Pol-InSAR. Each cycle of the
362 Interferometric Phase will require 228 days (~7 months) to provide global coverage. Note that these
363 techniques are nested: the data gathered for tomography will yield multiple Pol-InSAR and PolSAR
364 measurements, and each Pol-InSAR image triplet also provides three PolSAR images.

365 Associated with the highly innovative measurement concepts of the mission are completely new
366 challenges in external calibration arising from the orbital pattern needed for the tomographic and Pol-
367 InSAR phases of the mission (Section 4), the strong effects of the ionosphere at P-band, and the lack
368 of pre-existing P-band data except over very limited parts of the globe. Together these create
369 problems that can only be solved by combining infrequent visits to instrumented calibration sites with
370 systematic exploitation of the properties of distributed targets and targets of opportunity. An overall
371 approach to addressing these problems, including ionospheric correction, radiometric and polarimetric
372 calibration, and providing the required geolocation accuracy is described in Quegan et al. (2018).

373 **4. The BIOMASS orbit and its implications**

374 In the Tomographic Phase, BIOMASS needs to be placed in a very precise repeat orbit in which a
375 given scene is imaged 7 times with 3-day spacing. These acquisitions will be from slightly different
376 positions separated by 15% of the critical baseline (i.e. 0.823 km) at the equator, which is necessary to
377 preserve coherence. In this orbit, it takes 18 days to acquire the 7 images needed for each of the 3 sub-
378 swaths, so that tomography over the full swath (comprising the 3 sub-swaths) occupies a period of 60
379 days. Once this has been achieved, a drift manoeuvre will raise the satellite in altitude and then return
380 it to its nominal altitude of 671.9 km. This allows the Earth to rotate below the satellite, and the next
381 tomographic acquisition period covers a new swath that is adjacent to the previous one. Repeating this
382 sequence $6 + 1/3$ times yields global coverage and takes 425 days (the extra third corresponds to
383 coverage in swath 1). The orbit pattern for the Interferometric Phase uses essentially the same

384 concept, but because only 3 images are needed to form the Pol-InSAR product, imaging a full swath
385 requires only 24 days, and global coverage takes 228 days.

386 These properties of the BIOMASS orbit pattern, driven by the requirement for global coverage using
387 coherent imaging techniques, have profound implications for biomass retrieval in time and space.

388 Acquisitions in adjacent swaths are separated by 2 months in the Tomographic Phase and by a little
389 less than a month in each cycle of the Interferometric Phase. Hence there are likely to be significant
390 changes in environmental conditions between different swaths that make up the global coverage. In
391 addition, because each cycle of the Interferometric Phase takes 7 months, the acquisitions become
392 steadily more out of phase with annual geophysical cycles, such as the Amazonian and West African

393 inundation cycles. This means that the BIOMASS inversion algorithms have to be sufficiently robust
394 that they are negligibly affected by environmental changes~~This means that the BIOMASS inversion~~
395 ~~algorithms have to be sufficiently robust that they are negligibly affected by environmental changes.~~

Formatted: Font: 11 pt

396 Incomplete compensation for such changes will manifest themselves as systematic differences
397 between adjacent swaths or repeat swaths gathered in different cycles. As an example, boreal forests
398 freeze during winter and their backscatter significantly decreases, so the winter season will most
399 likely not be useful for biomass estimation.

400

401 **5. Forest AGB and height estimation techniques**

402

403 BIOMASS will exploit properties of all three SAR techniques, PolSAR, Pol-InSAR and TomoSAR,
404 to estimate biomass, while both Pol-InSAR and TomoSAR will provide estimates of forest height.

405 However, because BIOMASS will be the first spaceborne P-band SAR, the experimental data needed
406 to support the development and testing of these techniques is based on limited airborne and ground-

407 based measurements. Six major ESA airborne campaigns were carried out (BioSAR-1, -2 and -3 in
408 the boreal zone, and three in tropical ecosystems: TropiSAR in French Guiana, AfriSAR in Gabon

409 and Indrex-2 in Indonesia) using the E-SAR and F-SAR (DLR, Germany) and SETHI (ONERA,
410 France) P-band SARs (see Table 2, which includes the objectives of the campaigns and essential

411 properties of the test-sites). These campaigns have provided the most accurate and complete set of P-
 412 band SAR (PolSAR, Pol-InSAR and TomoSAR) and associated in situ data currently available over
 413 boreal and tropical forests. In addition, long-term continuous P-band tower-based measurements were
 414 made in French Guiana (Tropiscat), Ghana (Afriscat) and Sweden (Borealscat) to investigate diurnal
 415 and seasonal variations in backscatter and temporal coherence. Earlier P-band datasets from the
 416 NASA AirSAR system were also helpful, especially tropical forest data from Costa Rica, to extend
 417 the range of tropical biomass values (Saatchi et al., 2011), and NASA was heavily involved in the
 418 AfriSAR campaign, providing lidar coverage of the AfriSAR test-sites (Labrière et al., 2018). No
 419 specific ESA campaigns were conducted in temperate forests, but substantial amounts of tomographic
 420 data are available for such forests from experimental campaigns carried out by DLR.

421 **Table 2** Campaign data used in developing and testing BIOMASS retrieval algorithms.

422

Campaign	Objectives	Test sites	Time	Forest conditions
TropiSAR, SETHI (Dubois-Fernandez et al., 2012)	Biomass estimation in tropical forest; temporal stability of coherence	Paracou & Nouragues, French Guiana	Aug. 2009	Tropical rain forest, AGB 300-500 t/ha, lowland and hilly terrain
Indrex-2, E-SAR (Hajnsek et al., 2009a) ; not tomographic	Height retrieval in tropical forest ; measurement of repeat-pass temporal decorrelation	Sungai-Wai & Mawas, Borneo, Indonesia	Nov. 2004	Tropical rain forest. Sungai-Wai: lowland, AGB \leq 600 t/ha; Mawas: peat swamp, AGB \leq 200 t/ha
Tropiscat: Ground-based high temporal resolution	Measurement of long-term temporal coherence and	Paracou, French Guiana	Aug. 2011 - Dec. 2012	Tropical rain forest, AGB ca. 400 t/ha

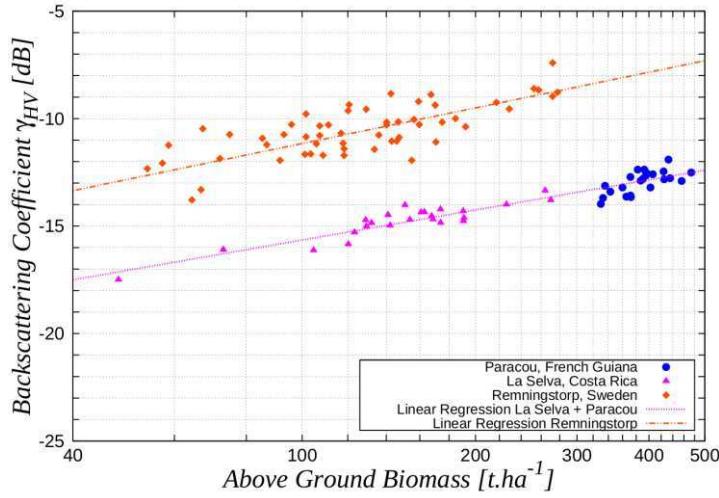
measurements (Koleck et al., 2012)	temporal variation of backscatter in tropical forest			
BioSAR-1, E-SAR (Hajsek et al., 2008)	Biomass estimation and measurement of multi-month temporal decorrelation	Remningstorp, southern Sweden	Mar. - May 2007	Hemi-boreal forest, low topography, AGB ≤ 300 t/ha
BioSAR-2, E-SAR (Hajsek et al., 2009b)	Topographic influence on biomass estimation	Krycklan, northern Sweden	Oct. 2008	Boreal forest, hilly, AGB ≤ 300 t/ha
BioSAR-3, E-SAR (Ulander et al., 2011a, b)	Forest change and multi-year coherence relative to BioSAR-1	Remningstorp, southern Sweden	Sept. 2010	Hemi-boreal forest, low topography, AGB ≤ 400 t/ha (more high biomass stands than in BIOSAR-1)
AfriSAR, SETHI and F-SAR	Biomass estimation in tropical forest; temporal stability of coherence	Sites at Lopé, Mondah, Mabounie and Rabi, Gabon	July 2015 (SETHI) Feb. 2016 (F-SAR)	Tropical forest and savannah, AGB from 50 to 500 t/ha
Afriscat: Ground- based high temporal resolution measurements	Measurement of long-term temporal coherence and temporal variation of backscatter in	Ankasa, Ghana	July 2015 - July 2016	Tropical forest, low topography, AGB from 100 to 300 t/ha

	tropical forest			
Borealscat: Ground-based high temporal resolution measurements (Ulander et al., 2018; Monteith and Ulander, 2018)	Time series of backscatter, tomography, coherence and environmental parameters in boreal forest.	Remningstorp, southern Sweden	Dec. 2016, ongoing	Hemi-boreal forest, spruce-dominated stand, low topography, AGB = 250 t/ha

423

424 **5.1 Estimating AGB**

425 Some key findings from these campaigns are illustrated in Fig. 2, where the P-band HV backscatter
426 (given as γ^0 in dB) is plotted against the biomass of reference plots from a boreal site (Remningstorp,
427 Sweden) and two tropical sites (Paracou, French Guiana and La Selva, Costa Rica). The data are not
428 corrected for topographic or soil moisture effects, and the lines correspond to linear regression fits to
429 the log-log form of the data. The sensitivity of backscatter to biomass is clear across the whole range
430 of biomass covered, though with large dispersion in the boreal forest and the high biomass tropical
431 forest in French Guiana. Also clear is that, for a given biomass, the HV backscatter is considerably
432 larger in boreal than tropical forest. This corrects an error in Fig. 2 of Le Toan et al. (2011) where
433 mean backscatter differences between the boreal and tropical data were ascribed to calibration errors
434 and removed by shifting the data. The careful calibration of the datasets shown in Fig. 2 indicates that
435 the difference is real and that different physical and biological factors (such as forest structure) are at
436 play in the different forest types.



437

438 **Fig. 2.** P-band backscatter at HV polarisation (γ_{HV}^0) over tropical and boreal forests against the
 439 biomass of in situ reference plots. Data from Paracou, French Guiana, were acquired by the SETHI
 440 SAR system in 2011 (Dubois-Fernandez et al., 2012), those from La Selva, Costa Rica, in 2004 by the
 441 AIRSAR system (Antonarakis et al., 2011) and those from Remningstorp, Sweden, by the E-SAR
 442 system in 2007 (Sandberg et al., 2011).

443

444 The regression lines indicate that in natural units the HV backscatter is approximately related to
 445 biomass, W , by a power law relationship, i.e.

$$446 \quad \gamma_{HV}^0 = cW^p \quad (2)$$

447 where c and p are parameters. Analysis in Schlund et al. (2018) indicates such relationships are found
 448 for the full set of available P-band SAR datasets that are supported by adequate in situ data except
 449 where there is strong topography. Although the model coefficients (and their coefficients of
 450 determination) vary across datasets, they are not significantly different when similar AGB ranges are
 451 considered.

452 Despite this strong regularity in the relation between HV backscatter and biomass, exploiting it to
 453 estimate biomass faces a number of problems:

454 **a. Dispersion in the data.** For the boreal data in Fig. 2, major factors causing dispersion in the
455 backscatter values are slope and soil moisture variations. The Krycklan campaign over boreal
456 forest in Sweden (Table 2) clearly shows that topography severely affects the power law
457 relationship given by eq. (2) (Soja et al., 2013)~~The Krycklan campaign over boreal forest in~~
458 ~~Sweden (Table 2) clearly shows that topography severely affects the power law relationship given~~
459 ~~by eq. (2) (Soja et al., 2013).~~ This is particularly obvious in Krycklan because in this region most
460 of the highest biomass stands are located in sloping areas. As demonstrated in Soja et al. (2013),
461 however, adding terms involving the $\gamma_{HH}^0/\gamma_{VV}^0$ ratio and slope to the regression significantly
462 reduces the dispersion, at the expense of including two extra parameters. Note that the HH/VV
463 ratio was included because of its lower sensitivity to soil moisture, and that the regression inferred
464 from the Krycklan site in N. Sweden could be successfully transferred to Remningstorp 720 km
465 away in S. Sweden. The associated relative RMSEs in AGB using the combined BioSAR-1 and -2
466 data were 27% (35 t/ha) or greater at Krycklan and 22% (40 t/ha) or greater at Remningstorp.
467 However, more recent unpublished analysis including the BIOSAR-3 data indicates that further
468 coefficients are needed to achieve adequate accuracy. Another study for Remningstorp (Sandberg
469 et al., 2014) found that AGB change could be estimated more accurately than AGB itself: analysis
470 based on 2007 and 2010 data gave a RMSE of 20 t/ha in the estimated biomass change, i.e.
471 roughly half the RMSEs of the individual AGB estimates. The algorithm used was based on
472 finding areas of little or no change using the HH/VV ratio and applying polarization-dependent
473 correction factors to reduce the effect of moisture variation.

474 Unlike in Sweden, very little environmental change occurred during the TropiSAR campaign in
475 French Guiana, and the major effect affecting the relation given by eq. (2) was topography, which
476 greatly increased the dispersion. Methods to reduce this were based on rotating the spatial axes
477 and normalization to account for the variation in the volume and double bounce backscatter with
478 incidence angle (Villard and Le Toan, 2015). This allowed the sensitivity of the HV backscatter to
479 biomass to be recovered, and AGB could then be estimated from the polarimetric data with
480 relative RMSE < 20%. However, because the approach is based on regression and there was little
481 temporal change in conditions during the campaign, it contains no provision for dealing with large

482 seasonal variations in backscatter like those observed in the Tropiscat data (Bai et al., 2018) and
483 expected in BIOMASS data.

484 **b. Algorithm training.** Regression methods need training data, but in many parts of the world, and
485 especially in the tropics, there are very few high quality permanent in situ sampling plots, almost
486 all funded under science grants. Significant efforts are being made by ESA, in collaboration with
487 NASA, to work with and extend the existing in situ networks in order to establish a set of well-
488 documented reference sites that could be using for training and validation. Part of the challenge in
489 doing so is to ensure that the set of reference sites is large enough and representative enough to
490 capture the major variations in forest types and conditions.

491 **c. Physical explanation.** Despite its remarkable generality, as demonstrated in Schlund et al.
492 (2018), the physical basis of eq. (2) is not well-understood except in certain limiting cases (see
493 below). Hence it is essentially empirical and at present we cannot in general attach meaningful
494 physical properties to the fitting parameters or derive them from scattering models. In particular,
495 it has no clear links to well-known decompositions of polarimetric backscatter into physical
496 mechanisms (e.g. Freeman and Durden (1998); Cloude and Pottier (1996)). In addition, in boreal
497 forests this relation depends on both total AGB and tree number density, so that unambiguous
498 estimates of AGB require information on number density or use of height information combined
499 with height- biomass allometric relations (Smith-Jonforsen et al., 2007)

500 To get round these problems with the regression-based approaches, the current emphasis is on
501 estimating biomass using a model-based approach that brings together three key factors: the
502 capabilities of the BIOMASS system, the observed properties of the vertical distribution of forest
503 biomass and our knowledge about the physics of radar-canopy interactions as embodied in scattering
504 models.

505 Its starting point is a simplified scattering model that describes the backscattering coefficient in each
506 of the HH, HV and VV channels as an incoherent sum of volume, surface and double-bounce
507 scattering (Truong-Loi et al., 2015). The model involves 6 real parameters per polarization, which are
508 estimated using a combination of a scattering model and reference data. Biomass, soil roughness and

509 soil moisture are then treated as variables to be estimated from the data. Initial analysis found that this
 510 model was too complex and the associated parameter estimation was too unstable for this to be a
 511 viable approach for BIOMASS. However, a crucial technical development was to demonstrate that
 512 both tomographic and Pol-InSAR data can be used to cancel out the terms involving the ground
 513 (surface scatter and double bounce) and isolate the volume scattering term (Mariotti d'Alessandro et
 514 al., 2013; Mariotti d'Alessandro et al., 2018). In the Truong-Loi et al. (2015) formulation, this term
 515 can be written as

$$516 \quad \sigma_{pq}^v = A_{pq} W^{\alpha_{pq}} \cos \theta \left(1 - \exp \left(-\frac{B_{pq} W^{\beta_{pq}}}{\cos \theta} \right) \right) \quad (3)$$

517 where A_{pq} , B_{pq} , α_{pq} and β_{pq} are coefficients for polarization configuration pq, W is AGB, and θ is
 518 the local incidence angle. The coefficients α_{pq} and β_{pq} relate to forest structure, $B_{pq} > 0$ is an
 519 extinction coefficient and $A_{pq} > 0$ is a scaling factor.

520 Assuming that A_{pq} , B_{pq} , α_{pq} and β_{pq} are space-invariant at a certain scale, these parameters and
 521 AGB can be estimated simultaneously from the measured values of σ_{pq}^v in the three polarizations, pq
 522 = HH, HV and VV, using a non-linear optimization scheme (Soja et al., 2017, 2018). However, in
 523 model (3), the two biomass-dependent factors, $A_{pq} W^{\alpha_{pq}}$ and $1 - \exp \left(-\frac{B_{pq} W^{\beta_{pq}}}{\cos \theta} \right)$, both increase
 524 with increasing AGB for realistic parameters ($\alpha_{pq} > 0$ and $\beta_{pq} > 0$), so interactions between
 525 α_{pq} , B_{pq} and β_{pq} render the inversion difficult. This problem can be mitigated by using two special
 526 cases of the model, both of which lead to a power law expression as in eq. (2). For the low-attenuation
 527 case, i.e., $B_{pq} W^{\beta_{pq}} \ll 1$, eq. (3) can be simplified using a series expansion to:

$$528 \quad \sigma_{pq}^v = A' W^p \quad (4)$$

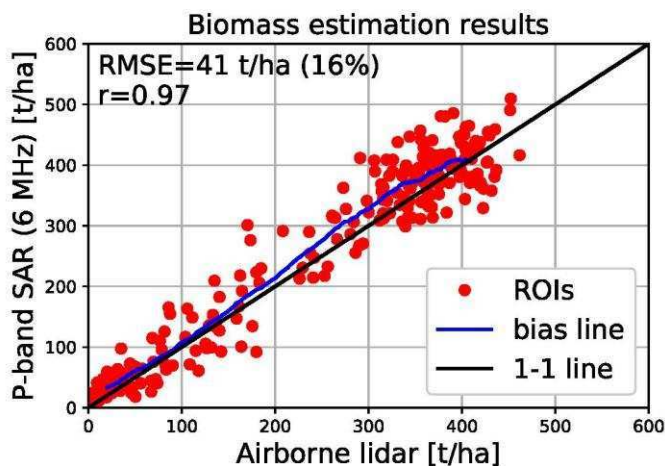
529 where $p = \alpha_{pq} + \beta_{pq}$ and $A' = A_{pq} B_{pq}$, and in the high-attenuation case, i.e., $B_{pq} W^{\beta_{pq}} \gg 1$, eq. (3)
 530 can be simplified to:

$$531 \quad \sigma_{pq}^v = A' W^p \cos \theta \quad (5)$$

532 where $p = \alpha_{pq}$ and $A' = A_{pq}$. In both cases, A' , W and p can then be estimated using the scheme
 533 proposed in Soja et al. (2017, 2018).

534 Note that there is still an inherent scaling ambiguity since the scheme cannot distinguish the unbiased
535 estimate of AGB, W_0 , from any function of the form aW_0^b , where a and b are calibration constants.
536 Hence reference data are needed, but these data do not need to cover a wide range of backscatter,
537 slope and incidence angle conditions, as would be required if any of the models (3) - (5) were to be
538 trained directly. One complication is that the temporal and spatial variations of a and b are
539 currently unknown and further work is needed to quantify them. Further refinements may also be
540 needed to reduce residual effects from moisture variations by, for example, use of the VV/HH ratio in
541 boreal forests as discussed above.

542 The effectiveness of this approach is illustrated by Fig. 3, which plots values of AGB estimated with
543 this scheme against AGB values estimated from in situ and airborne laser scanning data for a set of
544 200 m x 200 m regions of interest (ROIs). The airborne P-band data used are from the AfriSAR
545 campaign and were filtered to 6 MHz to match the BIOMASS bandwidth. The estimates are highly
546 correlated with the reference data ($r = 0.97$), exhibit only a small amount of bias across the whole
547 biomass range, and give a RMSE of 41 t/ha (16% of the average biomass).



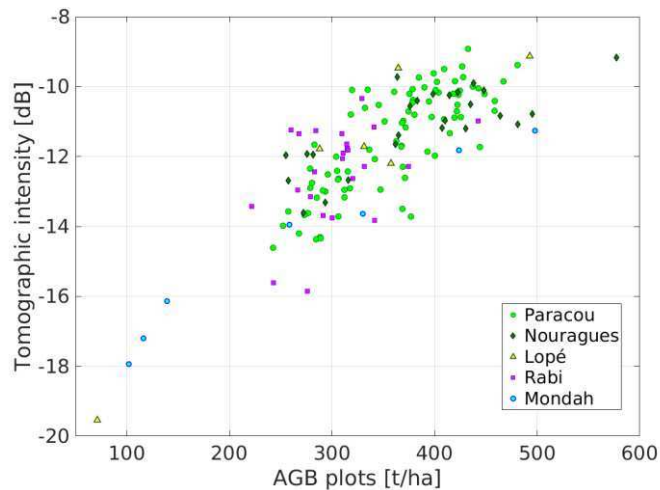
548

549 **Fig. 3.** Estimated AGB using the approach described in the text against AGB estimated from in situ
550 and airborne laser scanning at the La Lopé site in Gabon during the AfriSAR campaign. The running
551 average given by the blue line indicates only a small positive bias across the whole range of AGB.
552 ROI denotes Region of Interest.

553 Further confirmation of the importance of isolating the volume backscatter by using the full power of
554 tomography is from the TropiSAR tropical forest campaign, where the tomographic intensity (in dB)
555 measured at 30 m above the ground (representing scattering from canopy elements between ca. 17.5
556 m and 42.5 m, given the roughly 25 m vertical resolution of tomographic imaging) was found to be
557 highly correlated with AGB (Ho Tong Minh et al., 2014, 2016). The observed sensitivity is about 50
558 tons/ha per dB, and the correlation coefficient is about 0.84 at the scale of 1 ha. This striking result
559 has been replicated in the forest sites investigated during the AfriSAR campaign (Fig. 4), and suggests
560 that the backscatter from the forest layer centred 30 m above ground should be strongly correlated
561 with total AGB in the case of dense tropical forests.

562 Importantly, this finding is consistent with the TROLL ecological model (Chave, 1999), which
563 predicts that for dense tropical forests the fraction of biomass contained between 20 m and 40 m
564 accounts for about 35% to 40% of the total AGB, and that this relation is stable over a large range of
565 AGB values (Ho Tong Minh et al., 2014). Another element in support of the ecological relevance of
566 the 30 m layer is provided by two recent studies of tropical forests, which observed that: a) correlation
567 between AGB and the area occupied at different heights by large trees (as derived from lidar) is
568 maximal at a height of about 30 m (Meyer et al., 2017); b) about 35% of the total volume tends to be
569 concentrated at approximately 24-40 m above the ground (Tang, 2018).

570 However, tomographic data will only be available in the first phase of the mission. In addition,
571 exploiting the relation between AGB and the 30 m tomographic layer requires knowledge of how the
572 regression coefficients vary in time and space, hence substantial amounts of training data. In contrast,
573 ground cancellation can be carried out with both tomographic and Pol-InSAR data (so throughout the
574 mission). This allows the volume scattering term (eq. (3)) to be isolated and hence AGB to be
575 estimated using the scheme described in Soja et al. (2018), which makes much less demand on the
576 availability of reference data.



577

578 **Fig. 4.** Plot of HV backscatter intensity at height 30 m above the ground measured by tomography
 579 against in situ AGB in 1 ha plots at tropical forest sites investigated during the TropiSAR (Paracou
 580 and Nouragues) and AfriSAR (Lopé, Rabi, Mondah) campaigns.

581

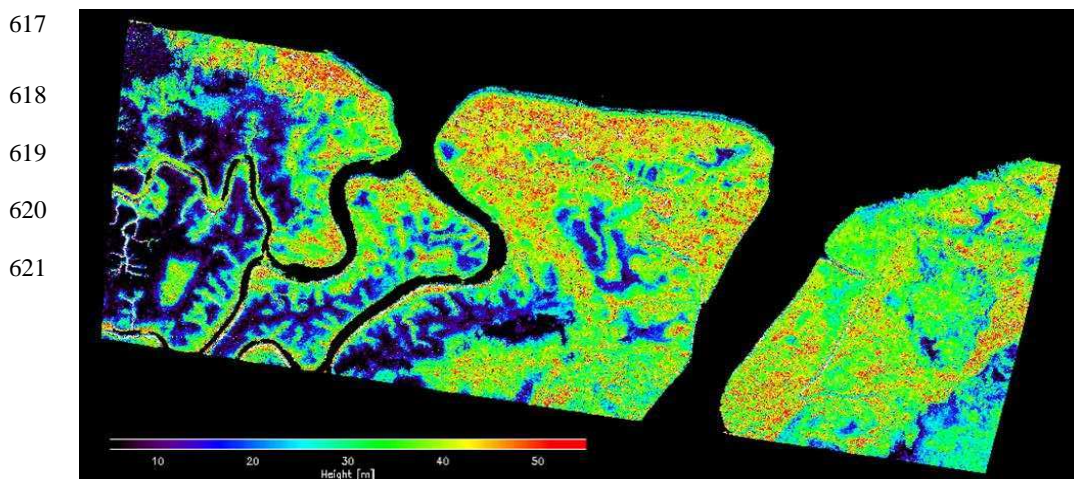
582 The value of tomography for estimating AGB in boreal and temperate forests is less clear, since (a)
 583 these forests in general have smaller heights than in the tropics (so it is more problematical to isolate
 584 the signal from a canopy layer without corruption by a ground contribution, given the roughly 25 m
 585 vertical resolution of the tomographic product from BIOMASS), and (b) the double bounce
 586 mechanism appears to be important in recovering the AGB of boreal forests. Hence ground
 587 cancellation (which also cancels double bounce scattering, since this appears at ground level in the
 588 tomographic image) may not help biomass estimation in such forests, and the preferred algorithm for
 589 BIOMASS in these cases is still not fixed. Recent results indicate that ground cancellation improves
 590 results in Krycklan, but not in Remningstorp, most likely because it suppresses direct ground
 591 backscattering, which is unrelated to AGB but is of higher relative importance in Krycklan due to the
 592 pronounced topography.

593

594 **5.2 Estimating forest height**

595 Forest height estimates will be available throughout the Tomographic and Interferometric Phases, in
596 the latter case using polarimetric interferometric (Pol-InSAR) techniques (Cloude and Papathanassiou,
597 1998, 2003; Papathanassiou and Cloude, 2001) applied to three polarimetric acquisitions performed in
598 a 3-day repeat-pass interferometric mode. The use of Pol-InSAR to estimate forest height has been
599 demonstrated at frequencies from X- to P-band for a variety of temperate, boreal and tropical sites,
600 with widely different stand and terrain conditions (Praks et al., 2007; Kugler et al., 2014; Hajnsek et
601 al., 2009; Garestier et al., 2008), and several dedicated studies have addressed its likely performance
602 and limitations when applied to BIOMASS data.

603 Estimation of forest height from Pol-InSAR requires a model that relates forest height to the Pol-
604 InSAR measurements (i.e. primarily to the interferometric coherence at different polarisations and for
605 different spatial baselines) together with a methodology to invert the established model. Most of the
606 established inversion algorithms use the two-layer Random Volume over Ground (RVoG) model to
607 relate forest height to interferometric coherence (Treuhaft et al., 1996). This relies on two
608 assumptions: 1) all polarizations “see” (up to a scalar scaling factor) the same vertical distribution of
609 scatterers in the vegetation (volume) layer; 2) the ground layer is impenetrable, i.e. for all
610 polarizations, the reflectivity of the ground scattering component is given by a Dirac delta function
611 modulated by a polarimetrically dependent amplitude. The RVoG model has been extensively
612 validated and its strong and weak points are well understood. Use of this model to obtain a forest
613 height map is illustrated in Fig. 5 which is derived by inverting P-band Pol-InSAR data acquired
614 during the AfriSAR campaign in February 2017 over the Pongara National Park, Gabon. This site is
615 covered mainly by mangrove forests, which are among the tallest mangrove forests in the world,
616 towering up to 60 m.



622

623

624

625

626 **Fig. 5.** Forest height map obtained from inverting P-band Pol-InSAR data acquired over the Pongara
627 National Park, Gabon, in the framework of the AfriSAR campaign in February 2017.

628 The main challenge for BIOMASS is therefore the development of an inversion formulation able to
629 provide unique, unbiased and robust height estimates, and which accounts for: 1) the scattering
630 characteristics at P-band, since the limited attenuation by the forest canopy means that a ground
631 scattering component is present in all polarisations; 2) the constraints imposed by the BIOMASS
632 configuration, both the 6 MHz bandwidth and the fact that some temporal decorrelation is inevitable
633 in the repeat-pass mode (Lee et al., 2013; Kugler et al., 2015). To meet this challenge a flexible multi-
634 baseline inversion scheme has been developed that allows the inversion of the RVoG model by
635 including: 1) a polarimetric three-dimensional ground scattering component; 2) a vertical distribution
636 of volume scattering that can adapt to high (tropical) and low (boreal) attenuation scenarios; 3) a
637 scalar temporal decorrelation that accounts for wind-induced temporal decorrelation of the vegetation
638 layer. The inversion can then be performed using the three polarimetric acquisitions in the
639 Interferometric Phase, allowing global forest height maps to be produced every 7 months.

640 The main limitations in generating the forest height product arise not from the inversion methodology
641 but from the 6 MHz bandwidth, which constrains the generation of large baselines as well as the
642 spatial resolution of the data, and the low frequency, which reduces the sensitivity to forest height in
643 certain sparse forest conditions. On the other hand, the low frequency will provide high temporal
644 stability over the 3-day repeat period of the Interferometric Phase, which is necessary to establish
645 uniqueness and optimum conditioning of the inversion problem.

646 An alternative approach to estimating forest height is by tracing the upper envelope of the observed
647 tomographic intensities, as reported in Tebaldini and Rocca (2012) and Ho Tong Minh et al. (2016)
648 for boreal and tropical forests, respectively. This has the advantage of being less computationally

649 expensive than model-based inversion, and it can be applied in the absence of a specific model of the
650 forest vertical structure. Importantly, it has been demonstrated using synthetic 6 MHz data simulating
651 BIOMASS acquisitions over boreal forests (Tebaldini and Rocca, 2012). However, this approach will
652 only be possible during the Tomographic Phase of the mission.

653

654 **6. Severe forest disturbance**

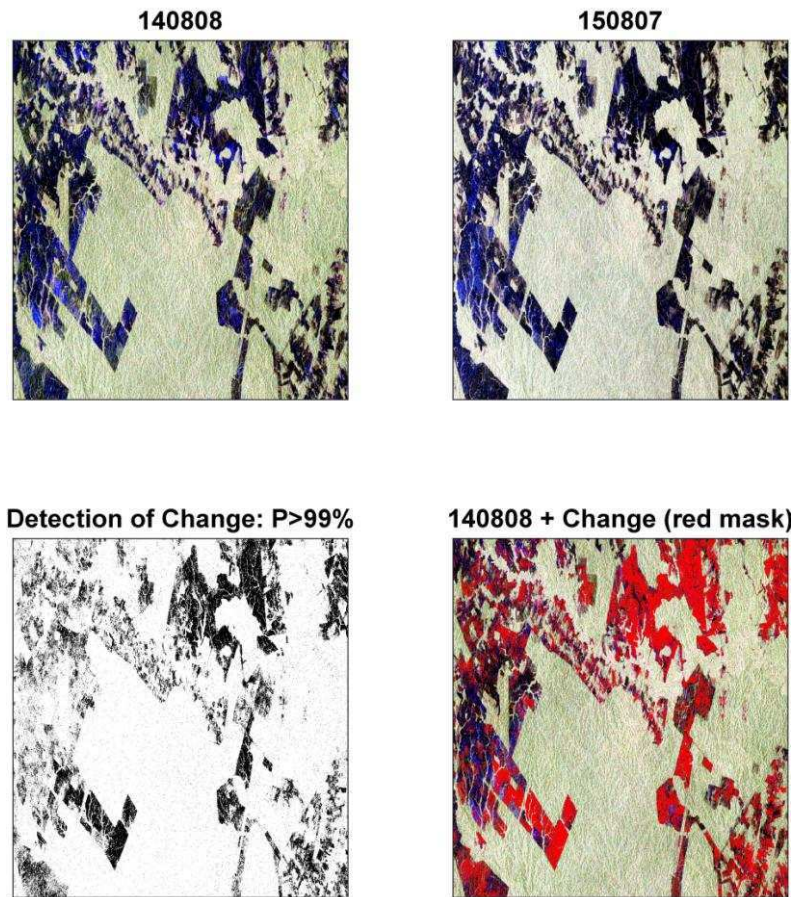
655 The BIOMASS disturbance product aims to detect high-intensity forest disturbance (effectively forest
656 clearance) occurring between satellite revisit times. This is a natural extra use of the data gathered for
657 biomass and height estimation, rather than a driver for the BIOMASS mission, and will contribute to
658 the overall capability to measure forest loss from space using optical (e.g., Hansen et al., 2013) and
659 radar sensors (e.g., the pair of Sentinel-1 C-band radar satellites). Changes in the polarimetric
660 covariance matrix caused by deforestation are relatively large; for example, Fig. 1 indicates that γ_{hv}^0
661 changes by 5 dB as biomass decreases from 500 t ha⁻¹ to nearly zero, while a change in AGB from
662 100 to 200 t ha⁻¹ causes γ_{hv}^0 to change by only ~1 dB. Hence change detection is less affected by the
663 statistical variability inherent in the radar signal, allowing the disturbance product to be produced at a
664 spatial resolution of ~50 m, instead of 200 m, as for the biomass and height products.

665 The method proposed for detecting disturbance is firmly rooted in the statistical properties of the 6-
666 look polarimetric covariance data and uses a likelihood ratio (Conradsen et al., 2016) to test, at a
667 given level of statistical significance, whether change has occurred relative to previous acquisitions in
668 each new polarimetric acquisition over forest. Note that this approach does not specify the detection
669 probability, which would require an explicit form of the multi-variate probability distribution function
670 associated with disturbed forest. This would be very difficult to characterise in any general sense
671 because change may affect the covariance matrix in many different ways. Instead it provides a
672 quantitative way to determine how sure we are that change has occurred; in this respect it is closely
673 related to the Constant False Alarm Rate approach to target detection (e.g. Scharf, 1991).

674 A current unknown in this approach is to what extent changes in the covariance matrix of undisturbed
675 forest caused by environmental effects, such as changing soil moisture due to rainfall events, will

676 ~~increase the false detection rate~~A current unknown in this approach is to what extent changes in the
677 ~~covariance matrix of undisturbed forest caused by environmental effects, such as changing soil~~
678 ~~moisture due to rainfall events, will increase the false detection rate.~~ A further issue is that detections
679 are only sought in forest pixels, so an accurate initial forest map is required, preferably estimated from
680 the radar data themselves but possibly from some other source; this will be progressively updated
681 after each new acquisition.

682 Some insight into the performance of this approach can be gained using multi-temporal polarimetric
683 data from PALSAR-2. Fig. 6 shows at the top Pauli format slant range representations of a pair of
684 images gathered on 8 August 2014 and 8 August 2015 (so in this case the time series has length 2),
685 below left the detection of change at 99% significance and below right the pixels at which change
686 occurred marked in red on the image from 2014 (with no forest mask applied). It can be seen that the
687 areas where change was detected occur in the non-forest regions, while detections in the forest regions
688 occur as isolated pixels consistent with the 1% false alarm rate implied by the level of significance of
689 the test.



690

691 **Fig. 6.** (Top) Pair of repeat-pass PALSAR-2 images acquired on 8 August 2014 and 7 August 2015
 692 displayed in Pauli image format (red = $HH + VV$; blue = $HH - VV$; green = $2HV$) and slant range
 693 geometry. (Bottom left) Detection of change at 99% significance level; changed pixels are marked as
 694 black. (Bottom right) Image from 8 August 2014 with changed pixels marked as red.

695 7. In situ and lidar reference biomass data

696 Although the model-based inversion proposed for estimating biomass (Section 5.1) minimises the
 697 need for in situ reference data, such data are critical for algorithm development and testing,
 698 investigation of regression-based approaches, and product calibration and validation. The BIOMASS
 699 mission faces three major challenges in providing these supporting data: (i) the key region where
 700 reference data are needed is the tropics, but high quality biomass data are available at only a very
 701 limited number of tropical sites; (ii) biomass will be estimated at a scale of 4 ha (200 m by 200 m

702 pixels) but most plot data are available at scales of 1 ha or less and the geographical locations of the
703 plots is often not known to high accuracy; (iii) because of SOTR restrictions (Section 2), reference
704 sites in the temperate and boreal zones will need to be outside N America and Europe.
705 ESA are addressing challenge (i) and (ii) by working with existing networks to develop suitable
706 extensive in situ reference data before launch through the Forest Observation System ([http://forest-
708 observation-system.net/](http://forest-
707 observation-system.net/)). A further encouraging development is the ESA-NASA initiative to
709 collaborate in developing the in situ data requirements for GEDI, BIOMASS and NISAR. Co-
710 operation along these lines is already in evidence from joint contributions to the AfriSAR campaign
711 by ESA and NASA. As regards (iii), for the temperate zone, southern hemisphere sites, e.g. in
712 Tasmania, would be suitable, while Siberia is the most desirable region for the boreal zone. However,
concrete plans to gather in situ data in these regions are not currently in place.

713 An important complement to in situ data that helps to address challenge (ii) is airborne lidar data. This
714 can provide a forest height map and information on canopy structure which, when combined with
715 field data, allows biomass to be estimated. Lidar data offer many advantages, including:

716 • A scanning lidar provides a relatively fine scale and accurate map of biomass, which can be
717 aggregated to the 4 ha resolution cell of BIOMASS (this will allow the effects of variability in
718 biomass at sub-resolution size to be assessed). Precision at this scale is typically below 10%
719 and the vast majority of relevant studies indicate that the associated pan-tropical allometry
720 (Chave et al. 2014) has negligible bias.

721 • Lidar mapping can cover landscapes with a wide range of biomass levels and different forest
722 conditions (degraded, regrowth, selectively logged, etc.).

723 Forest height can be estimated at the same time as biomass, and with fine resolution (around 1 m). An
724 important complement to in situ data that helps to address challenge (ii) is airborne lidar data. This
725 can provide a forest height map and information on canopy structure which, when combined with
726 field data, allows biomass to be estimated. Lidar data offer many advantages, including:

727 • A scanning lidar provides a relatively fine scale and accurate map of biomass, which can be
728 aggregated to the 4 ha resolution cell of BIOMASS (this will allow the effects of variability in

Formatted: Line spacing: Double

729 ~~biomass at sub-resolution size to be assessed). Precision at this scale is typically below 10%~~
730 ~~and the vast majority of relevant studies indicate that the associated pan-tropical allometry~~
731 ~~(Chave et al. 2014) has negligible bias.~~

732 ~~• Lidar mapping can cover landscapes with a wide range of biomass levels and different forest~~
733 ~~conditions (degraded, regrowth, selectively logged, etc.).~~

734 ~~• Forest height with fine resolution (around 1 m) can be estimated at the same time as biomass.~~

735 Hence the validation strategy for BIOMASS will involve a combination of in situ reference forest
736 plots and lidar-derived biomass/height maps.

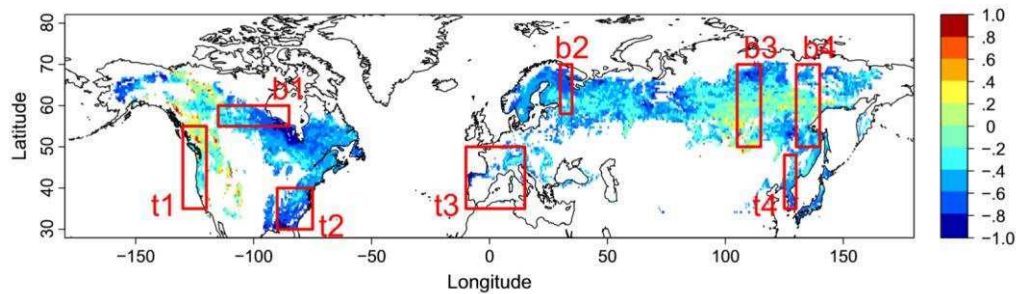
737 **8. Exploiting BIOMASS data in carbon cycle and climate analysis**

738 Although the primary objectives of BIOMASS are to reduce the major uncertainties in carbon fluxes
739 linked to Land Use Change, forest degradation and regrowth and to provide support for international
740 agreements (UNFCCC & REDD+), its products will also play a key role in advancing fundamental
741 knowledge of forest ecology and biogeochemistry. For example, BIOMASS data will help in
742 constraining critical carbon cycle parameters, initialising and testing the land component of carbon
743 cycle and Earth System models (ESMs), and quantifying the forest disturbance regime.

744 Differences between ESM forecasts of the carbon cycle are currently significant, and lead to major
745 uncertainties in predictions (Exbrayat et al., 2018). These differences have been linked to variations in
746 the internal processing of carbon, particularly in the large pools in biomass and soil organic matter
747 (Friend et al. 2014). Linking biomass mapping to estimates of net primary production (NPP) provides
748 a constraint on the turnover rate of the biomass pool, a critical model diagnostic (Carvalhais et al.,
749 2014; Thurner et al., 2014). A recent study (Thurner et al., 2017) found observed boreal and temperate
750 forest carbon turnover rates up to 80% greater than estimates from global vegetation models involved
751 in the Inter-Sectoral Impact Model Intercomparison Project (ISI-MIP) (Warszawski et al., 2014). The
752 relative difference between modelled and observed values is shown in Fig. 7, where the red boxes
753 indicate regions analysed in Thurner et al. (2017) in order to explain these discrepancies. In the boreal
754 zone (boxes b1 - 4) they were mainly attributed to the neglect of the effects of frost damage on

755 mortality in the models, while most of the models did not reproduce observation-based relationships
756 between mortality and drought in temperate forest transects (boxes t1 - 3).

757



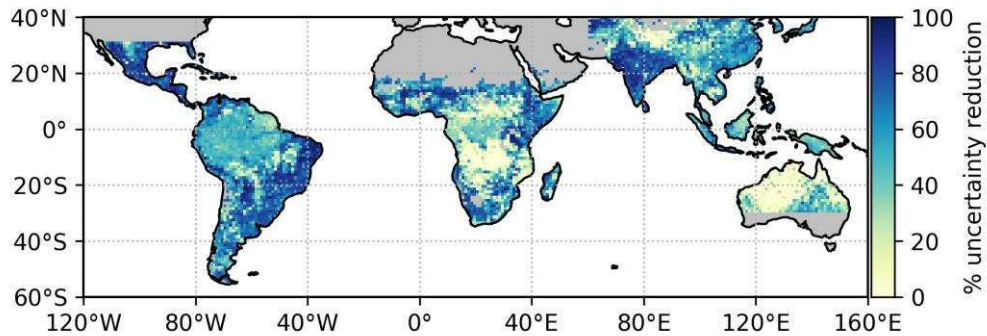
758

759 **Fig 7.** Relative difference between modelled carbon turnover rates and turnover rates inferred from
760 observations. 1.0 means modelled rate is 100% higher (from Thurner et al., 2017). Red boxes labelled
761 b (boreal) and t (temperate) were analysed further in Thurner et al. (2017) to explain these
762 discrepancies (figure reproduced courtesy of Martin Thurner).

763 The more accurate estimates from BIOMASS, particularly over the tropical belt, will greatly improve
764 estimation of turnover across the tropics (Bloom et al., 2016). This information will support improved
765 parameterisation of carbon cycling for ESMs, allowing identification of regional variations in carbon
766 turnover currently missing from tropical plant functional types (Exbrayat et al., 2018a). A sensitivity
767 analysis performed using the CARDAMOM system (Bloom et al., 2016; Exbrayat et al. 2018b)
768 indicates an average reduction of $49.5 \pm 29.2\%$ (mean \pm 2 std) in the 95% confidence interval of the
769 estimated vegetation carbon turnover time when the recent pan-tropical biomass map due to Avitabile
770 et al. (2016) is assimilated. The analysis shows how this error reduction has clear spatial variability
771 with latitude and between continents (Fig. 8).

772 Another component of uncertainty in ESMs is in their initialisation of biomass stocks, arising from
773 the paucity of data in the tropics, Land Use Change and internal model steady states. Data from
774 BIOMASS will provide the modelling community with a compelling resource with which to
775 understand both steady state and transient forest carbon dynamics. Observations of the disturbance
776 regime will constrain modelling of both natural processes of disturbance and mortality and the role of

777 humans (Williams et al., 2013). The potential for BIOMASS to monitor degradation (partial loss of
778 biomass) will be critical for modelling the subtle and slow processes of carbon loss associated with
779 forest edges, fires and human communities (Ryan et al, 2012; Brinck et al., 2017).



780

781 **Fig. 8.** The relative reduction in the size of the 95% confidence interval of estimated vegetation
782 carbon turnover times when using a prior value for biomass at each pixel compared to a run without a
783 biomass prior. Turnover times were estimated using the CARDAMOM system. The darker areas
784 show where reduction in relative uncertainty is largest.

785 Repeated measurements of biomass will allow significant improvements in global monitoring of
786 forest dynamics, and analysis of associated carbon cycling at fine spatial scales. Current biomass
787 maps (e.g., Saatchi et al., 2011) provide maps of stocks at a fixed time (or combine observations from
788 several times). While such data help to constrain the steady state biomass, relevant at regional scales
789 ($\sim 1^\circ$), they give little information on the dynamics of forests at finer (ha to km^2) scales over time.
790 BIOMASS will allow detailed, localised, and temporally resolved analyses of forest dynamics to be
791 constrained. The value of such detailed information has been illustrated in a site level analysis for an
792 aggrading forest in North Carolina (Smallman et al., 2017). Using in situ carbon stock information as
793 a baseline, the analysis showed that a model analysis constrained purely by assimilation of 9
794 sequential annual biomass estimates (corresponding to the BIOMASS scenario, with 1 estimate in the
795 Tomographic Phase and 8 in the Interferometric Phase) together with time series of Leaf Area Index
796 (LAI, e.g. from an operational satellite like Sentinel-2) led to significantly smaller bias and narrower
797 confidence intervals in biomass increment estimates than when LAI and just one biomass estimate, or

798 only management information, were assimilated. Bias in estimated carbon use efficiency (the ratio of
799 NPP to gross primary production) was also significantly reduced by repeated biomass observations.
800 This indicates the potential of BIOMASS to improve significantly our knowledge of the internal
801 processing of carbon in forests.

802 **9. Secondary objectives**

803 BIOMASS will be the first P-band SAR in space and thus will offer previously unavailable
804 opportunities for measuring properties of the Earth. As a result, mission planning includes provision
805 for several secondary objectives, including mapping sub-surface geology, measuring terrain
806 topography under dense vegetation, estimating glacier and ice sheet velocities and investigating
807 properties of the ionosphere.

808 **9.1 Sub-surface geology**

809 In very dry environments, long wavelength SAR is able to probe the sub-surface down to several
810 metres, as was demonstrated at L-band (1.25 GHz) during the first Shuttle Imaging Radar SIR-A
811 mission (Elachi et al., 1984), which revealed buried and previously unknown palaeo-drainage
812 channels in southern Egypt (McCauley et al., 1982; Paillou et al., 2003). More complete L-band
813 coverage of the eastern Sahara acquired by the JAXA JERS-1 satellite was used to produce the first
814 regional-scale radar mosaic covering Egypt, northern Sudan, eastern Libya and northern Chad, from
815 which numerous unknown crater structures were identified (Paillou et al., 2006). In 2006, JAXA
816 launched the Advanced Land Observing Satellite (ALOS-1), carrying a fully polarimetric L-band SAR,
817 PALSAR, which offered higher resolution and much better signal to noise ratio than JERS-1. This
818 provided an unprecedented opportunity to study the palaeo-environment and palaeo-climate of
819 terrestrial deserts (Paillou et al., 2010), and led to the discovery of two major palaeo-rivers in North
820 Africa: the Kufrah river, a 900 km long palaeo-drainage system, which in the past connected
821 southeastern Libya to the Gulf of Sirt (Paillou et al., 2009; Paillou et al., 2012), and the Tamanrasset
822 River in Mauritania, which connected a vast ancient river system in the western Sahara to a large
823 submarine channel system, the Cap Timiris Canyon (Skonieczny et al., 2015). Besides its value in
824 studying the past climates of desert regions, the sub-surface imaging capability of L-band SAR also

825 helps to build more complete and accurate geological maps in support of future water prospecting in
826 arid and semi-arid regions (Paillou, 2017).

827

828 Deeper probing of the sub-surface requires longer radar wavelengths: while L-band can penetrate 1-2
829 m into dry sand, a P-band system should be able to probe down to more than 5 m. In June 2010, the
830 first ever airborne P-band SAR campaign over the Sahara was conducted at a desert site in southern
831 Tunisia using the SETHI system developed by ONERA (Paillou et al., 2011). Figure 9 shows a
832 comparison between an ALOS-2 L-band scene and a P-band scene acquired by SETHI over the Ksar
833 Ghilane oasis, an arid area at the border between past alluvial plains and present day sand dunes.. The
834 P-band data better reveal the sub-surface features under the superficial sand layer because of the higher
835 penetration depth and lower sensitivity to the covering sand surface. A two-layer scattering model for
836 the surface and sub-surface geometry is able to reproduce both the L- and P-band measured backscatter
837 levels, and indicates that the backscatter from the sub-surface layer is about 30 times weaker than from
838 the surface at L-band, while at P-band the sub-surface contribution is about 30 times stronger than that
839 from the surface. As a result, the total backscatter is comparable at P- and L-band, as the data show, but
840 the P-band return is dominated by the sub-surface layer (Paillou et al., 2017). Hence BIOMASS should
841 be a very effective tool for mapping sub-surface geological and hydrological features in arid areas,
842 offering a unique opportunity to reveal the hidden and still unknown history of deserts.

843

844



852

853

854

855 **Figure 9.** Left: SPOT image of the Ksar Ghilane oasis region in southern Tunisia: palaeo-channels are
856 hidden by aeolian sand deposits. Middle: ALOS-2 L-band radar image, showing sub-surface features
857 but blurred by the return from the superficial sand layer. Right: SETHI P-band radar image, clearly
858 revealing sub-surface hydrological features.

859

860 **9.2 Terrain topography under dense vegetation**

861 As an integral part of its ability to make height-resolved measurements of the backscatter in forest
862 canopies, the tomographic phase of the mission will gain access to the ground phase, and hence will
863 be able to derive a true Digital Terrain Model (DTM) that is unaffected by forest cover (Mariotti
864 d’Alessandro and Tebaldini, 2018) and expected to have a spatial resolution of ca. 100 m x 100 m.
865 This contrasts with the Digital Elevation Models (DEMs) produced by radar sensors at higher
866 frequencies, such as SRTM (Rodriguez et al., 2015) or Tandem-X (Wessel et al., 2018), in which
867 attenuation and scattering by dense forest canopies cause biases. Since global tomographic
868 acquisitions occupy the first phase of the mission, this improved DTM will be available early in the
869 Interferometric Phase, and will be used to improve the products based on Pol-InSAR and PolSAR.

870 **9.3 Glacier and ice sheet velocities**

871 The velocity fields of glaciers and icesheets can be measured using two classes of SAR techniques:
872 differential SAR Interferometry (DInSAR) (Massonnet et al., 1993) and offset tracking (Gray et al.,
873 1998; Michel & Rignot, 1999). These techniques measure the ice displacement between two
874 observations and require features in the ice or coherence between the observations. BIOMASS has the
875 potential to supplement ice velocity measurements from other SAR missions, since its left-looking
876 geometry with an inclination angle larger than 90° means that the polar gap in Antarctica will be
877 smaller than for most other SAR missions, which are right-looking. The polar gap will be larger in
878 Greenland, but the Greenland ice sheet cannot be mapped due to SOTR restrictions. The primary

879 advantage of BIOMASS is the higher coherence and longer coherence time resulting from the lower
880 frequency of BIOMASS compared to all other space-based SAR systems. Its longer wavelength with
881 deeper penetration into the firm ensures less sensitivity to snowfall, surface melt and aeolian processes
882 (Rignot, 2008). This is seen when comparing L-band and C-band results (Rignot, 2008; Boncori et al.,
883 2010), and explains the long coherence time observed in airborne P-band data acquired by the Danish
884 Technical University POLARIS SAR in the percolation zone of the Greenland ice sheet (Dall et al.
885 2013).

886 The range and azimuth components of the ice velocity field will most likely be measured with
887 differential SAR interferometry (DInSAR) and offset tracking, respectively. At lower latitudes two
888 velocity components might instead be obtained by combining DInSAR from ascending and
889 descending orbits, since the range resolution of BIOMASS is too coarse for offset tracking to provide
890 the range component (Dall et al. 2013). Generally DInSAR ensures less noisy results, and phase
891 unwrapping is facilitated by the fact that the fringe rate of BIOMASS DInSAR data will be 1/12 of
892 that of Sentinel-1 data, assuming a 6-day baseline in both cases. The very low ice velocities in the
893 interior of Antarctica call for a long temporal baseline, but a 70-day baseline has been successfully
894 used at C-band (Kwok et al., 2000), and therefore sufficiently high P-band coherence is not unlikely
895 with the 228-day baseline provided by the BIOMASS observation cycle. However, ionospheric
896 scintillation is severe at high latitudes, and without accurate correction will corrupt the ice velocity
897 maps, possibly prohibitively. Assessment of whether proposed correction techniques (Kim et al.,
898 2015; Li et al., 2015) are sufficiently accurate will only be possible when BIOMASS is in orbit.

899 **9.4 Ionospheric properties**

900 A major concern in initial studies for BIOMASS was the effect of the ionosphere on the radar signal,
901 and a crucial factor in the selection of the mission was demonstration that these effects could be
902 compensated or were negligible in the context of the mission primary objectives (Rogers et al., 2013;
903 Rogers and Quegan, 2014). However, correction of ionospheric effects (particularly Faraday rotation,
904 but also scintillation, as noted in Section 9.3) necessarily involves measuring them, which then
905 provides information on the ionosphere. The dawn-dusk BIOMASS orbit will cover major features of

906 the ionosphere, including the fairly quiescent ionosphere at low and mid-latitudes, steep gradients
907 around the dusk-side mid-latitude trough, and large irregularities in the auroral ovals and polar cap.
908 Measurements of ionospheric Total Electron Content, derived from Faraday rotation (Wright et al.,
909 2003) and/or interferometric measurements (Tebaldini et al., 2018), should be possible along the orbit
910 at spatial resolutions of around a km, giving an unprecedented capability to measure these spatial
911 structures and their changes, since they will be viewed every two hours as the orbit repeats.

912

913 **10. The role of BIOMASS in an overall observing system**

914 BIOMASS will have unique capabilities to map biomass in dense forests, but will form only part of
915 the overall system of sensors providing information on forest biomass and biomass change, and more
916 generally on the global carbon cycle. In fact, the next few years will see an unprecedented
917 combination of sensors either dedicated to or capable of measuring forest structure and biomass.
918 Particularly important for their links to BIOMASS will be the Global Ecosystem Dynamics
919 Investigation (GEDI) and NISAR missions.

920 GEDI will be a near infrared (1064 nm wavelength) light detection and ranging (lidar) sensor onboard
921 the International Space Station with a 2-year lifetime from deployment in late 2018. It is focusing on
922 tropical and temperate forests to address three key issues: 1) quantifying the above-ground carbon
923 balance of the land surface; 2) clarifying the role played by the land surface in mitigating atmospheric
924 CO₂ in the coming decades; 3) investigating how ecosystem structure affects habitat quality and
925 biodiversity. GEDI will provide the first sampling of forest vertical structure across all forests
926 between 51.5° S and 51.5° N, from which estimates of canopy height, ground elevation and vertical
927 canopy profile measurements will be derived. Further processing of the ~0.0625 ha footprint
928 measurements will then yield estimates of the mean and variance of AGB on a 1 km grid.

929 NISAR (launch 2021) is a joint project between NASA and ISRO (the Indian Space Research
930 Organization) to develop and launch the first dual-frequency SAR satellite, with NASA providing the
931 L-band (24 cm wavelength) and ISRO the S-band (12 cm wavelength) sensors. It will measure AGB
932 and its disturbance and regrowth globally in 1 ha grid-cells for areas where AGB does not exceed 100

933 t/ha, and aims to achieve an accuracy of 20 t/ha or better over at least 80% of these areas. Its focus is
934 therefore on lower biomass forests, which constitute a significant portion of boreal and temperate
935 forests and savanna woodlands. NISAR will give unprecedented L-band coverage in space and time,
936 being able to provide HH and HV observations every 12 days in ascending and descending orbits and
937 covering forests globally every 6 days. The mission is also designed to give global interferometric
938 SAR measurements for surface deformation and cryosphere monitoring.

939 These three missions have significant overlaps in science objectives and products, but focus on
940 different observations, cover different regions, and retrieve different components of AGB at different
941 spatial and temporal scales. Their complementary nature is brought out by Fig. 10, which shows the
942 coverage of the three sensors on a map indicating approximate mean AGB. BIOMASS will focus on
943 tropical and sub-tropical woodlands at 4 ha resolution (though will also cover the temperate and
944 boreal forests of Asia and the southern hemisphere), NISAR will give global coverage at 1 ha
945 resolution but with AGB estimates limited to areas where $AGB < 100$ t/ha, and GEDI will cover the
946 full range of AGB, but with sample footprints limited to lie within $\pm 51.5^\circ$ latitude. Hence without the
947 data from all three missions, wall-to-wall estimation of global forest biomass will not be possible.

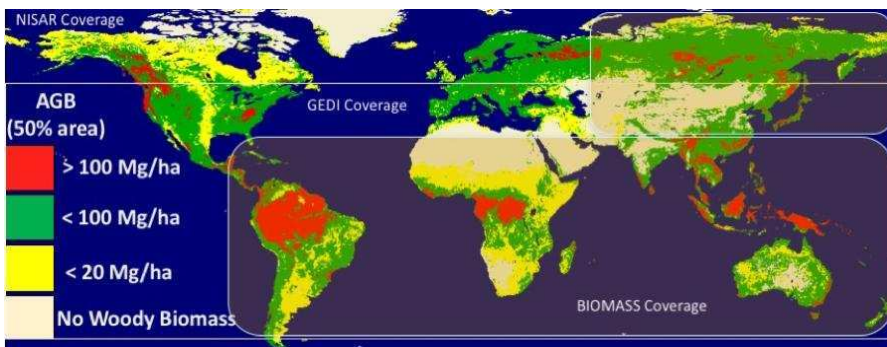
948 There will, however, still be lack of temporal and/or spatial coverage in regions where BIOMASS
949 cannot operate because of SOTR exclusions and where AGB exceeds the 100 t/ha threshold for
950 NISAR~~There will, however, still be lack of temporal and/or spatial coverage in regions where~~
951 ~~BIOMASS cannot operate because of SOTR exclusions and where AGB exceeds the 100 t/ha~~
952 ~~threshold for NISAR.~~

953 For lower values of AGB (less than about 50 t/ha) P-band measurements will be much more affected
954 by soil conditions than L-band, and NISAR should provide more accurate AGB estimates. The high
955 temporal frequency of NISAR observations will also allow the effects of soil moisture changes and
956 vegetation phenology to be mitigated. Currently the theoretical basis of the algorithms proposed for
957 NISAR and BIOMASS are the same (Truong-Loi et al., 2015), which offers the possibility of a
958 combined L- and P-band algorithm that optimises the capabilities of each. In addition, GEDI forest
959 height and biomass products will be available before the NISAR and BIOMASS missions, so can help

960 to initialize their algorithms and validate their products. GEDI estimates of the vertical structure of
961 forests will also be of enormous value in interpreting the BIOMASS Pol-InSAR and tomographic
962 measurements and in producing a consistent forest height and digital terrain model at fine spatial scale
963 (around 1 ha). Conversely, height or backscatter products from NISAR and BIOMASS missions can
964 provide information on the spatial variability of forest structure and biomass; this may be used in
965 future reprocessing to improve both the algorithms that form the GEDI gridded height and biomass
966 products and the resolution of these products.

967 Hence the three sensors will be highly complementary, and their combination will provide an
968 unparalleled opportunity to estimate forest AGB, height and structure globally with unprecedented
969 accuracy, spatial resolution and temporal and spatial coverage.

970



977

978 **Fig. 10.** Coverage of ESA and NASA-ISRO satellite measurements of forest structure and above-
979 ground biomass (AGB). The background shows the global coverage area of NISAR, which will be
980 sensitive to AGB values < 100 t/ha (green and yellow). BIOMASS coverage includes the tropical belt,
981 the temperate and boreal zones of Asia, and the southern hemisphere, while the GEDI Lidar will
982 sample latitudes between $\pm 51.5^\circ$. These two sensors will cover the full range of forest AGB
983 providing measurements where AGB >100 t/ha (red), so inaccessible to NISAR.

984

985 **Discussion**

Formatted: Font: 11 pt

986 Along with its role in quantifying the biomass and its change, it is important to realize that the
987 BIOMASS instrument, particularly in its interferometric and tomographic modes, is capable of
988 producing global measures of important forest properties that are simply unavailable for almost all of
989 the Earth. Some of these are practical measurements whose value has been known for years. For
990 example, in forestry the ability to predict yield or increase in biomass is increased greatly when one
991 knows both mass and height, so much so that tree height has been used in yield-table-based forestry to
992 quantify the so-called site-index, the quality of a site for forest enterprise. Hence the information from
993 the BIOMASS satellite and the modern digital offspring of classic forestry yield tables could be used
994 to make informed estimates of expected net production of forest biomass. In similar vein, Section 8
995 notes how the combination of biomass with NPP allows the turnover time of carbon within forest
996 vegetation to be estimated. Both examples illustrate that although forest biomass, height, structure and
997 change are all individually important, their full significance for climate, carbon cycle, biodiversity,
998 resource management, etc., is only fully realised when they are combined with each other and with
999 other sources of information.

1000 This perception of biomass as a key variable within a wider information system is implicit in the
1001 recognition of AGB as an ECV (GCOS, 2017). More explicit analysis of its function within a carbon
1002 information and management system is provided by the Group on Earth Observations (GEO) (Ciais et
1003 al., 2010) and the response to this report in the CEOS Strategy for Carbon Observations from Space
1004 (CEOS, 2014). In particular, the CEOS report (Fig. 2.3 and Table 2.1 of the report) indicates where
1005 biomass fits within the set of key GEO satellite requirement areas and core GEO observational
1006 elements necessary to quantify the current state and dynamics of the terrestrial carbon cycle and its
1007 components. Central to the GEO Carbon Strategy is the combination of data and carbon cycle models,
1008 not least because models provide the only way in which the many available space-based and in situ
1009 measurements can be integrated into a single consistent structure for performing carbon flux
1010 calculations.

1011 There are many possible forms for these models but data can interact with them in essentially four
1012 ways: by providing estimates of current model state variables, estimates of model parameters, tracking

1013 of processes and testing of model predictions. In addition, data and models can be even more tightly
1014 bound by combining them in a data assimilation structure where both are regarded as sources of
1015 information whose relative contribution to carbon flux estimates is weighted by their uncertainty.
1016 There are already significant developments in exploiting biomass data in these ways, for example
1017 initializing the age structure of forests when estimating the European carbon balance (Bellassen et al.,
1018 2011), estimating carbon turnover time (Turner et al., 2017), testing Dynamic Global Vegetation
1019 Models (Cantú et al., 2018), and full-scale data assimilation (Bloom et al., 2016). Further progress in
1020 this direction is to be expected as we move towards launch in 2022.

1021 **Conclusions**

1022 BIOMASS mission will be the first space-based P-band radar, and this completely new view from
1023 space will yield both predictable and unforeseen opportunities to learn about the Earth and its
1024 dynamics. Within the operational constraints imposed by the Space Object Tracking Radar system
1025 (Section 2) the 5-year mission will provide global mapping of forest AGB, height and change at 200
1026 m spatial resolution by combining three different radar techniques, each of them innovative. This is
1027 the first space-based radar mission for which all observations will be fully polarimetric, which is
1028 necessary both to recover biomass information and to correct ionospheric effects. Even more
1029 innovative will be this first systematic use of Pol-InSAR to measure forest height globally, and the
1030 first use of SAR tomography to identify the vertical structure of forests globally. In parallel with these
1031 major technological developments, considerable progress is being made in developing new
1032 understanding and quantitative methods that will allow these measurements to be exploited in carbon
1033 cycle and climate models. This link between measurements and models forms an essential part of
1034 meeting the primary objective of the BIOMASS mission, which is to determine the worldwide
1035 distribution of forest AGB in order to reduce the major uncertainties in calculations of carbon stocks
1036 and fluxes associated with the terrestrial biosphere, including carbon fluxes associated with Land Use
1037 Change, forest degradation and forest regrowth. Of major mutual advantage in meeting this objective
1038 will be the information provided by other space missions flying within the next five years, for which
1039 pride of place goes to GEDI and NISAR, but supplemented by optical and other radar missions. Of

1040 great importance is that the structures for making use of these new data in carbon cycle and climate
1041 models are being developed and implemented.

1042 The physical and technical capabilities embedded in the BIOMASS mission in order to measure
1043 biomass can be turned to many other uses. At present, known applications include sub-surface
1044 imaging in arid regions, estimating glacier and icesheet velocities, and production of a true DTM
1045 without biases caused by forest cover. An originally unforeseen application arising from the need to
1046 correct the radar signal for ionospheric effects is to exploit the high sensitivity of the P-band signal to
1047 Total Electron Content to estimate ionospheric properties and changes along the satellite's dawn-dusk
1048 orbit. This is likely to be just one amongst many novel uses of the BIOMASS data, whose scope will
1049 only become clear once BIOMASS is in orbit.

1050 **Acknowledgements**

1051 This work was in part supported by the UK National Environment Research Council National Centre
1052 for Earth Observation (NCEO).

1053

1054 **References**

1055

1056 Antonarakis, A.S., Saatchi, S.S., Chazdon, R.L. & Moorcroft, P.R. (2011). Using Lidar and radar
1057 measurements to constrain predictions of forest ecosystem structure and function. *Ecological*
1058 *Applications*, 21(4), 1120–1137.

1059 Askne, J. I. H., Soja, M. J., and Ulander, L. M. H. (2017). Biomass estimation in a boreal forest from
1060 TanDEM-X data, lidar DTM, and the interferometric water cloud model, *Remote Sensing of Env.*,
1061 196, 265-278, doi:org/10.1016/j.rse.2017.05.010.

1062 Avitabile, V., Herold, M., Heuvelink, G. B. M., Lewis, S. L., Phillips, O. L., Asner, G. P., et al.
1063 (2016). An integrated pan-tropical biomass map using multiple reference datasets, *Glob. Change Biol.*
1064 22(4), 1406-1420, doi: 10.1111/gcb.13139.

1065 Baccini, A., Goetz, S. J., Walker, W. S., Laporte, N. T., Sun M., Sulla-Menashe, D., et al. (2012).
1066 Estimated carbon dioxide emissions from tropical deforestation improved by carbon-density maps.
1067 Nature Clim. Change, 2, 182-185, doi:110.1038/nclimate1354.

1068 Baccini, A., Walker, W., Carvalho, L., Farina, M., Sulla-Menashe, D., Houghton, R. A. (2017).
1069 Tropical forests are a net carbon source based on aboveground measurements of gain and loss,
1070 Science, 358(6360), 230-234, doi:10.1126/science.aam5962.

1071 Bai, Y., Tebaldini, S., Ho Tong Minh, D., and Yang, W. (2018). An empirical study on the impact of
1072 changing weather conditions on repeat-pass SAR tomography,” IEEE Jnl. Selected Topics in Applied
1073 Earth Observations and Remote Sensing, 1–7.

1074 Bellassen, V., Viovy, N., Luysaert, S., Le Maire, G., Schelhaas, M.-J. and Ciais, P. (2011).
1075 Reconstruction and attribution of the carbon sink of European forests between 1950 and 2000, Global
1076 Change Biology, 17, 3274–3292, doi: 10.1111/j.1365-2486.2011.02476.x.

1077 Bloom AA, Exbrayat J-F, van der Velde I.R., Feng L, Williams, M. (2016). The decadal state of the
1078 terrestrial carbon cycle: Global retrievals of terrestrial carbon allocation, pools, and residence times,
1079 PNAS, 113(5), 1285-1290, [doi:pnas.1515160113](https://doi.org/10.1073/pnas.1515160113).

1080 Boncori, J.P.M., Dall, J., Ahlstrøm, A.P., Andersen, S.B. (2010). Validation and operational
1081 measurements with SUSIE: a SAR ice motion processing chain developed within PROMICE
1082 (Programme for Monitoring of Greenland Ice-Sheet), Proc. ESA Living Planet Symposium, Bergen.

1083 Bouvet, A., Mermoz, S., Le Toan, T., Villard, L., Mathieu, R., Naidoo, L., and Asner, G. P. (2018).
1084 An above-ground biomass map of African savannahs and woodlands at 25 m resolution derived from
1085 ALOS PALSAR, Remote Sens. Env., 206, 156–173.

1086 Brinck, K., Fischer, R., Groeneveld, J., Lehmann, S., De Paula, M.D., et al. (2017). High resolution
1087 analysis of tropical forest fragmentation and its impact on the global carbon cycle. Nature
1088 Communications, 8, 14855

1089 Cairns, M.A., Brown, S., Helmer, E.H., & Baumgardner, G.A. (1997). Root biomass allocation in the
1090 world’s upland forests. Oecologia, 111, 1–11.

1091 Cantú, A. G., Friele, K., Reye, C. P.O., Ciais, P., Chang, J., Ito, A., et al. (2018). Evaluating changes
1092 of biomass in global vegetation models: the role of turnover fluctuations and ENSO events, *Environ.*
1093 *Res. Lett.*, 13, 075002.

1094 Carreiras, J. M. B., Quegan, S., Le Toan, T., Ho Tong Minh, D., Saatchi, S., Carvalhais, N., et al.
1095 (2017). Coverage of high biomass forests by the ESA BIOMASS mission under defense restrictions,
1096 *Remote Sensing of Environment*, 196, 154-162, doi.org/10.1016/j.rse.2017.05.003.

1097 Carvalhais N, Forkel M, Khomik M, Bellarby J, Jung M, Migliavacca M, et al. (2014). Global
1098 covariation of carbon turnover times with climate in terrestrial ecosystems. *Nature*, 514, 213-217.

1099 CEOS (2014). CEOS Strategy for Carbon Observations from Space; The Committee on Earth
1100 Observation Satellites (CEOS) Response to the Group on Earth Observations (GEO) Carbon
1101 Strategy.

1102 Chave, J. (1999). Study of structural, successional and spatial patterns in tropical rain forests using
1103 TROLL, a spatially explicit forest model, *Ecological Modelling*, 124 (2–3), 233–254.

1104 Chave, J., Rejou-Mechain, M., Burquez, A., Chidumayo, E., Colgan, M. S., Delitti, W. B., et al.
1105 (2014). Improved allometric models to estimate the aboveground biomass of tropical trees, *Global*
1106 *Change Biology*, 20, 3177–3190, doi: 10.1111/gcb.12629.

1107 Ciais, P., Dolman, A. J., Dargaville, R., Barrie, L., Bombelli, A., Butler, J., et al. (2010). GEO Carbon
1108 Strategy, GEO Secretariat Geneva/FAO, Rome, 48 pp.

1109 Cloude, S. R., and Pottier, E. (1996). A review of target decomposition theorems in radar polarimetry,
1110 *IEEE Trans. Geosci. Remote Sens.*, 34(2), 498–518.

1111 Cloude, S. R., and Papathanassiou, K. P. (1998). Polarimetric SAR interferometry, *IEEE Trans.*
1112 *Geosci. Remote Sensing*, 36(5), 1551-1565.

1113 Cloude S. R. and Papathanassiou, K. P. (2003), Three-stage inversion process for polarimetric SAR
1114 interferometry, *IEE Proc. Radar, Sonar and Navigation*, 150(3), 125-134.

1115 Conradsen, K., Nielsen, A. A., Schou, J., and Skriver, H. (2003). A test statistic in the complex
1116 Wishart distribution and its application to change detection in polarimetric SAR data, *IEEE Trans.*
1117 *Geosci. Remote Sensing*, 41(1), 4-19.

1118 Conradsen, K., Nielsen, A. A., and Skriver, H. (2016). Determining the points of change in time series
1119 of polarimetric SAR data, *IEEE Trans. Geosci. Remote Sensing*, 54(5), 3007-3024.

1120 Dall, J., Nielsen, U., Kusk, A., van de Wal, R.S.W. 2013. Ice flow mapping with P-band SAR, *Proc.*
1121 *Int Geosci. Remote Sensing Symp. (IGARSS 2013)*, Melbourne.

1122 Dubois-Fernandez, P., Le Toan, T., Daniel, S., Oriot, H., Chave, J., Blanc, L., et al. (2012). The
1123 TropiSAR airborne campaign in French Guiana: Objectives, description and observed temporal
1124 behavior of the backscatter signal, *IEEE Trans. Geosci. Remote Sensing*, 50(8), 3228-3241.

1125 Elachi, C., Roth, L. E., and Schaber, G. G. (1984). Spaceborne radar sub-surface imaging in hyperarid
1126 regions, *IEEE Trans. Geosci. Remote Sensing*, vol. GE-22, pp. 383-388,.

1127 European Space Agency (2008). BIOMASS: Candidate Earth Explorer Core Missions - Reports for
1128 Assessment; ESA SP-1313-2, Mission Science Division, ESA-ESTEC, Noordwijk, the Netherlands,
1129 ISSN 0379-6566, 122 pp.

1130 European Space Agency (2012). Report for Mission Selection: Biomass. Science authors: Quegan, S.,
1131 Le Toan T., Chave, J., Dall, J., Perrera, A., Papathanassiou, et al., ESA SP 1324/1 (3 vol. series),
1132 European Space Agency, Noordwijk, the Netherlands, pp. 193.

1133 European Space Agency (2015). Biomass Mission Requirements Document, EOP-SM/1645.

1134 Exbrayat, J.-F., Bloom, A. A., Falloon, P., Ito, A., Smallman, T. L., & Williams, M. (2018a).
1135 Reliability ensemble averaging of 21st century projections of terrestrial net primary productivity
1136 reduces global and regional uncertainties. *Earth System Dynamics*, 9(1), 153–165,
1137 <https://doi.org/10.5194/esd-9-153-2018>.

1138 Exbrayat, J.- F., Luke Smallman, T., Anthony Bloom, A., Hutley, L. B., & Williams, M.
1139 (2018b). Inverse determination of the influence of fire on vegetation carbon turnover in the
1140 pantropics. *Global Biogeochemical Cycles*, 32, 1776–1789. <https://doi.org/10.1029/2018GB005925>.

1141 FAO. (2006). Global Forest Resources Assessment 2005. FAO Forestry Paper 147, United Nations
1142 Food and Agriculture Organization, Rome, Italy.

1143 FAO (2008). UN Collaborative Programme on Reducing Emissions From Deforestation And Forest
1144 Degradation in Developing Countries (UN-REDD). FAO, UNDP, UNEP.

1145 FAO (2009) Assessment of the status of the development of the standards for the Terrestrial Essential
1146 Climate Variables, GTOS Secretariat, UN Food and Agriculture Organisation, Rome, Italy.

1147 FAO. (2010). Global Forest Resources Assessment 2010, United Nations Food and Agriculture
1148 Organization, Rome, Italy. ISBN 978-92-5-106654-6.

1149 FAO (2016). Global Forest Resources Assessment 2015 Second Edition, Food and Agriculture
1150 Organization of the United Nations, Rome, ISBN 978-92-5-109283-5.

1151 FAO (2012). Global Ecological Zones for FAO Forest Reporting: 2010 Update. Forest Resources
1152 Assessment Working Paper 179, Food and Agriculture Organisation of the United Nations, Rome,
1153 Italy.

1154 Fransson, J. E. S., Walter, F., and Ulander, L. M. H. (2000). Estimation of forest parameters using
1155 CARABAS-II VHF SAR data, IEEE Trans. Geosci. Remote Sens., 38(2), 720–727.

1156 Freeman, A., and Durden, S. (1998). A three-component scattering model for polarimetric SAR data,
1157 IEEE Trans. Geosci. Remote Sens., 36(3), 963–973.

1158 Friend, A. D., Lucht, W., Rademacher, T. T., Keribin, R. M., Betts, R., et al. (2014). Carbon residence
1159 time dominates uncertainty in terrestrial vegetation responses to future climate and atmospheric CO₂.
1160 Proceedings of the National Academy of Sciences of the United States of America, 111, 3280 – 3285.

1161 Garestier, F., Dubois-Fernandez, P. C., and Papathanassiou, K. P. (2008). Pine forest height inversion
1162 using single-pass X-Band Pol-InSAR data, IEEE Trans. Geosci. Remote Sensing, 46(1), 59-68.

1163 GCOS (2015). Status of the Global Observing System for Climate, GCOS-195, WMO, Geneva,
1164 http://www.wmo.int/pages/prog/gcos/Publications/GCOS-195_en.pdf.

1165 GCOS (2017). The Global Observing System for Climate: implementation needs, GCOS-200, WMO,
1166 Geneva.

1167 Gray, A.L., Mattar, K.E., and Vachon, P.W. (1998). InSAR results from the RADARSAT Antarctic
1168 mapping mission data: estimation of data using a simple registration procedure, Proc. Int Geosci.
1169 Remote Sensing Symp. (IGARSS 1998), Seattle.

1170 Hajnsek I., Scheiber, R., Ulander, L., Gustavsson, A., Sandberg, G., Tebaldini, S., et al. (2008).
1171 BIOSAR 2007: Technical Assistance for the Development of Airborne SAR and Geophysical
1172 Measurements during the BioSAR 2007 Experiment, Final Report, ESA contract No.:
1173 20755/07/NL/CB.

1174 Hajnsek, I., Scheiber, R., Keller, M., Horn, R., Lee, S., Ulander, L., et al. (2009). BIOSAR 2008: Final
1175 Report, ESTEC Contract 22052/08/NL/CT-002, 302 pp.

1176 Hajnsek, I., Kugler, F., Lee, S.K., and Papathanassiou, K.P. (2009). Tropical forest parameter
1177 estimation by means of Pol-InSAR: The INDREX-II campaign, IEEE Trans. Geosci. Remote Sensing
1178 47(2), 481-493.

1179 Hansen, M. C., Potapov, P. V., Moore, R., Hancher, M., Turubanova, S. A., Tyukavina, A., et al.
1180 (2013). High-resolution global maps of 21st-century forest cover change, Science, 15(342), Issue
1181 6160, 850-853, doi: 10.1126/science.1244693.

1182 Ho Tong Minh, D., Tebaldini, S., Rocca, F., Albinet, C., Borderies, P., Koleček, T., et al. (2012).
1183 Tropiscat: multi-temporal multi-polarimetric tomographic imaging of tropical forest, Proc. 2012 IEEE
1184 International Geosci. Remote Sensing Symp., Munich, 22-27 July 2012, 7051-7054.

1185 Ho Tong Minh, D., Le Toan, T., Rocca, F., Tebaldini, S., d'Alessandro, M. M., and Villard, L.
1186 (2014). Relating P-band Synthetic Aperture Radar tomography to tropical forest biomass, IEEE Trans
1187 Geosci. Remote Sensing, 52(2), 967-979.

1188 Ho Tong Minh, D., Le Toan, T., Rocca, F., Tebaldini, S., Villard, L., Réjou-Méchain, M., Phillips,
1189 O.L., Feldpausch, T.R., Dubois-Fernandez, P., Scipal, K., Chave, J. (2016). SAR tomography for the

1190 retrieval of forest biomass and height: Cross-validation at two tropical forest sites in French Guiana,
1191 Remote Sensing of Environment, 175, 138-147.

1192 IPCC (2007). IPCC Fourth Assessment Report: Climate Change 2007, The Physical Science Basis.
1193 Cambridge University Press, Cambridge, UK.

1194 IPCC (2013). Climate Change 2013: The Physical Science Basis. Contribution of Working Group I to
1195 the Fifth Assessment Report of the Intergovernmental Panel on Climate Change (Stocker, T. F., D.
1196 Qin, G.-K. Plattner, M. Tignor, S. K. Allen, J. Boschung, A. Nauels, Y. Xia, V. Bex and P. M.
1197 Midgley (eds.)). Cambridge University Press, Cambridge, United Kingdom and New York, NY, USA,
1198 1535 pp.

1199 Kim, J.-S., Papathanassiou, K., Scheiber, R., and Quegan, S. (2015). Correction of ionospheric
1200 scintillation induced distortions on polarimetric SAR data, IEEE Trans. Geosci. Remote Sensing, doi:
1201 10.1109/TGRS.2015.2431856.

1202 Koleček, T., Borderies, P., Rocca, F., Albinet, C., Ho Tong Minh, D., Tebaldini, S., Hamadi, A., et al.
1203 (2012). TropiSCAT: A polarimetric and tomographic scatterometer experiment in French Guiana
1204 forests, Proc. 2012 IEEE International Geosci. Remote Sensing Symp., Munich, 22-27 July 2012,
1205 7597-7600, doi: [10.1109/IGARSS.2012.6351869](https://doi.org/10.1109/IGARSS.2012.6351869)

1206 Kugler, F., Schulze, D., Hajnsek, I., Pretzsch, H., Papathanassiou, K. P. (2014). TanDEM-X Pol-
1207 InSAR performance for forest height estimation, IEEE Trans. Geosci. Remote Sensing, 52(10), 6404-
1208 6422.

1209 Kugler, F., Lee, S-K., Papathanassiou, K. P. (2015). Forest height estimation by means of Pol-InSAR
1210 data inversion: the role of the vertical wavenumber, IEEE Trans. Geosci. Remote Sensing, 53(10),
1211 5294-5311

1212 Kwok, R., Siegert, M.J., Carsey, F.D. (2000). Ice motion over Lake Vostok, Antarctica: constraints on
1213 inferences regarding the accreted ice, Journal of Glaciology, 46(155), 689-694.

1214 Labrière, N., Tao, S., Chave, J., Scipal, K., Le Toan, T., Abernethy, K., et al. (2018). In situ reference
1215 datasets from the TropiSAR and AfriSAR campaigns in support of upcoming spaceborne biomass

1216 missions, *IEEE Jnl. Selected Topics in Applied Earth Observations and Remote Sensing*, 11(10),
1217 3617-3627, doi: [10.1109/JSTARS.2018.2851606](https://doi.org/10.1109/JSTARS.2018.2851606).

1218 Le Quéré, C., Andrew, R. M., Friedlingstein, P., Sitch, S., Pongratz, J., Manning, A. C., et al. (2018).
1219 Global Carbon Budget 2017, *Earth Syst. Sci. Data*, 10, 405-448, doi: 10.5194/essdd-2017-123.

1220 Le Toan T., Quegan, S., Davidson, M., Balzter, H., Paillou, P., Papathanassiou, K., et al. (2011). The
1221 BIOMASS mission: Mapping global forest biomass to better understand the terrestrial carbon cycle,
1222 *Remote Sens. Env.*, 115, 2850–2860.

1223 Ledo, A., Paul, K. I., Burslem, D. F., Ewel, J. J., Barton, C., Battaglia, M., et al. (2018). Tree size and
1224 climatic water deficit control root to shoot ratio in individual trees globally, *New Phytologist*, 217(1),
1225 8-11.

1226 Lee, J.-S., Schuler, D., and Ainsworth, T. (2000). Polarimetric SAR data compensation for terrain
1227 azimuth slope variation, *IEEE Trans Geosci. Remote Sensing*, 38(5), 2153–2163.

1228 Lee, S.-K., Kugler, F., Papathanassiou, K. P., and Hajnsek, I. Quantification of temporal decorrelation
1229 effects at L-band for polarimetric SAR interferometry applications (2013). *IEEE Jnl. Selected Topics*
1230 *in Applied Earth Observations and Remote Sensing*, 6(3), 1351-1367.

1231 Lefsky, M. A., Harding, D. J., Keller, M., Cohen, W. B., Carabajal, C., Del Bom Espirito-Santo, F., et
1232 al. (2005). Estimates of forest canopy height and aboveground biomass using ICESat. *Geophysical*
1233 *Research Letters* 32, L22S02, doi:10.1029/2005GL023971.

1234 Lefsky, M. A. (2010). A global forest canopy height map from the Moderate Resolution Imaging
1235 Spectroradiometer and the Geoscience Laser Altimeter System, *Geophysical Research Letters* 37(15),
1236 doi.org/10.1029/2010GL043622

1237 Li, Z., Quegan, S., Chen, J., and Rogers, N. C. (2015). Performance analysis of Phase Gradient
1238 Autofocus for compensating ionospheric scintillation in BIOMASS P-band SAR data, *IEEE Trans.*
1239 *Geosci. Remote Sensing Letts.*, 12(6), 1367-1371, doi: 10.1109/LGRS.2015.2402833.

1240 Mariotti d'Alessandro, M., Tebaldini, S., Quegan, S., Soja, M. J., Ulander, L. M. H. (2018).
1241 Interferometric ground notching, *Proc. Int Geosci. Remote Sensing Symp. (IGARSS 2018)*, Valencia.

1242 Mariotti d'Alessandro, M. and Tebaldini, S. (2018). Retrieval of terrain topography in tropical forests
1243 using P-band SAR tomography, Proc. Int Geosci. Remote Sensing Symp. (IGARSS 2018), Valencia.

1244 Mariotti d'Alessandro, M., Tebaldini, S., and Rocca, F. (2013). Phenomenology of ground scattering
1245 in a tropical forest through polarimetric synthetic aperture radar tomography, IEEE Trans. Geosci.
1246 Remote Sensing, 51(8), 4430-4437.

1247 Meyer, V., Saatchi, S., Clark, D. B., Keller, M., Vincent, G., et al. (2018). Canopy area of large trees
1248 explains aboveground biomass variations across neotropical forest landscapes, Biogeosciences, 15,
1249 3377–3390.

1250 Massonnet, D., Rossi, M., Carmona, C., Adragna, F., Peltzer, G., Feigl, K., Rabaute, T. (1993). The
1251 displacement field of the Landers earthquake mapped by radar interferometry, Nature, 364, 138-142.

1252 McCauley, J. F., Schaber, G. G., Breed, C. S., Grolier, M. J., Haynes, C. V., Issawi, B., et al. (1982).
1253 Sub-surface valleys and geoarchaeology of the eastern Sahara revealed by Shuttle Radar, Science,
1254 218, pp. 1004-1020,.

1255 Michel, R. & Rignot, E. (1999). Flow of Glacier Moreno, Argentina, from repeat-pass Shuttle
1256 Imaging Radar images: comparison of the phase correlation method with radar interferometry.
1257 Journal of Glaciology, 45(149), 93–100.

1258 Mitchard, E. T. A., Saatchi, S. S., Woodhouse, I. H., Nangendo, G., Ribeiro, N. S., and Williams, M.
1259 (2009). Using satellite radar backscatter to predict above-ground woody biomass: A consistent
1260 relationship across four different African landscapes, Geophys. Res. Lett., 36, Article L23401,
1261 doi:[10.1029/2009GL040692](https://doi.org/10.1029/2009GL040692).

1262 Mitchard, E. T. A., Saatchi, S. S., Baccini, A., Asner, G. P., Goetz, S. J., Harris, N. L., et al., (2013).
1263 Uncertainty in the spatial distribution of tropical forest biomass: a comparison of pan-tropical maps.
1264 Carbon Balance and Management, 8(10), doi:10.1186/1750-0680-8-10.

1265 Mitchard, E. T. A., Feldpausch, T. R., Brienen, R. J. W., Lopez-Gonzalez, G., Monteagudo, A.,
1266 Baker, T. R., et al., (2014). Markedly divergent estimates of Amazon forest carbon density from
1267 ground plots and satellites. Global Ecol. Biogeogr., 23(8), 836-955, doi: 10.1111/geb.12168.

1268 Mokany, K., Raison, R.J., and Prokushkin, A.S. (2006). Critical analysis of root:shoot ratios in
1269 terrestrial biomes. *Global Change Biology*, 12(1), 84-96.

1270 Monteith, A. R., and Ulander, L. M. H. (2018). Temporal survey of P- and L-band polarimetric
1271 backscatter in boreal forests, *IEEE Jnl. Selected Topics in Applied Earth Observations and Remote*
1272 *Sensing*, 11(10), 3564 – 3577.

1273 Paillou, P., Grandjean, G., Baghdadi, N., Heggy, E., August-Bernex, T., and Achache, J. (2003). Sub-
1274 surface imaging in central-southern Egypt using low frequency radar: Bir Safsaf revisited, *IEEE*
1275 *Trans. Geosci. Remote Sensing*, 41(7), 1672-1684.

1276 Paillou, P., Reynard, B., Malézieux, J.-M., Dejax, J., Heggy, E., Rochette, P., et al. (2006). An
1277 extended field of crater-shaped structures in the Gilf Kebir region – Egypt: Observations and
1278 hypotheses about their origin, *Jnl. African Earth Sciences*, 46, 281-299.

1279 Paillou, P., Schuster, M., Tooth, S., Farr, T., Rosenqvist, A., Lopez, S., et al. (2009). Mapping of a
1280 major paleodrainage system in Eastern Libya using orbital imaging Radar: The Kufrah River, *Earth*
1281 *and Planetary Science Letters*, 277, 327-333, doi: 10.1016/j.epsl.2008.10.029.

1282 Paillou, P., Lopez, S., Farr, T. and Rosenqvist, A. (2010). Mapping sub-surface geology in Sahara
1283 using L-band SAR: first results from the ALOS/PALSAR imaging radar, *IEEE Journal of Selected*
1284 *Topics in Earth Observations and Remote Sensing*, 3(4), 632-636.

1285 Paillou, P., Ruault du Plessis, O., Coulombeix, C., Dubois-Fernandez, P., Bacha, S., Sayah, N., et al.
1286 (2011). The TUNISAR experiment: flying an airborne P-band SAR over southern Tunisia to map sub-
1287 surface geology and soil salinity,” *PIERS 2011, Marrakesh, Morocco*.

1288 Paillou, P., Tooth, S., and Lopez, S. (2012). The Kufrah paleodrainage system in Libya: a past
1289 connection to the Mediterranean Sea?, *C.R. Geoscience*, 344, 406-414.

1290 Paillou, P. (2017). Mapping palaeohydrography in deserts: contribution from space-borne imaging
1291 radar, *Water*, 9(194).

1292 Paillou, P. Dubois-Fernandez, P., Lopez, S., and Touzi, R. (2017). SAR polarimetric scattering
1293 processes over desert areas: Ksar Ghilane, Tunisia, *POLINSAR, Frascati, Italy*.

1294 Pan, Y., Birdsey, R.A., Fang, J., Houghton, R., Kauppi, P.E., Kurz, W. A., et al. (2011). A large and
1295 persistent carbon sink in the world's forests. *Science*, 333, 988-993.

1296 Papathanassiou, K. P., Cloude, S. R. (2001). Single-baseline polarimetric SAR interferometry. *IEEE*
1297 *Trans. Geosci. Remote Sensing*, 39(11), 2352-2363.

1298 Persson, H. J., Olsson, H., Soja, M. J., Ulander, L. M. H., and Fransson, J. E. S. (2017). Experiences
1299 from large-scale forest mapping of Sweden using TanDEM-X data, *Remote Sensing*, 9 (12),
1300 doi:10.3390/rs9121253.

1301 Philip, M.S. (1994). *Measuring Trees and Forests*, Second Edition, CAB International, Oxon, UK.

1302 Praks, J., Kugler, F., Papathanassiou, K. P., Hajnsek, I., Hallikainen, M. (2007). Tree height
1303 estimation for boreal forest by means of L- and X-band Pol-InSAR and HUTSCAT scatterometer,
1304 *IEEE Trans. Geosci. Remote Sensing Letts.*, 37(3), 466–470.

1305 Quegan, S., Lomas, M., Papathanassiou, K. P., Kim, J-S., Tebaldini, S., Giudici, D., et al. (2018).
1306 Calibration challenges for the BIOMASS P-band SAR instrument, *Proc. IEEE Int. Geosci. Remote*
1307 *Sensing Symp. (IGARSS 2018)*, Valencia.

1308 Rackham, O., & Moody, J. (1996). *The making of the Cretan landscape*. Manchester University Press.

1309 Rodriguez, E., Morris, C. S., Belz, J. E., Chapin, E. C., Martin, J. M., Daffer, W., et al. (2005). An
1310 assessment of the SRTM topographic products, Technical Report JPL D-31639, Jet Propulsion
1311 Laboratory, Pasadena, California.

1312 Radkau, J. (2012). *Wood: a history* (Vol. 17). Polity.

1313 Rignot, E. (2008). Changes in West Antarctic ice stream dynamics observed with ALOS PALSAR
1314 data, *Geophysical Research Letters* **35**, L12505, doi:10.1029/2008GL033365, 1–5.

1315 Rogers, N. C., Quegan, S., Kim, J. S. and Papathanassiou, K. P. (2013). Impacts of ionospheric
1316 scintillation on the BIOMASS P-band satellite SAR, *IEEE Trans. Geosci. Remote Sensing*, 52(1), doi:
1317 10.1109/TGRS.2013.2255880.

1318 Rogers, N. C., and Quegan, S. (2014). The accuracy of Faraday rotation estimation in satellite
1319 Synthetic Aperture Radar images, *IEEE Trans. Geosci. Remote Sensing*, 52(8), 4799 – 4807, doi:
1320 [10.1109/TGRS.2013.2284635](https://doi.org/10.1109/TGRS.2013.2284635)

1321 Rosenqvist, A., Shimada, M., Suzuki, S., Ohgushi, F., Tadono, T., Watanabe, M., et al. (2014).
1322 Operational performance of the ALOS global systematic acquisition strategy and observation plans
1323 for ALOS-2 PALSAR-2, *Remote Sens. Env.* 155, 3-12, doi.org/10.1016/j.rse.2014.04.011.

1324 Ru, X., Liu, Z., Huang, Z., and Jiang, W. (2016). Normalized residual-based constant false-alarm rate
1325 outlier detection. *Pattern Recognition Letters*, 69, 1-7.

1326 Ryan C. M., Hill T. C., Woollen E., Ghee C., Mitchard E. T. A. , Cassells G, Grace J, Woodhouse IH,
1327 Williams M. (2012). Quantifying small-scale deforestation and forest degradation in African
1328 woodlands using radar imagery. *Global Change Biology* 18, 243-257.

1329 Saatchi, S., Marlier, M., Chazdon, R. L., Clark, D B., and Russell, A. (2011). Impact of spatial
1330 variability of tropical forest structure on radar estimation of aboveground biomass, *Remote Sensing of*
1331 *Environment*, 115(11), 2836-2849, doi.org/10.1016/j.rse.2010.07.015.

1332 Saatchi, S. S., Harris, N. L., Brown, S., Lefsky, M., Mitchard, E. T. A., Salas, W., et al., (2011).
1333 Benchmark map of forest carbon stocks in tropical regions across three continents, *Proceedings of the*
1334 *National Academy of Sciences*, **108** (24), 9899–9904.

1335 Sandberg, G., Ulander, L. M. H., Holmgren, J., Fransson, J. E. S., & Le Toan, T. (2011). L- and P-
1336 band backscatter intensity for biomass retrieval in hemiboreal forest, *Remote Sensing of the*
1337 *Environment* 115, 2874-2886.

1338 Sandberg, G., Ulander, L. M. H., Wallerman, J., and Fransson, J.E.S. (2014). Measurements of forest
1339 biomass change using P-band SAR backscatter, *IEEE Trans. Geosci. Remote Sensing*, 52(10), 6047-
1340 6061.

1341 Santoro, M., Beer, C., Cartus, O., Schmullius, C., Shvidenko, A., McCallum, I., et al. (2011).
1342 Retrieval of growing stock volume in boreal forest using hyper-temporal series of Envisat ASAR
1343 ScanSAR backscatter measurements. *Remote Sens. Environ.*, 115(2), 490-507.

1344 Santoro, M., Cartus, O., Fransson, J. E. S., Shvidenko, A. , McCallum, I., Hall, R. J., et al. (2013).
1345 Estimates of forest growing stock volume for Sweden, Central Siberia and Québec using Envisat
1346 Advanced Synthetic Aperture Radar backscatter data. *Remote Sensing*, 5(9), 4503-4532.

1347 Scharf, L. L. (1991). *Statistical signal processing: detection, estimation, and time series analysis*.
1348 [Boston: Addison–Wesley. ISBN 0-201-19038-9.](#)

1349 Schimel, D., Pavlick, R., Fisher, J.B., Asner, G.P., Saatchi, S. S., Townsend, P., et al. (2015).
1350 Observing terrestrial ecosystems and the carbon cycle from space, *Global Change Biology*, 21, 1762-
1351 1776.

1352 Schmillius, C., Matejka, E., Pathe, C., Santoro, M., Cartus, O., Wiesmann, A., et al. (2017). DUE
1353 GlobBiomass Final Report, ESA-ESRIN Contract No. 4000113100/14/L_NB.

1354 Schlund, M., Scipal, K., and Quegan, S. (2018). Assessment of a power law relationship between P-
1355 band SAR backscatter and aboveground biomass and its implications for BIOMASS mission
1356 performance, *IEEE Jnl. Selected Topics in Applied Earth Observations and Remote Sensing*, 11,
1357 3538-3547, doi: [10.1109/JSTARS.2018.2866868](#).

1358 Skonieczny, C., Paillou, P., Bory, A., Bayon, G., Biscara, et al. (2015). African humid periods
1359 triggered the reactivation of a large river system in Western Sahara, *Nature Comm.*, Nov. 10th.

1360 Smallman, T. L., Exbrayat, J.-F., Mencuccini, M., Bloom, A., and Williams, M. (2017). Assimilation
1361 of repeated woody biomass observations constrains decadal ecosystem carbon cycle uncertainty in
1362 aggrading forests, *J. Geophys. Res. Biogeosciences*, 122, 528-545.

1363 Smith-Jonforsen, G., Folkesson, K., Hallberg, B., and Ulander, L. M. H. (2007). Effects of forest
1364 biomass and stand consolidation on P-band backscatter, *IEEE Geosci. Remote Sensing Letts.*, 4(4),
1365 669-673.

1366 Soja, M. J., Sandberg, G., and Ulander, L. M. H. (2013). Regression-based retrieval of boreal forest
1367 biomass in sloping terrain using P-band SAR, *IEEE Trans. Geosci. Remote Sens.*, 51(5), 2646-2665.

1368 Soja, M. J., Askne, J. I. H., and Ulander, L. M. H. (2017). Estimation of boreal forest properties from
1369 TanDEM-X data using inversion of the interferometric water cloud model, *IEEE Geosci. Remote*
1370 *Sensing Letts.*, 14(7), 997-1001.

1371 Soja, M. J., d'Alessandro, M. M., Quegan, S., Tebaldini, S., and Ulander, L. M. H. (2018). Model-
1372 based estimation of tropical forest biomass from notch-filtered P-band SAR backscatter, *Proc. IEEE*
1373 *Int. Geosci. Remote Sensing Symp. (IGARSS 2018)*, Valencia.

1374 Tang, S. (2018). Quantifying Differences in Forest Structures with Quantitative Structure Models
1375 from TLS Data, MSc Thesis, University College London.

1376 Tebaldini, S., Mariotti d'Alessandro, M., Kim, J.-S., Papathanassiou, K. (2017). Ionosphere vertical
1377 profiling from BIOMASS multisquint InSAR, *Proc. IEEE Int. Geosci. Remote Sensing Symp.*
1378 *(IGARSS 2017)*, Fort Worth (USA).

1379 Tebaldini S. and Rocca, F. (2012). Multibaseline polarimetric SAR tomography of a boreal forest at
1380 P- and L-bands, *IEEE Trans. Geosci. Remote Sens.*, 50(1), 232-246.

1381 Thomas, S. C., and Martin, A. R. (2012). Carbon content of tree tissues: a synthesis, *Forests*, 3, 332-
1382 352, doi:10.3390/f3020332.

1383 Thurner, M., Beer, C., Santoro, M., Carvalhais, N., Wutzler, T., Schepaschenko, D., et al. (2014).
1384 Carbon stock and density of northern boreal and temperate forests. *Global Ecology and*
1385 *Biogeography*, 23(3), 297-310.

1386 Thurner, M., Beer, C., Ciais, P., Friend, A.D., Ito, A., et al. (2017). Evaluation of climate-related
1387 carbon turnover processes in global vegetation models for boreal and temperate forests, *Global*
1388 *Change Biology*, 23, 3076–3091.

1389 Treuhft, R. N., Madsen, S. N., Moghaddam, M., and van Zyl, J. J. (1996). Vegetation characteristics
1390 and underlying topography from interferometric data, *Radio Sci.*, 31, 1449-1495.

1391 Truong-Loi, M.-L., Saatchi, S., and Jaruwatanadilok, S. (2015). Soil moisture estimation under
1392 tropical forests using UHF radar polarimetry, *IEEE Trans. Geosci. Remote Sens.*, 53(4), 1718–1727.

1393 Ulander, L. M. H., Gustavsson, A., Flood, B., Murdin, D., Dubois-Fernandez, P., Dupuis, X., et al.
1394 (2011a). BioSAR 2010: Technical Assistance for the Development of Airborne SAR and Geophysical
1395 Measurements during the BioSAR 2010 Experiment, Final Report, ESA contract no.
1396 4000102285/10/NL/JA/ef.

1397 Ulander, L.M.H., Sandberg, G. & Soja, M.J. (2011b). Biomass retrieval algorithm based on P-band
1398 BioSAR experiments of boreal forest, Proc. 2011 IEEE International Geosci. Remote Sensing Symp.,
1399 Vancouver, Canada, 4245-4248.

1400 Ulander, L. M. H., Monteith, A. R., Soja, M. J., and Eriksson, L. E. B. (2018). Multiport vector
1401 network analyzer radar for tomographic forest scattering measurements, IEEE Geosci. Remote
1402 Sensing Letters, 15(12), 1897 – 1901.

1403 UNFCCC (2016). Key decisions relevant for reducing emissions from deforestation and forest
1404 degradation in developing countries (REDD+), Decision booklet REDD+, UNFCCC secretariat,
1405 February 2016.

1406 Villard, L., and Le Toan, T. (2015). Relating P-band SAR intensity to biomass for tropical dense
1407 forests in hilly terrain: γ^0 or t^0 ?, IEEE Jnl. Selected Topics in Applied Earth Observations and Remote
1408 Sensing, 8(1), 214-223.

1409 Warszawski, L., Frieler, K., Huber, V., Piontek, F., Serdeczny, O., and Schewe, J. (2014). The Inter-
1410 Sectoral Impact Model Intercomparison Project (ISI-MIP): Project framework, PNAS, 111(9), 3228-
1411 3232; <https://doi.org/10.1073/pnas.1312330110>.

1412 Wessel, B., Huber, M., Wohlfart, C., Marschalk, U., Kosmann, D., Roth, A. (2018). Accuracy
1413 assessment of the global TanDEM-X Digital Elevation Model with GPS data, ISPRS Jnl.
1414 Photogrammetry and Remote Sensing, 139, 171–182.

1415 Williams, M, Hill, T.C., and Ryan C.M. (2013). Using biomass distributions to determine probability
1416 and intensity of tropical forest disturbance, Plant Ecology and Diversity, 6, 87-99.

1417 World Bank, Wood-Based Biomass Energy Development for Sub-Saharan Africa: Issues and
1418 Approaches (2011). The International Bank for Reconstruction and Development, The World Bank
1419 Group, Washington, D.C., U.S.A.

1420 Wright, P., Quegan, S., Wheadon, N., and Hall, D. (2003). Faraday rotation effects on L-band
1421 spaceborne SAR data, IEEE Trans. Geosci. Remote Sensing, 41(12), 2735-2744.

1422

1423 **Figure captions**

1424 **Fig. 1.** Global ecological regions of the world (FAO 2012) with the area affected by Space Objects
1425 Tracking Radar (SOTR) stations highlighted in yellow. Only land areas between 65° South and 85°
1426 North are represented (figure reproduced courtesy of Joao Carreiras).

1427 **Fig. 2.** P-band backscatter at HV polarisation (γ_{HV}^0) over tropical and boreal forests against the
1428 biomass of in situ reference plots. Data from Paracou, French Guiana, were acquired by the SETHI
1429 SAR system in 2011 (Dubois-Fernandez et al., 2012), those from La Selva, Costa Rica, in 2004 by the
1430 AIRSAR system (Antonarakis et al., 2011) and those from Remningstorp, Sweden, by the E-SAR
1431 system in 2007 (Sandberg et al., 2011).

1432 **Fig. 3.** Estimated AGB using the approach described in the text against AGB estimated from in situ
1433 and airborne laser scanning at the La Lopé site in Gabon during the AfriSAR campaign. The running
1434 average given by the blue line indicates only a small positive bias across the whole range of AGB.
1435 ROI denotes Region of Interest.

1436 **Fig. 4.** Plot of HV backscatter intensity at height 30 m above the ground measured by tomography
1437 against in situ AGB in 1 ha plots at tropical forest sites investigated during the TropiSAR (Paracou
1438 and Nouragues) and AfriSAR (Lopé, Rabi, Mondah) campaigns.

1439 **Fig. 5.** Forest height map obtained from inverting P-band Pol-InSAR data acquired over the Pongara
1440 National Park, Gabon, in the framework of the AfriSAR campaign in February 2017.

1441 **Fig. 6.** (Top) Pair of repeat-pass PALSAR-2 images acquired on 8 August 2014 and 7 August 2015
1442 displayed in Pauli image format (red = HH + VV; blue = HH - VV; green = 2HV) and slant range

1443 geometry. (Bottom left) Detection of change at 99% significance level; changed pixels are marked as
1444 black. (Bottom right) Image from 8 August 2014 with changed pixels marked as red.

1445 **Fig 7.** Relative difference between modelled carbon turnover rates and turnover rates inferred from
1446 observations. 1.0 means modelled rate is 100% higher (from Thurner et al., 2017). Red boxes labelled
1447 b (boreal) and t (temperate) were analysed further in Thurner et al. (2017) to explain these
1448 discrepancies (figure reproduced courtesy of Martin Thurner).

1449 **Fig. 8.** The relative reduction in the size of the 95% confidence interval of estimated vegetation
1450 carbon turnover times when using a prior value for biomass at each pixel compared to a run without a
1451 biomass prior. Turnover times were estimated using the CARDAMOM system. The darker areas
1452 show where reduction in relative uncertainty is largest.

1453 **Figure 9.** Left: SPOT image of the Ksar Ghilane oasis region in southern Tunisia: palaeo-channels are
1454 hidden by aeolian sand deposits. Middle: ALOS-2 L-band radar image, showing sub-surface features
1455 but blurred by the return from the superficial sand layer. Right: SETHI P-band radar image, clearly
1456 revealing sub-surface hydrological features.

1457 **Fig. 10.** Coverage of ESA and NASA-ISRO satellite measurements of forest structure and above-
1458 ground biomass (AGB). The background shows the global coverage area of NISAR, which will be
1459 sensitive to AGB values < 100 t/ha (green and yellow). BIOMASS coverage includes the tropical belt,
1460 the temperate and boreal zones of Asia, and the southern hemisphere, while the GEDI Lidar will
1461 sample latitudes between $\pm 51.5^\circ$. These two sensors will cover the full range of forest AGB
1462 providing measurements where $AGB > 100$ t/ha (red), so inaccessible to NISAR.

1463

*Highlights (for review)

- BIOMASS will be the first spaceborne P-band mission
- Global estimates of forest biomass and height, subject to US DoD restrictions
- The first systematic use of Pol-InSAR to measure forest height from space
- The first systematic use of spaceborne SAR tomography
- Sub-surface imaging, icesheet motion estimation and a bias-free DTM

1 **The European Space Agency BIOMASS mission: measuring forest above-ground biomass from**
2 **space**

3

4 **Shaun Quegan¹, Thuy Le Toan², Jerome Chave³, Jorgen Dall⁴, Jean-François Exbrayat⁵, Dinh**
5 **Ho Tong Minh⁶, Mark Lomas¹, Mauro Mariotti D'Alessandro⁷, Philippe Paillou⁸, Kostas**
6 **Papathanassiou⁹, Fabio Rocca⁷, Sassan Saatchi¹⁰, Klaus Scipal¹¹, Hank Shugart¹², T. Luke**
7 **Smallman⁵, Maciej J. Soja¹³, Stefano Tebaldini⁷, Lars Ulander¹⁴, Ludovic Villard² and Mathew**
8 **Williams⁵**

9 1. University of Sheffield and National Centre for Earth Observation, UK

10 2. Centre d'Etudes Spatiales de la Biosphère, CNRS-CNES-Université Paul Sabatier-IRD,
11 Toulouse, France

12 3. Université Toulouse III Paul Sabatier, Laboratoire Evolution & Diversité Biologique, Toulouse,
13 France

14 4. Technical University of Denmark, National Space Institute, Denmark

15 5. University of Edinburgh, School of GeoSciences and National Centre for Earth
16 Observation, UK

17 6. UMR TETIS, IRSTEA, University of Montpellier, 34093 Montpellier, France

18 7. Dipartimento di Elettronica Informazione e Bioingegneria, Politecnico di Milano, Italy

19 8. Université de Bordeaux, Pessac Cedex, France

20 9. German Aerospace Center e.V. (DLR), Wessling, Germany

21 10. Jet Propulsion Laboratory, Pasadena, USA
22 10. Mission Science Division, ESA-ESTEC, the
Netherlands

23 11. Mission Science Division, ESA-ESTEC, the Netherlands

24 12. University of Virginia, Charlottesville, Virginia USA

25 13. MJ Soja Consulting, Hobart, Tasmania, Australia and University of Tasmania, Hobart,
26 Tasmania , Australia

27 14. Chalmers University of Technology, Sweden

28

29 Corresponding author

30 Shaun Quegan

31 School of Mathematics and Statistics

32 Hicks Building, University of Sheffield,

33 Hounsfield Rd

34 Sheffield S3 7RH

35 UK

36 Tel: +44 114 2223778

Fax: + 44 114 2223809

37 Email: s.quegan@sheffield.ac.uk

38

39 **Abstract**

40 The primary objective of the European Space Agency's 7th Earth Explorer mission, BIOMASS, is to
41 determine the worldwide distribution of forest above-ground biomass (AGB) in order to reduce the
42 major uncertainties in calculations of carbon stocks and fluxes associated with the terrestrial
43 biosphere, including carbon fluxes associated with Land Use Change, forest degradation and forest
44 regrowth. To meet this objective it will carry, for the first time in space, a fully polarimetric P-band
45 synthetic aperture radar (SAR). Three main products will be provided: global maps of both AGB and
46 forest height, with a spatial resolution of 200 m, and maps of severe forest disturbance at 50 m
47 resolution (where "global" is to be understood as subject to Space Object tracking radar restrictions).
48 After launch in 2022, there will be a 3-month commissioning phase, followed by a 14-month phase
49 during which there will be global coverage by SAR tomography. In the succeeding interferometric
50 phase, global polarimetric interferometry Pol-InSAR coverage will be achieved every 7 months up to
51 the end of the 5-year mission. Both Pol-InSAR and TomoSAR will be used to eliminate scattering
52 from the ground (both direct and double bounce backscatter) in forests. In dense tropical forests AGB
53 can then be estimated from the remaining volume scattering using non-linear inversion of a
54 backscattering model. Airborne campaigns in the tropics also indicate that AGB is highly correlated
55 with the backscatter from around 30 m above the ground, as measured by tomography. In contrast,
56 double bounce scattering appears to carry important information about the AGB of boreal forests, so
57 ground cancellation may not be appropriate and the best approach for such forests remains to be
58 finalized. Several methods to exploit these new data in carbon cycle calculations have already been
59 demonstrated. In addition, major mutual gains will be made by combining BIOMASS data with data
60 from other missions that will measure forest biomass, structure, height and change, including the
61 NASA Global Ecosystem Dynamics Investigation lidar deployed on the International Space Station
62 after its launch in December 2018, and the NASA-ISRO NISAR L- and S-band SAR, due for launch
63 in 2022. More generally, space-based measurements of biomass are a core component of a carbon
64 cycle observation and modelling strategy developed by the Group on Earth Observations. Secondary
65 objectives of the mission include imaging of sub-surface geological structures in arid environments,
66 generation of a true Digital Terrain Model without biases caused by forest cover, and measurement of

67 glacier and icesheet velocities. In addition, the operations needed for ionospheric correction of the
68 data will allow very sensitive estimates of ionospheric Total Electron Content and its changes along
69 the dawn-dusk orbit of the mission.

70

71 **1. Introduction: The role of biomass in the global carbon cycle and climate**

72 For millennia, humanity has depended on woody biomass from forests as a source of materials and
73 energy (Rackham and Moody, 1996; Radkau, 2012), and this dependence shows no sign of abating.
74 For example, around a third of the world’s population relies on biomass for energy, and in sub-
75 Saharan Africa around 81% of the energy use by households is provided by burning woody biomass
76 (World Bank, 2011). At the same time, forest, and its associated biomass, has often been treated as an
77 impediment to development, and huge tracts have been cleared, and continue to be cleared, to make
78 way for agriculture, pasture and agro-forestry (FAO, 2016). However, a significant shift in the
79 relationship between mankind and biomass has occurred as climate change has become of pressing
80 international concern and the role of forest biomass within this process has become clearer (IPCC,
81 2007, 2013).

82 Climate change is intimately connected with the global carbon balance and the fluxes of greenhouses
83 gases, especially carbon dioxide (CO₂), between the Earth’s surface and the atmosphere
84 (Intergovernmental Panel on Climate Change (IPCC), 2007, 2013). In particular, an unequivocal
85 indication of man’s effect on our planet is the accelerating growth of atmospheric CO₂. The principal
86 contribution (around 88%) to this growth is emissions from fossil fuel burning, with most of the
87 remainder arising from Land Use Change in the tropics (Le Quéré, 2018). However, the increase in the
88 concentration of atmospheric CO₂ between 2007 and 2016 is only about half (44%) of the emissions.
89 Because CO₂ is chemically inert in the atmosphere, the “missing” half of the emissions must flow back
90 into the Earth’s surface. Current estimates (Le Quéré et al., 2018) suggest that around 28% of the total
91 emissions are taken up by the land and 22% by the oceans (leaving around 6% unaccounted for), but
92 there are large uncertainties in these values, especially the land uptake, whose value has usually been
93 estimated as a residual that ensures the total amount of carbon is conserved, as expressed in eq. (1):

94
$$U_{\text{land}} = E_{\text{ff}} + E_{\text{lb}} - (\Delta C_{\text{atmos}} + U_{\text{ocean}}). \quad (1)$$

95 Here E_{ff} denotes fossil fuel emissions; E_{lb} is net land biospheric emissions, comprising both Land Use
96 Change and ecosystem dynamics, and including alterations to biomass stocks linked to process
97 responses to climate change, nitrogen deposition and rising atmospheric CO_2 ; ΔC_{atmos} is the change in
98 atmospheric CO_2 ; and U_{land} and U_{ocean} are net average uptake by the land and ocean respectively. In eq.
99 (1) the quantities on the right-hand side are typically estimated on an annual basis or as a decadal
100 average, using a mixture of measurements and models, to yield U_{land} . However, in Le Quéré et al.
101 (2018) U_{land} is estimated independently using dynamic global vegetation models. Under both
102 approaches U_{land} has the largest uncertainty of any term in eq. (1), estimated as 0.8 GtC/yr, which is
103 26% of its estimated value of 3.0 GtC/yr (1 GtC = 10^9 t of C which is equivalent to 3.67×10^9 t of CO_2).
104 Moreover, the Land Use Change flux (which is the difference between emissions from forest loss and
105 uptake of CO_2 by forest regrowth) has an uncertainty of 0.7 GtC/yr, which is 54% of its estimated
106 value of 1.3 GtC/yr. Since the fractional carbon content of dry biomass is around 50% (though with
107 significant inter-species differences [Thomas and Martin, 2012]), biomass change is a fundamental
108 component in these two land fluxes, controlling the emissions from forest disturbance and the uptake
109 of carbon by forest growth (e.g. Pan et al. 2011). This is why above-ground biomass (AGB) is
110 recognised as an Essential Climate Variable (ECV) within the Global Climate Observing System
111 (2015, 2017).

112 Climate change concerns have therefore made it imperative to obtain accurate estimates of biomass
113 and its changes. Unfortunately, where this information is most needed – the tropics – is where almost
114 no data have been gathered (Schimel et al., 2015). This is in contrast to forests in the temperate and
115 southern parts of the boreal zones whose economic importance has driven the development of
116 extensive national inventories (although there are vast areas of Alaska, Northern Canada, and East
117 Eurasia that do not have forest inventories because of their low economic importance). The tropical
118 forests cover an enormous area (~ 18 million km^2) and offer huge logistical challenges for ground-
119 based biomass inventory. They are also crucial in political efforts to mitigate climate change. In
120 particular, the United Nations Convention on Climate Change (UNFCCC) through its Reduction of

121 Emissions from Deforestation and Degradation (REDD+) initiative (UNFCCC, 2016) aims to use
122 market and financial incentives to transfer funds from the developed world to the developing countries
123 in the tropical belt to help them reduce emissions by preservation and management of their forests
124 (UN-REDD Programme, 2008).

125 Estimates of biomass losses have focused on deforestation, i.e. conversion of forest land to other land
126 use, which results in complete removal of AGB. However, also significant, but missing from most
127 current estimates, is forest degradation. This is the loss of part of biomass, for instance removal of
128 large stems for timber or of understorey plants for replacement by cocoa, or through increased fire
129 along forest edges.

130 UN-REDD and related programmes have given significant impetus to the acquisition of more in situ
131 data in developing countries and this adds to the information available in the periodic reports of the
132 United Nations (UN) Food and Agriculture Organisation (FAO) (FAO 2006, 2010, 2016). However
133 national data in many cases have large gaps, sampling biases, inconsistency of methods, lack spatially
134 explicit information and contain unrepresentative samples, particularly in developing countries. As a
135 result, major efforts have been made to formulate more consistent global approaches that combine
136 forest inventory and satellite data to estimate AGB. Such endeavours have been greatly hampered by
137 the fact that, up until the launch of the Global Ecosystem Dynamics Investigation (GEDI) instrument
138 (see below), there has never been any spaceborne sensor designed to measure biomass, so space-based
139 estimates of biomass have relied on opportunistic methods applied to non-optimal sensors, with the
140 limitations this implies.

141 In the tropics, the most significant developments have been based on forest height estimates derived
142 from the Geoscience Laser Altimeter System (GLAS) onboard the Ice, Cloud and land Elevation
143 Satellite (ICESat) before its failure in 2009 (Lefsky, 2005, 2010). Combining GLAS data with other
144 EO and environmental datasets and in situ biomass measurements has led to the production of two
145 pan-tropical biomass maps (Saatchi et al. 2010; Baccini et al. 2012) at grid scales of 1 km and 500 m
146 respectively; differences between these maps and differences between the maps and in situ data are

147 discussed in Mitchard et al. (2013, 2014). Refinements of these maps have been produced by
148 Avitabile et al. (2016) and Baccini et al. (2017) based on essentially the same satellite datasets.

149 For boreal and temperate forests, methods have been developed to estimate Growing Stock Volume
150 (GSV, defined as the volume of wood in all living trees in an area with diameter at breast height above
151 a given threshold) from very long time series of C-band Envisat satellite radar data (Santoro et al.
152 2011). Multiplying these GSV estimates by wood density allowed Thurner et al. (2014) to estimate the
153 carbon stock of forests north of 30°N. Reliable GSV estimates using these methods are only possible
154 at spatial resolutions much coarser than the underlying radar data: by averaging to 0.5°, the relative
155 RMS difference between estimated GSV and reference data was consistently found to lie in the range
156 20–30% (Santoro et al. 2013). Further refinements to the methodology and its combination with
157 ALOS PALSAR-2 data are given in the Final Report of the ESA GlobBiomass project (Schmullius et
158 al., 2017).

159 L-band radar offers access to biomass values up to around 100 t/ha before losing sensitivity (e.g.
160 Mitchard et al., 2009). Under the JAXA Kyoto and Carbon Initiative, the ALOS L-band PALSAR-1
161 acquired a systematic five-year archive of forest data before its failure in April 2011 (Rosenqvist et
162 al., 2014). PALSAR-2 launched in spring 2014 and has continued this systematic acquisition strategy,
163 but current JAXA data policy makes scene data very expensive. Annual mosaics are freely available
164 and have been used to map woodland savanna biomass at continental scale (Bouvet et al., 2018), but
165 the mosaics combine data from different times and environmental conditions, so further processing
166 may be needed to exploit them for biomass estimation (Schmullius et al., 2017). L-band data will also
167 be acquired by the two Argentinian Microwave Observation Satellites (SAOCOM), the first of which
168 was launched on October 8, 2018, with the second due in 2019. Their main objectives are
169 measurements of soil moisture and monitoring of hazards, such as oil spills and floods, and their value
170 for global forest observations is not yet clear.

171 C-band (Sentinel-1, Radarsat) and X-band (Tandem-X) radar instruments are in orbit but at these
172 frequencies most of the backscatter is from the leaves and small twigs, so they have limited value for
173 biomass estimation except within the context of long time series at C-band (Santoro et al. 2011) and,

174 for TanDEM-X, when a ground Digital Terrain Model (DTM) is available and the height-to-biomass
175 allometry is robust (Persson et al., 2017; Askne et al., 2017).

176 An exciting new development is the deployment on the International Space Station of the NASA
177 GEDI lidar instrument after its launch on December 5, 2018 (see Section 10). This mission aims to
178 sample forest vertical structure across all forests between 51.5° S and 51.5° N, from which estimates
179 of the mean and variance of AGB on a 1 km grid will be derived. In addition, ICESat-2 launched on
180 September 15, 2018; although it is optimised for icesheet, cloud and aerosol applications, and uses a
181 different technical approach from ICESat-1 based on photon counting, preliminary results suggest that
182 it can provide information on both forest height and structure.

183 It is against this scientific and observational background that BIOMASS was selected by the
184 European Space Agency (ESA) in 2013 as its 7th Earth Explorer mission, and the satellite is now
185 under production by a consortium led by Airbus UK for launch in 2022. The initial mission concept is
186 described in Le Toan et al. (2011), but there have been major developments since that time in almost
187 all aspects of the mission: the measurement and calibration concepts, the scientific context, the
188 methods to recover biomass from the satellite data, the exploitation of biomass in carbon cycle and
189 climate modelling, the availability of P-band airborne campaign data and high quality in situ data, and
190 the overall capability to estimate biomass from space. It is therefore timely to provide a
191 comprehensive description of the current mission concept, and this paper sets out to do so.

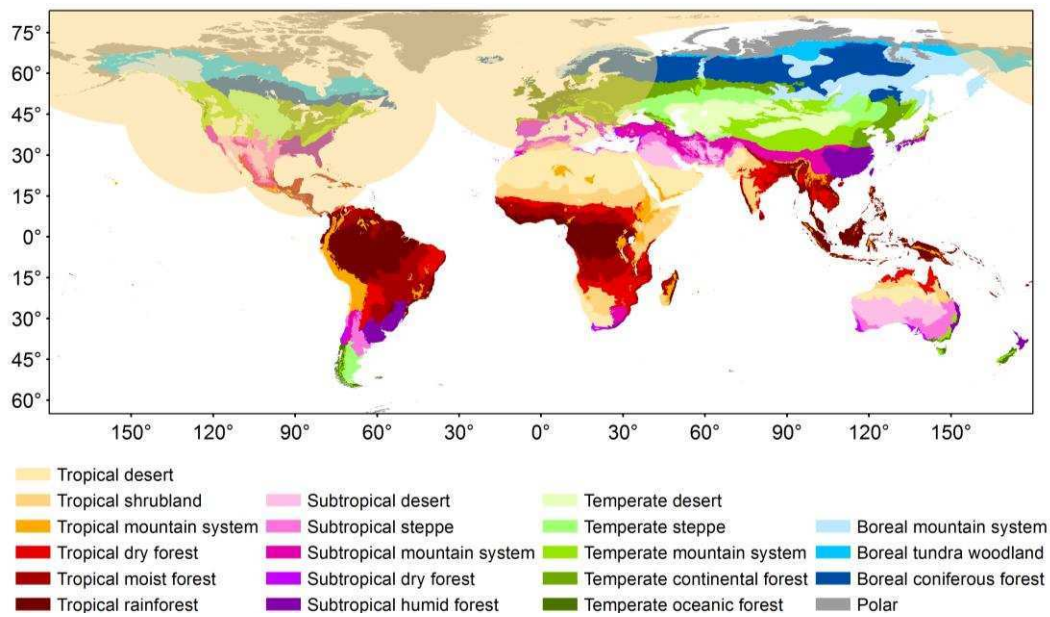
192 After a review of the mission objectives (Section 2), the associated measurement techniques
193 (polarimetry, polarimetric interferometry [Pol-InSAR] and SAR tomography [TomoSAR]) are
194 described in Section 3. Pol-InSAR and TomoSAR require the combination of multi-temporal stacks
195 of data; this imposes very strong conditions on the BIOMASS orbit pattern, with significant
196 consequences for the production of global biomass products (Section 4). The orbit pattern also
197 imposes strong requirements on the ability of the AGB and height inversion techniques, discussed in
198 Section 5, to adapt to changing environmental conditions. Section 6 deals with the use of BIOMASS
199 data to estimate severe forest disturbance, while Section 7 describes the development of the reference
200 datasets to be used for algorithm calibration and product validation. In Section 8 we discuss

201 developments in how BIOMASS data can be used to estimate key carbon cycle and climate variables.
202 Section 9 addresses a range of secondary objectives. Section 10 provides a view on how BIOMASS
203 complements other upcoming missions devoted to forest structure and biomass, in particular the
204 GEDI lidar and the NASA-ISRO NISAR L- and S-band mission. Finally, Section 11 discusses how
205 BIOMASS will contribute to an overall system for measuring biomass and its changes in the context
206 of a global carbon cycle management scheme and presents our general conclusions.

207 **2. BIOMASS mission objectives and data properties**

208 The primary objective of the BIOMASS mission is to determine the worldwide distribution of forest
209 above-ground biomass (AGB) in order to reduce the major uncertainties in calculations of carbon
210 stocks and fluxes associated with the terrestrial biosphere, including carbon fluxes associated with
211 Land Use Change, forest degradation and forest regrowth. In doing so, it will provide support for
212 international agreements such as REDD+ and UN Sustainable Development Goals (#13: climate
213 action; #15: life on land). In addition it has several secondary objectives, including mapping sub-
214 surface geology, measuring terrain topography under dense vegetation and estimating glacier and
215 icesheet velocities (ESA, 2012).

216 Although BIOMASS aims at full global coverage, it will at least cover forested areas between 75° N
217 and 56° S, subject to US Department of Defense Space Object Tracking Radar (SOTR) restrictions.
218 These restrictions do not currently allow BIOMASS to operate within line-of-sight of the SOTR
219 radars and mainly exclude the North American continent and Europe (Fig. 1, reproduced from
220 Carreiras et al., 2017). For secondary applications, if global coverage is not possible, data will be
221 collected on a best effort basis after covering the primary objectives, with priorities defined as in ESA
222 (2015).



223

224 **Fig. 1.** Global ecological regions of the world (FAO 2012) with the area affected by Space Objects

225 Tracking Radar (SOTR) stations highlighted in yellow. Only land areas between 65° South and 85°

226 North are represented (figure reproduced courtesy of Joao Carreiras).

227

228 The BIOMASS data product requirements to meet the primary mission objectives are (ESA, 2015):

229

1. Above-ground forest biomass (AGB), defined as the dry weight of live organic matter above
 230 the soil, including stem, stump, branches, bark, seeds and foliage woody matter per unit area,
 231 expressed in $t\ ha^{-1}$ (FAO, 2009). It does not include dead mass, litter and below-ground
 232 biomass. Biomass maps will be produced with a grid-size of 200m x 200m (4 ha).

233

2. Forest height, defined as upper canopy height according to the H100 standard used in forestry
 234 expressed in m, mapped using the same 4 ha grid as for biomass. H100 is defined as the
 235 average height of the 100 tallest trees/ha (Philip, 1994).

236

3. Severe disturbance, defined as an area where an intact patch of forest has been cleared,
 237 expressed as a binary classification of intact vs deforested or logged areas, with detection of
 238 forest loss being fixed at a given level of statistical significance.

239 Further properties of these products are defined in Table 1. Note that:

- 240 • The biomass and height products will be produced on a 4 ha grid, while the disturbance
 241 product is at the full resolution of the instrument after averaging to 6 looks in azimuth, i.e.,
 242 around 50 m x 50 m. This is because the large changes in backscatter associated with forest
 243 clearance mean that disturbance can be detected using less precise estimates of the
 244 polarimetric covariance and coherence matrices than are needed for biomass and height
 245 estimation.
- 246 • If the true AGB exceeds 50 t ha⁻¹ then the RMS error (RMSE) of its estimate is expected to
 247 depend on biomass and be less than AGB/5. For all values of AGB < 50 t ha⁻¹ the RMSE is
 248 stipulated to be 10 t ha⁻¹ or better, though it is likely that changes in ground conditions, such
 249 as soil moisture, may cause the RMSE to increase beyond this value. Similarly, the RMSE of
 250 estimates of forest height should be less than 30% of the true forest height for trees higher
 251 than 10 m.
- 252 • Below-ground biomass cannot be measured by BIOMASS (or any other remote sensing
 253 instrument), but can be inferred from above-ground biomass using allometric relations
 254 combined with climate data (Cairn et al., 1997; Mokany et al., 2006; Thurner et al., 2014). In
 255 particular, Ledo et al. (2018) used an extensive tropical, temperate and boreal forest dataset to
 256 develop a regression, with just tree size and mean water deficit as predictor variables, which
 257 explains 62% of the variance in the root-to-shoot ratio. Therefore, throughout this paper,
 258 ‘biomass’ denotes ‘above-ground biomass’.

259 **Table 1** Summary of primary BIOMASS Level 2 products. Achieving global coverage requires 425
 260 days during the initial Tomographic Phase and 228 days for each cycle of the subsequent
 261 Interferometric Phase. RMSE indicates Root Mean Square Error. “Global” is to be understood as
 262 subject to Space Object Tracking Radar restrictions (Carreiras et al., 2017).

263

Level 2 Product	Definition	Information Requirements
Forest	Above-ground biomass expressed	• 200 m resolution

biomass	in $t\ ha^{-1}$.	<ul style="list-style-type: none"> • RMSE of 20% or $10\ t\ ha^{-1}$ for biomass $< 50\ t\ ha^{-1}$ • 1 biomass map every observation cycle • global coverage of forested areas
Forest height	Upper canopy height defined according to the H100 standard	<ul style="list-style-type: none"> • 200 m resolution • accuracy required is biome-dependent, but RMSE should be better than 30% for trees higher than 10 m • 1 height map every observation cycle • global coverage of forested areas
Severe disturbance	Map product showing areas of forest clearance	<ul style="list-style-type: none"> • 50 m resolution • detection at a specified level of significance • 1 map every observation cycle • global coverage of forested areas

264

265 3. The BIOMASS system and measurement techniques

266

267 BIOMASS will be a fully polarimetric SAR mission operating at P-band (centre frequency 435 MHz)
268 with 6 MHz bandwidth, as permitted by the International Telecommunications Union under a
269 secondary allocation (the primary allocation is to the SOTR system). The choice of P-band is
270 mandatory for measuring biomass with a single radar satellite (necessary for affordability within the
271 ESA cost envelope) for three main reasons (ESA, 2008, 2012; Le Toan et al., 2011):

- 272 1. P-band radiation can penetrate the canopy in all forest biomes and interacts preferentially with
273 the large woody vegetation elements in which most of the biomass resides;
- 274 2. Backscatter at P-band is more sensitive to biomass than at higher frequencies (X-, C-, S- and
275 L-bands); lower frequencies (e.g. VHF) display even greater sensitivity (Fransson et al.,
276 2000) but present formidable challenges for spaceborne SAR because of ionospheric effects;

277 3. P-band displays high temporal coherence between passes separated by several weeks, even in
278 dense forest (Ho Tong Minh et al., 2012), allowing the use of Pol-InSAR to estimate forest
279 height and retrieval of forest vertical structure using tomography.

280 Here (1) is the crucial physical condition: it underlies the sensitivity in point (2) and, through the
281 relative positional stability of the large woody elements, combined with the greater phase tolerance at
282 longer wavelengths, permits the long-term coherence needed for (3).

283 The satellite will carry a 12 m diameter reflector antenna, yielding a single-look azimuth resolution of
284 ~7.9 m. A polarimetric covariance product will also be generated by averaging 6 looks in azimuth,
285 giving pixels with azimuth resolution ~50 m. Because of the allotted 6 MHz bandwidth, the single-
286 look slant range resolution will be 25 m, equivalent to a ground range resolution of 59.2 m at an
287 incidence angle of 25°. Roll manoeuvres will allow the satellite to successively generate three sub-
288 swaths of width 54.32, 54.41 and 46.06 km, giving a range of incidence angles across the combined
289 swath from 23° to 33.9°. It will be in a sun-synchronous orbit with a near dawn-dusk (06:00 ± 15 min)
290 equatorial crossing time; the Local Time of the Ascending Node (LTAN) will be on the dawn-side,
291 the system will be left-looking and the orbit inclination will be 98°, with the highest latitude in the
292 northern hemisphere attained on the night-side. This orbit is chosen to avoid the severe scintillations
293 that occur in the post-sunset equatorial ionosphere (Rogers et al., 2013). Observations will be made
294 during both the ascending and descending passes.

295 BIOMASS displays major advances compared to all previous SAR missions in its use of three
296 complementary technologies to provide information on forest properties: polarimetry (PolSAR), Pol-
297 InSAR and TomoSAR. All acquisitions will be fully polarimetric, i.e. the amplitude and phase of the
298 HH, VV, HV & VH channels will be measured (HV indicates horizontal polarization on transmit and
299 vertical polarization on receive, with the other channels being similarly defined). This is in itself an
300 advance, but BIOMASS will also be the first mission to systematically employ the Pol-InSAR
301 technique to measure forest height. Even more innovative is its tomographic capability, which will
302 allow three-dimensional imaging of forests.

303 The Tomographic Phase will immediately follow the initial 3-month Commissioning Phase, and will
304 provide tomographic mapping of all imaged forest areas. Global coverage requires 425 days (~14
305 months) in order to provide 7 passes, each separated by 3 days, for each tomographic acquisition. The
306 remainder of the 5-year mission will be taken up by the Interferometric Phase, during which 3 passes,
307 each separated by 3 days, will be combined in 3-baseline Pol-InSAR. Each cycle of the
308 Interferometric Phase will require 228 days (~7 months) to provide global coverage. Note that these
309 techniques are nested: the data gathered for tomography will yield multiple Pol-InSAR and PolSAR
310 measurements, and each Pol-InSAR image triplet also provides three PolSAR images.

311 Associated with the highly innovative measurement concepts of the mission are completely new
312 challenges in external calibration arising from the orbital pattern needed for the tomographic and Pol-
313 InSAR phases of the mission (Section 4), the strong effects of the ionosphere at P-band, and the lack
314 of pre-existing P-band data except over very limited parts of the globe. Together these create
315 problems that can only be solved by combining infrequent visits to instrumented calibration sites with
316 systematic exploitation of the properties of distributed targets and targets of opportunity. An overall
317 approach to addressing these problems, including ionospheric correction, radiometric and polarimetric
318 calibration, and providing the required geolocation accuracy is described in Quegan et al. (2018).

319 **4. The BIOMASS orbit and its implications**

320 In the Tomographic Phase, BIOMASS needs to be placed in a very precise repeat orbit in which a
321 given scene is imaged 7 times with 3-day spacing. These acquisitions will be from slightly different
322 positions separated by 15% of the critical baseline (i.e. 0.823 km) at the equator, which is necessary to
323 preserve coherence. In this orbit, it takes 18 days to acquire the 7 images needed for each of the 3 sub-
324 swaths, so that tomography over the full swath (comprising the 3 sub-swaths) occupies a period of 60
325 days. Once this has been achieved, a drift manoeuvre will raise the satellite in altitude and then return
326 it to its nominal altitude of 671.9 km. This allows the Earth to rotate below the satellite, and the next
327 tomographic acquisition period covers a new swath that is adjacent to the previous one. Repeating this
328 sequence $6 + 1/3$ times yields global coverage and takes 425 days (the extra third corresponds to
329 coverage in swath 1). The orbit pattern for the Interferometric Phase uses essentially the same

330 concept, but because only 3 images are needed to form the Pol-InSAR product, imaging a full swath
331 requires only 24 days, and global coverage takes 228 days.

332 These properties of the BIOMASS orbit pattern, driven by the requirement for global coverage using
333 coherent imaging techniques, have profound implications for biomass retrieval in time and space.
334 Acquisitions in adjacent swaths are separated by 2 months in the Tomographic Phase and by a little
335 less than a month in each cycle of the Interferometric Phase. Hence there are likely to be significant
336 changes in environmental conditions between different swaths that make up the global coverage. In
337 addition, because each cycle of the Interferometric Phase takes 7 months, the acquisitions become
338 steadily more out of phase with annual geophysical cycles, such as the Amazonian and West African
339 inundation cycles. This means that the BIOMASS inversion algorithms have to be sufficiently robust
340 that they are negligibly affected by environmental changes. Incomplete compensation for such
341 changes will manifest themselves as systematic differences between adjacent swaths or repeat swaths
342 gathered in different cycles. As an example, boreal forests freeze during winter and their backscatter
343 significantly decreases, so the winter season will most likely not be useful for biomass estimation.
344

345 **5. Forest AGB and height estimation techniques**

346
347 BIOMASS will exploit properties of all three SAR techniques, PolSAR, Pol-InSAR and TomoSAR,
348 to estimate biomass, while both Pol-InSAR and TomoSAR will provide estimates of forest height.
349 However, because BIOMASS will be the first spaceborne P-band SAR, the experimental data needed
350 to support the development and testing of these techniques is based on limited airborne and ground-
351 based measurements. Six major ESA airborne campaigns were carried out (BioSAR-1, -2 and -3 in
352 the boreal zone, and three in tropical ecosystems: TropiSAR in French Guiana, AfriSAR in Gabon
353 and Indrex-2 in Indonesia) using the E-SAR and F-SAR (DLR, Germany) and SETHI (ONERA,
354 France) P-band SARs (see Table 2, which includes the objectives of the campaigns and essential
355 properties of the test-sites). These campaigns have provided the most accurate and complete set of P-
356 band SAR (PolSAR, Pol-InSAR and TomoSAR) and associated in situ data currently available over

357 boreal and tropical forests. In addition, long-term continuous P-band tower-based measurements were
 358 made in French Guiana (Tropiscat), Ghana (Afriscat) and Sweden (Borealscat) to investigate diurnal
 359 and seasonal variations in backscatter and temporal coherence. Earlier P-band datasets from the
 360 NASA AirSAR system were also helpful, especially tropical forest data from Costa Rica, to extend
 361 the range of tropical biomass values (Saatchi et al., 2011), and NASA was heavily involved in the
 362 AfriSAR campaign, providing lidar coverage of the AfriSAR test-sites (Labrière et al., 2018). No
 363 specific ESA campaigns were conducted in temperate forests, but substantial amounts of tomographic
 364 data are available for such forests from experimental campaigns carried out by DLR.

365 **Table 2** Campaign data used in developing and testing BIOMASS retrieval algorithms.

366

Campaign	Objectives	Test sites	Time	Forest conditions
TropiSAR, SETHI (Dubois-Fernandez et al., 2012)	Biomass estimation in tropical forest; temporal stability of coherence	Paracou & Nouragues, French Guiana	Aug. 2009	Tropical rain forest, AGB 300-500 t/ha, lowland and hilly terrain
Indrex-2, E-SAR (Hajsek et al., 2009a) ; not tomographic	Height retrieval in tropical forest ; measurement of repeat-pass temporal decorrelation	Sungai-Wai & Mawas, Borneo, Indonesia	Nov. 2004	Tropical rain forest. Sungai-Wai: lowland, AGB \leq 600 t/ha; Mawas: peat swamp, AGB \leq 200 t/ha
Tropiscat: Ground-based high temporal resolution measurements (Koleck et al., 2012)	Measurement of long-term temporal coherence and temporal variation of backscatter in	Paracou, French Guiana	Aug. 2011 - Dec. 2012	Tropical rain forest, AGB ca. 400 t/ha

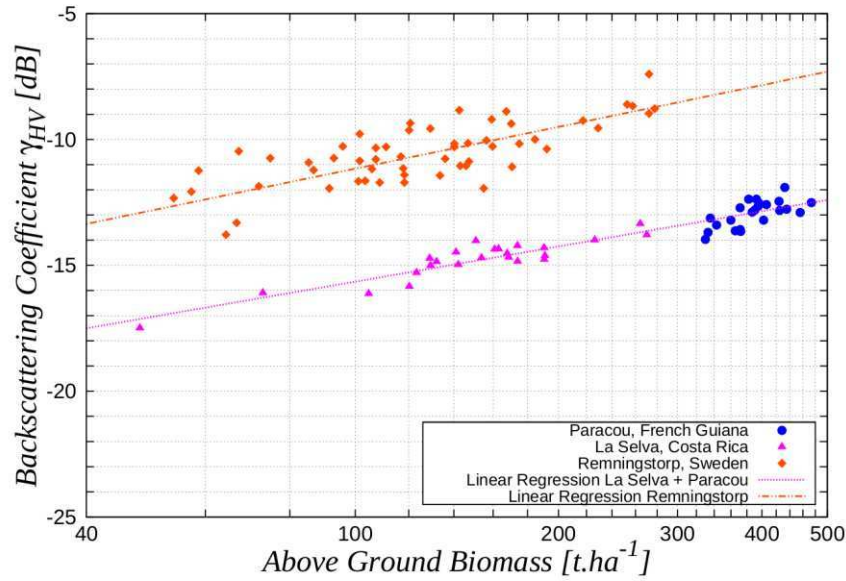
	tropical forest			
BioSAR-1, E-SAR (Hajnssek et al., 2008)	Biomass estimation and measurement of multi-month temporal decorrelation	Remningstorp, southern Sweden	Mar. - May 2007	Hemi-boreal forest, low topography, AGB ≤ 300 t/ha
BioSAR-2, E-SAR (Hajnssek et al., 2009b)	Topographic influence on biomass estimation	Krycklan, northern Sweden	Oct. 2008	Boreal forest, hilly, AGB ≤ 300 t/ha
BioSAR-3, E-SAR (Ulander et al., 2011a, b)	Forest change and multi-year coherence relative to BioSAR-1	Remningstorp, southern Sweden	Sept. 2010	Hemi-boreal forest, low topography, AGB ≤ 400 t/ha (more high biomass stands than in BIOSAR-1)
AfriSAR, SETHI and F-SAR	Biomass estimation in tropical forest; temporal stability of coherence	Sites at Lopé, Mondah, Mabounie and Rabi, Gabon	July 2015 (SETHI) Feb. 2016 (F-SAR)	Tropical forest and savannah, AGB from 50 to 500 t/ha
Afriscat: Ground-based high temporal resolution measurements	Measurement of long-term temporal coherence and temporal variation of backscatter in tropical forest	Ankasa, Ghana	July 2015 - July 2016	Tropical forest, low topography, AGB from 100 to 300 t/ha
Borealscat: Ground-	Time series of	Remningstorp,	Dec. 2016,	Hemi-boreal

based high temporal resolution measurements (Ulander et al., 2018; Monteith and Ulander, 2018)	backscatter, tomography, coherence and environmental parameters in boreal forest.	southern Sweden	ongoing	forest, spruce-dominated stand, low topography, AGB = 250 t/ha
--	---	-----------------	---------	--

367

368 **5.1 Estimating AGB**

369 Some key findings from these campaigns are illustrated in Fig. 2, where the P-band HV backscatter
370 (given as γ^0 in dB) is plotted against the biomass of reference plots from a boreal site (Remningstorp,
371 Sweden) and two tropical sites (Paracou, French Guiana and La Selva, Costa Rica). The data are not
372 corrected for topographic or soil moisture effects, and the lines correspond to linear regression fits to
373 the log-log form of the data. The sensitivity of backscatter to biomass is clear across the whole range
374 of biomass covered, though with large dispersion in the boreal forest and the high biomass tropical
375 forest in French Guiana. Also clear is that, for a given biomass, the HV backscatter is considerably
376 larger in boreal than tropical forest. This corrects an error in Fig. 2 of Le Toan et al. (2011) where
377 mean backscatter differences between the boreal and tropical data were ascribed to calibration errors
378 and removed by shifting the data. The careful calibration of the datasets shown in Fig. 2 indicates that
379 the difference is real and that different physical and biological factors (such as forest structure) are at
380 play in the different forest types.



381

382 **Fig. 2.** P-band backscatter at HV polarisation (γ_{HV}^0) over tropical and boreal forests against the
 383 biomass of in situ reference plots. Data from Paracou, French Guiana, were acquired by the SETHI
 384 SAR system in 2011 (Dubois-Fernandez et al., 2012), those from La Selva, Costa Rica, in 2004 by the
 385 AIRSAR system (Antonarakis et al., 2011) and those from Remningstorp, Sweden, by the E-SAR
 386 system in 2007 (Sandberg et al., 2011).

387

388 The regression lines indicate that in natural units the HV backscatter is approximately related to
 389 biomass, W , by a power law relationship, i.e.

$$390 \quad \gamma_{HV}^0 = cW^p \quad (2)$$

391 where c and p are parameters. Analysis in Schlund et al. (2018) indicates such relationships are found
 392 for the full set of available P-band SAR datasets that are supported by adequate in situ data except
 393 where there is strong topography. Although the model coefficients (and their coefficients of
 394 determination) vary across datasets, they are not significantly different when similar AGB ranges are
 395 considered.

396 Despite this strong regularity in the relation between HV backscatter and biomass, exploiting it to
 397 estimate biomass faces a number of problems:

398 **a. Dispersion in the data.** For the boreal data in Fig. 2, major factors causing dispersion in the
399 backscatter values are slope and soil moisture variations. The Krycklan campaign over boreal
400 forest in Sweden (Table 2) clearly shows that topography severely affects the power law
401 relationship given by eq. (2) (Soja et al., 2013). This is particularly obvious in Krycklan because
402 in this region most of the highest biomass stands are located in sloping areas. As demonstrated in
403 Soja et al. (2013), however, adding terms involving the $\gamma_{HH}^0/\gamma_{VV}^0$ ratio and slope to the regression
404 significantly reduces the dispersion, at the expense of including two extra parameters. Note that
405 the HH/VV ratio was included because of its lower sensitivity to soil moisture, and that the
406 regression inferred from the Krycklan site in N. Sweden could be successfully transferred to
407 Remningstorp 720 km away in S. Sweden. The associated relative RMSEs in AGB using the
408 combined BioSAR-1 and -2 data were 27% (35 t/ha) or greater at Krycklan and 22% (40 t/ha) or
409 greater at Remningstorp. However, more recent unpublished analysis including the BIOSAR-3
410 data indicates that further coefficients are needed to achieve adequate accuracy. Another study for
411 Remningstorp (Sandberg et al., 2014) found that AGB change could be estimated more accurately
412 than AGB itself: analysis based on 2007 and 2010 data gave a RMSE of 20 t/ha in the estimated
413 biomass change, i.e. roughly half the RMSEs of the individual AGB estimates. The algorithm
414 used was based on finding areas of little or no change using the HH/VV ratio and applying
415 polarization-dependent correction factors to reduce the effect of moisture variation.

416 Unlike in Sweden, very little environmental change occurred during the TropiSAR campaign in
417 French Guiana, and the major effect affecting the relation given by eq. (2) was topography, which
418 greatly increased the dispersion. Methods to reduce this were based on rotating the spatial axes
419 and normalization to account for the variation in the volume and double bounce backscatter with
420 incidence angle (Villard and Le Toan, 2015). This allowed the sensitivity of the HV backscatter to
421 biomass to be recovered, and AGB could then be estimated from the polarimetric data with
422 relative RMSE < 20%. However, because the approach is based on regression and there was little
423 temporal change in conditions during the campaign, it contains no provision for dealing with large
424 seasonal variations in backscatter like those observed in the Tropiscat data (Bai et al., 2018) and
425 expected in BIOMASS data.

426 **b. Algorithm training.** Regression methods need training data, but in many parts of the world, and
427 especially in the tropics, there are very few high quality permanent in situ sampling plots, almost
428 all funded under science grants. Significant efforts are being made by ESA, in collaboration with
429 NASA, to work with and extend the existing in situ networks in order to establish a set of well-
430 documented reference sites that could be using for training and validation. Part of the challenge in
431 doing so is to ensure that the set of reference sites is large enough and representative enough to
432 capture the major variations in forest types and conditions.

433 **c. Physical explanation.** Despite its remarkable generality, as demonstrated in Schlund et al.
434 (2018), the physical basis of eq. (2) is not well-understood except in certain limiting cases (see
435 below). Hence it is essentially empirical and at present we cannot in general attach meaningful
436 physical properties to the fitting parameters or derive them from scattering models. In particular,
437 it has no clear links to well-known decompositions of polarimetric backscatter into physical
438 mechanisms (e.g. Freeman and Durden (1998); Cloude and Pottier (1996)). In addition, in boreal
439 forests this relation depends on both total AGB and tree number density, so that unambiguous
440 estimates of AGB require information on number density or use of height information combined
441 with height- biomass allometric relations (Smith-Jonforsen et al., 2007)

442 To get round these problems with the regression-based approaches, the current emphasis is on
443 estimating biomass using a model-based approach that brings together three key factors: the
444 capabilities of the BIOMASS system, the observed properties of the vertical distribution of forest
445 biomass and our knowledge about the physics of radar-canopy interactions as embodied in scattering
446 models.

447 Its starting point is a simplified scattering model that describes the backscattering coefficient in each
448 of the HH, HV and VV channels as an incoherent sum of volume, surface and double-bounce
449 scattering (Truong-Loi et al., 2015). The model involves 6 real parameters per polarization, which are
450 estimated using a combination of a scattering model and reference data. Biomass, soil roughness and
451 soil moisture are then treated as variables to be estimated from the data. Initial analysis found that this
452 model was too complex and the associated parameter estimation was too unstable for this to be a

453 viable approach for BIOMASS. However, a crucial technical development was to demonstrate that
 454 both tomographic and Pol-InSAR data can be used to cancel out the terms involving the ground
 455 (surface scatter and double bounce) and isolate the volume scattering term (Mariotti d'Alessandro et
 456 al., 2013; Mariotti d'Alessandro et al., 2018). In the Truong-Loi et al. (2015) formulation, this term
 457 can be written as

$$458 \quad \sigma_{pq}^v = A_{pq} W^{\alpha_{pq}} \cos \theta \left(1 - \exp \left(-\frac{B_{pq} W^{\beta_{pq}}}{\cos \theta} \right) \right) \quad (3)$$

459 where A_{pq} , B_{pq} , α_{pq} and β_{pq} are coefficients for polarization configuration pq, W is AGB, and θ is
 460 the local incidence angle. The coefficients α_{pq} and β_{pq} relate to forest structure, $B_{pq} > 0$ is an
 461 extinction coefficient and $A_{pq} > 0$ is a scaling factor.

462 Assuming that A_{pq} , B_{pq} , α_{pq} and β_{pq} are space-invariant at a certain scale, these parameters and
 463 AGB can be estimated simultaneously from the measured values of σ_{pq}^v in the three polarizations, pq
 464 = HH, HV and VV, using a non-linear optimization scheme (Soja et al., 2017, 2018). However, in
 465 model (3), the two biomass-dependent factors, $A_{pq} W^{\alpha_{pq}}$ and $1 - \exp \left(-\frac{B_{pq} W^{\beta_{pq}}}{\cos \theta} \right)$, both increase
 466 with increasing AGB for realistic parameters ($\alpha_{pq} > 0$ and $\beta_{pq} > 0$), so interactions between
 467 α_{pq} , B_{pq} and β_{pq} render the inversion difficult. This problem can be mitigated by using two special
 468 cases of the model, both of which lead to a power law expression as in eq. (2). For the low-attenuation
 469 case, i.e., $B_{pq} W^{\beta_{pq}} \ll 1$, eq. (3) can be simplified using a series expansion to:

$$470 \quad \sigma_{pq}^v = A' W^p \quad (4)$$

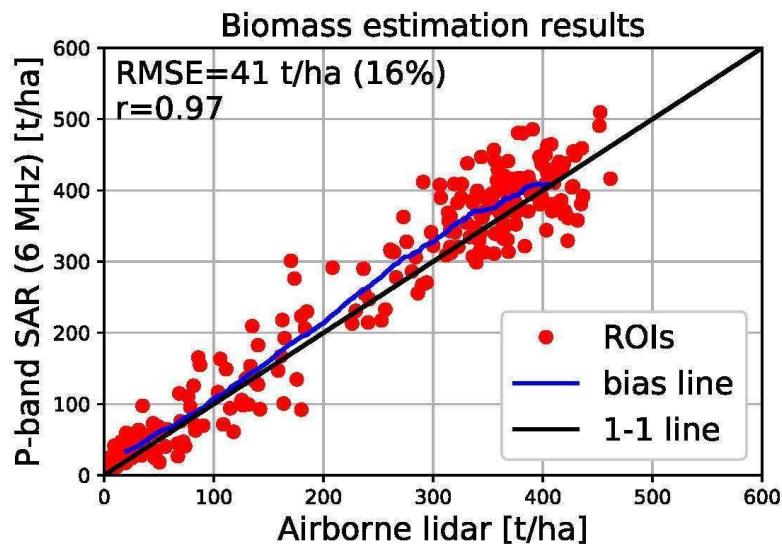
471 where $p = \alpha_{pq} + \beta_{pq}$ and $A' = A_{pq} B_{pq}$, and in the high-attenuation case, i.e., $B_{pq} W^{\beta_{pq}} \gg 1$, eq. (3)
 472 can be simplified to:

$$473 \quad \sigma_{pq}^v = A' W^p \cos \theta \quad (5)$$

474 where $p = \alpha_{pq}$ and $A' = A_{pq}$. In both cases, A' , W and p can then be estimated using the scheme
 475 proposed in Soja et al. (2017, 2018).

476 Note that there is still an inherent scaling ambiguity since the scheme cannot distinguish the unbiased
 477 estimate of AGB, W_0 , from any function of the form aW_0^b , where a and b are calibration constants.
 478 Hence reference data are needed, but these data do not need to cover a wide range of backscatter,
 479 slope and incidence angle conditions, as would be required if any of the models (3) - (5) were to be
 480 trained directly. One complication is that the temporal and spatial variations of a and b are are
 481 currently unknown and further work is needed to quantify them. Further refinements may also be
 482 needed to reduce residual effects from moisture variations by, for example, use of the VV/HH ratio in
 483 boreal forests as discussed above.

484 The effectiveness of this approach is illustrated by Fig. 3, which plots values of AGB estimated with
 485 this scheme against AGB values estimated from in situ and airborne laser scanning data for a set of
 486 200 m x 200 m regions of interest (ROIs). The airborne P-band data used are from the AfriSAR
 487 campaign and were filtered to 6 MHz to match the BIOMASS bandwidth. The estimates are highly
 488 correlated with the reference data ($r = 0.97$), exhibit only a small amount of bias across the whole
 489 biomass range, and give a RMSE of 41 t/ha (16% of the average biomass).

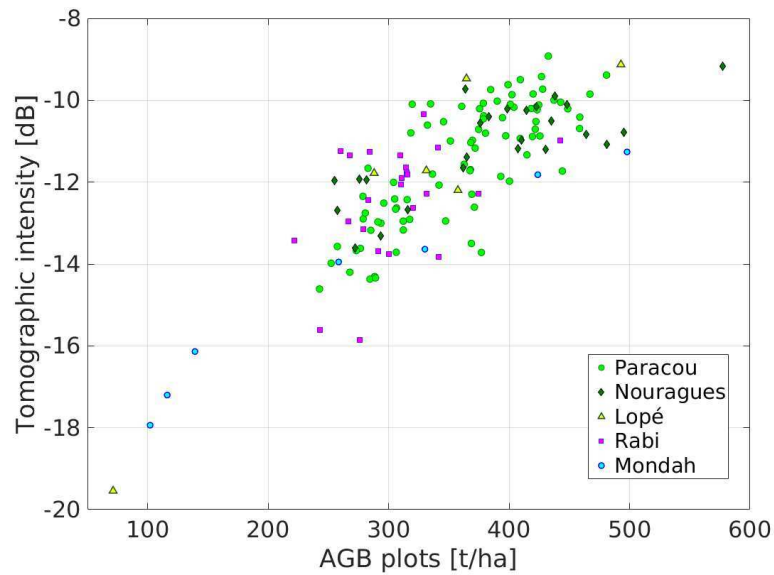


490
 491 **Fig. 3.** Estimated AGB using the approach described in the text against AGB estimated from in situ
 492 and airborne laser scanning at the La Lopé site in Gabon during the AfriSAR campaign. The running
 493 average given by the blue line indicates only a small positive bias across the whole range of AGB.
 494 ROI denotes Region of Interest.

495 Further confirmation of the importance of isolating the volume backscatter by using the full power of
496 tomography is from the TropiSAR tropical forest campaign, where the tomographic intensity (in dB)
497 measured at 30 m above the ground (representing scattering from canopy elements between ca. 17.5
498 m and 42.5 m, given the roughly 25 m vertical resolution of tomographic imaging) was found to be
499 highly correlated with AGB (Ho Tong Minh et al., 2014, 2016). The observed sensitivity is about 50
500 tons/ha per dB, and the correlation coefficient is about 0.84 at the scale of 1 ha. This striking result
501 has been replicated in the forest sites investigated during the AfriSAR campaign (Fig. 4), and suggests
502 that the backscatter from the forest layer centred 30 m above ground should be strongly correlated
503 with total AGB in the case of dense tropical forests.

504 Importantly, this finding is consistent with the TROLL ecological model (Chave, 1999), which
505 predicts that for dense tropical forests the fraction of biomass contained between 20 m and 40 m
506 accounts for about 35% to 40% of the total AGB, and that this relation is stable over a large range of
507 AGB values (Ho Tong Minh et al., 2014). Another element in support of the ecological relevance of
508 the 30 m layer is provided by two recent studies of tropical forests, which observed that: a) correlation
509 between AGB and the area occupied at different heights by large trees (as derived from lidar) is
510 maximal at a height of about 30 m (Meyer et al., 2017); b) about 35% of the total volume tends to be
511 concentrated at approximately 24-40 m above the ground (Tang, 2018).

512 However, tomographic data will only be available in the first phase of the mission. In addition,
513 exploiting the relation between AGB and the 30 m tomographic layer requires knowledge of how the
514 regression coefficients vary in time and space, hence substantial amounts of training data. In contrast,
515 ground cancellation can be carried out with both tomographic and Pol-InSAR data (so throughout the
516 mission). This allows the volume scattering term (eq. (3)) to be isolated and hence AGB to be
517 estimated using the scheme described in Soja et al. (2018), which makes much less demand on the
518 availability of reference data.



519

520 **Fig. 4.** Plot of HV backscatter intensity at height 30 m above the ground measured by tomography
 521 against in situ AGB in 1 ha plots at tropical forest sites investigated during the TropiSAR (Paracou
 522 and Nouragues) and AfriSAR (Lopé, Rabi, Mondah) campaigns.

523

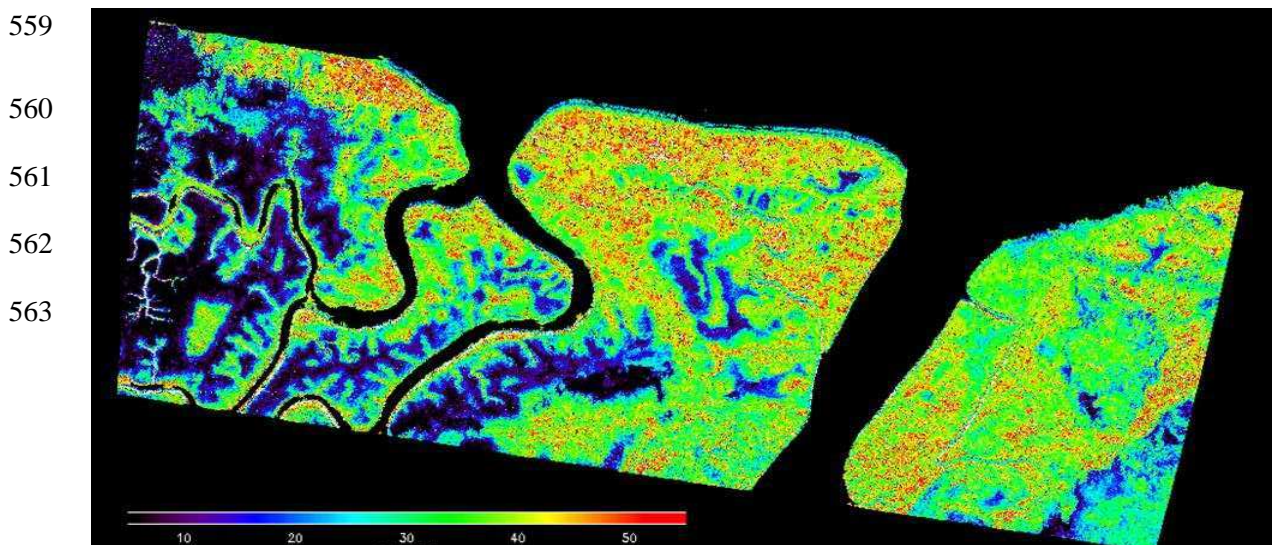
524 The value of tomography for estimating AGB in boreal and temperate forests is less clear, since (a)
 525 these forests in general have smaller heights than in the tropics (so it is more problematical to isolate
 526 the signal from a canopy layer without corruption by a ground contribution, given the roughly 25 m
 527 vertical resolution of the tomographic product from BIOMASS), and (b) the double bounce
 528 mechanism appears to be important in recovering the AGB of boreal forests. Hence ground
 529 cancellation (which also cancels double bounce scattering, since this appears at ground level in the
 530 tomographic image) may not help biomass estimation in such forests, and the preferred algorithm for
 531 BIOMASS in these cases is still not fixed. Recent results indicate that ground cancellation improves
 532 results in Krycklan, but not in Remningstorp, most likely because it suppresses direct ground
 533 backscattering, which is unrelated to AGB but is of higher relative importance in Krycklan due to the
 534 pronounced topography.

535

536 **5.2 Estimating forest height**

537 Forest height estimates will be available throughout the Tomographic and Interferometric Phases, in
538 the latter case using polarimetric interferometric (Pol-InSAR) techniques (Cloude and Papathanassiou,
539 1998, 2003; Papathanassiou and Cloude, 2001) applied to three polarimetric acquisitions performed in
540 a 3-day repeat-pass interferometric mode. The use of Pol-InSAR to estimate forest height has been
541 demonstrated at frequencies from X- to P-band for a variety of temperate, boreal and tropical sites,
542 with widely different stand and terrain conditions (Praks et al., 2007; Kugler et al., 2014; Hajnsek et
543 al., 2009; Garestier et al., 2008), and several dedicated studies have addressed its likely performance
544 and limitations when applied to BIOMASS data.

545 Estimation of forest height from Pol-InSAR requires a model that relates forest height to the Pol-
546 InSAR measurements (i.e. primarily to the interferometric coherence at different polarisations and for
547 different spatial baselines) together with a methodology to invert the established model. Most of the
548 established inversion algorithms use the two-layer Random Volume over Ground (RVoG) model to
549 relate forest height to interferometric coherence (Treuhaft et al., 1996). This relies on two
550 assumptions: 1) all polarizations “see” (up to a scalar scaling factor) the same vertical distribution of
551 scatterers in the vegetation (volume) layer; 2) the ground layer is impenetrable, i.e. for all
552 polarizations, the reflectivity of the ground scattering component is given by a Dirac delta function
553 modulated by a polarimetrically dependent amplitude. The RVoG model has been extensively
554 validated and its strong and weak points are well understood. Use of this model to obtain a forest
555 height map is illustrated in Fig. 5 which is derived by inverting P-band Pol-InSAR data acquired
556 during the AfriSAR campaign in February 2017 over the Pongara National Park, Gabon. This site is
557 covered mainly by mangrove forests, which are among the tallest mangrove forests in the world,
558 towering up to 60 m.



564
565
566
567
568
569
570
571
572
573
574
575
576
577
578
579
580
581
582
583
584
585
586
587
588
589
590

Fig. 5. Forest height map obtained from inverting P-band Pol-InSAR data acquired over the Pongara National Park, Gabon, in the framework of the AfriSAR campaign in February 2017.

The main challenge for BIOMASS is therefore the development of an inversion formulation able to provide unique, unbiased and robust height estimates, and which accounts for: 1) the scattering characteristics at P-band, since the limited attenuation by the forest canopy means that a ground scattering component is present in all polarisations; 2) the constraints imposed by the BIOMASS configuration, both the 6 MHz bandwidth and the fact that some temporal decorrelation is inevitable in the repeat-pass mode (Lee et al., 2013; Kugler et al., 2015). To meet this challenge a flexible multi-baseline inversion scheme has been developed that allows the inversion of the RVoG model by including: 1) a polarimetric three-dimensional ground scattering component; 2) a vertical distribution of volume scattering that can adapt to high (tropical) and low (boreal) attenuation scenarios; 3) a scalar temporal decorrelation that accounts for wind-induced temporal decorrelation of the vegetation layer. The inversion can then be performed using the three polarimetric acquisitions in the Interferometric Phase, allowing global forest height maps to be produced every 7 months.

The main limitations in generating the forest height product arise not from the inversion methodology but from the 6 MHz bandwidth, which constrains the generation of large baselines as well as the spatial resolution of the data, and the low frequency, which reduces the sensitivity to forest height in certain sparse forest conditions. On the other hand, the low frequency will provide high temporal stability over the 3-day repeat period of the Interferometric Phase, which is necessary to establish uniqueness and optimum conditioning of the inversion problem.

An alternative approach to estimating forest height is by tracing the upper envelope of the observed tomographic intensities, as reported in Tebaldini and Rocca (2012) and Ho Tong Minh et al. (2016) for boreal and tropical forests, respectively. This has the advantage of being less computationally

591 expensive than model-based inversion, and it can be applied in the absence of a specific model of the
592 forest vertical structure. Importantly, it has been demonstrated using synthetic 6 MHz data simulating
593 BIOMASS acquisitions over boreal forests (Tebaldini and Rocca, 2012). However, this approach will
594 only be possible during the Tomographic Phase of the mission.

595

596 **6. Severe forest disturbance**

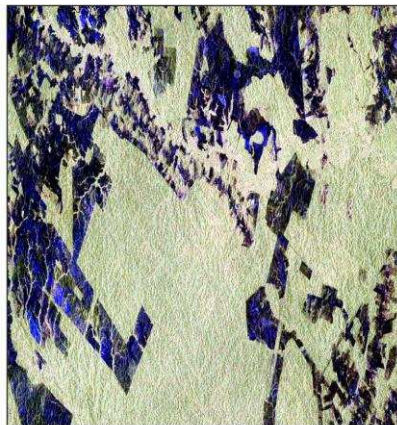
597 The BIOMASS disturbance product aims to detect high-intensity forest disturbance (effectively forest
598 clearance) occurring between satellite revisit times. This is a natural extra use of the data gathered for
599 biomass and height estimation, rather than a driver for the BIOMASS mission, and will contribute to
600 the overall capability to measure forest loss from space using optical (e.g., Hansen et al., 2013) and
601 radar sensors (e.g., the pair of Sentinel-1 C-band radar satellites). Changes in the polarimetric
602 covariance matrix caused by deforestation are relatively large; for example, Fig. 1 indicates that γ_{hv}^0
603 changes by 5 dB as biomass decreases from 500 t ha⁻¹ to nearly zero, while a change in AGB from
604 100 to 200 t ha⁻¹ causes γ_{hv}^0 to change by only ~1 dB. Hence change detection is less affected by the
605 statistical variability inherent in the radar signal, allowing the disturbance product to be produced at a
606 spatial resolution of ~50 m, instead of 200 m, as for the biomass and height products.

607 The method proposed for detecting disturbance is firmly rooted in the statistical properties of the 6-
608 look polarimetric covariance data and uses a likelihood ratio (Conradsen et al., 2016) to test, at a
609 given level of statistical significance, whether change has occurred relative to previous acquisitions in
610 each new polarimetric acquisition over forest. Note that this approach does not specify the detection
611 probability, which would require an explicit form of the multi-variate probability distribution function
612 associated with disturbed forest. This would be very difficult to characterise in any general sense
613 because change may affect the covariance matrix in many different ways. Instead it provides a
614 quantitative way to determine how sure we are that change has occurred; in this respect it is closely
615 related to the Constant False Alarm Rate approach to target detection (e.g. Scharf, 1991).

616 A current unknown in this approach is to what extent changes in the covariance matrix of undisturbed
617 forest caused by environmental effects, such as changing soil moisture due to rainfall events, will

618 increase the false detection rate. A further issue is that detections are only sought in forest pixels, so
619 an accurate initial forest map is required, preferably estimated from the radar data themselves but
620 possibly from some other source; this will be progressively updated after each new acquisition.
621 Some insight into the performance of this approach can be gained using multi-temporal polarimetric
622 data from PALSAR-2. Fig. 6 shows at the top Pauli format slant range representations of a pair of
623 images gathered on 8 August 2014 and 8 August 2015 (so in this case the time series has length 2),
624 below left the detection of change at 99% significance and below right the pixels at which change
625 occurred marked in red on the image from 2014 (with no forest mask applied). It can be seen that the
626 areas where change was detected occur in the non-forest regions, while detections in the forest regions
627 occur as isolated pixels consistent with the 1% false alarm rate implied by the level of significance of
628 the test.

140808



150807



Detection of Change: P>99%



140808 + Change (red mask)



629

630 **Fig. 6.** (Top) Pair of repeat-pass PALSAR-2 images acquired on 8 August 2014 and 7 August 2015
631 displayed in Pauli image format (red = HH + VV; blue = HH - VV; green = 2HV) and slant range
632 geometry. (Bottom left) Detection of change at 99% significance level; changed pixels are marked as
633 black. (Bottom right) Image from 8 August 2014 with changed pixels marked as red.

634 **7. In situ and lidar reference biomass data**

635 Although the model-based inversion proposed for estimating biomass (Section 5.1) minimises the
636 need for in situ reference data, such data are critical for algorithm development and testing,
637 investigation of regression-based approaches, and product calibration and validation. The BIOMASS
638 mission faces three major challenges in providing these supporting data: (i) the key region where
639 reference data are needed is the tropics, but high quality biomass data are available at only a very
640 limited number of tropical sites; (ii) biomass will be estimated at a scale of 4 ha (200 m by 200 m
641 pixels) but most plot data are available at scales of 1 ha or less and the geographical locations of the
642 plots is often not known to high accuracy; (iii) because of SOTR restrictions (Section 2), reference
643 sites in the temperate and boreal zones will need to be outside N America and Europe.

644 ESA are addressing challenge (i) and (ii) by working with existing networks to develop suitable
645 extensive in situ reference data before launch through the Forest Observation System ([http://forest-
646 observation-system.net/](http://forest-observation-system.net/)). A further encouraging development is the ESA-NASA initiative to
647 collaborate in developing the in situ data requirements for GEDI, BIOMASS and NISAR. Co-
648 operation along these lines is already in evidence from joint contributions to the AfriSAR campaign
649 by ESA and NASA. As regards (iii), for the temperate zone, southern hemisphere sites, e.g. in
650 Tasmania, would be suitable, while Siberia is the most desirable region for the boreal zone. However,
651 concrete plans to gather in situ data in these regions are not currently in place.

652 An important complement to in situ data that helps to address challenge (ii) is airborne lidar data. This
653 can provide a forest height map and information on canopy structure which, when combined with
654 field data, allows biomass to be estimated. Lidar data offer many advantages, including:

- 655 • A scanning lidar provides a relatively fine scale and accurate map of biomass, which can be
656 aggregated to the 4 ha resolution cell of BIOMASS (this will allow the effects of variability in

657 biomass at sub-resolution size to be assessed). Precision at this scale is typically below 10%
658 and the vast majority of relevant studies indicate that the associated pan-tropical allometry
659 (Chave et al. 2014) has negligible bias.

- 660 • Lidar mapping can cover landscapes with a wide range of biomass levels and different forest
661 conditions (degraded, regrowth, selectively logged, etc.).
- 662 • Forest height with fine resolution (around 1 m) can be estimated at the same time as biomass.

663 Hence the validation strategy for BIOMASS will involve a combination of in situ reference forest
664 plots and lidar-derived biomass/height maps.

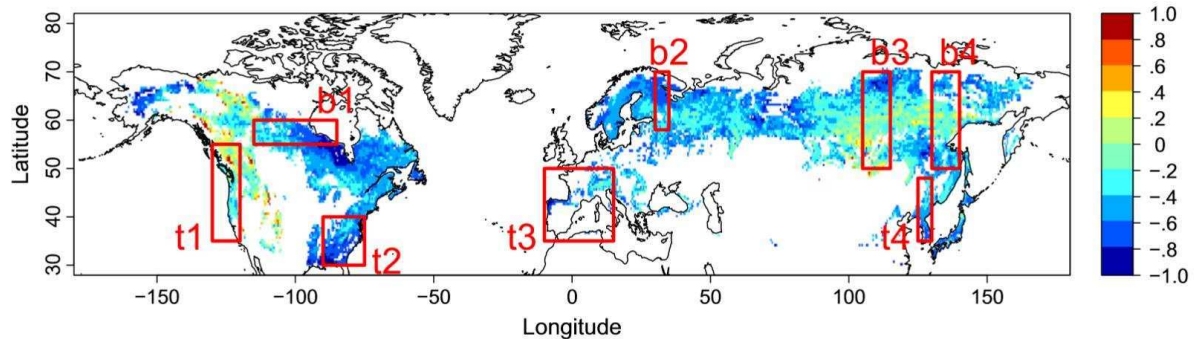
665 **8. Exploiting BIOMASS data in carbon cycle and climate analysis**

666 Although the primary objectives of BIOMASS are to reduce the major uncertainties in carbon fluxes
667 linked to Land Use Change, forest degradation and regrowth and to provide support for international
668 agreements (UNFCCC & REDD+), its products will also play a key role in advancing fundamental
669 knowledge of forest ecology and biogeochemistry. For example, BIOMASS data will help in
670 constraining critical carbon cycle parameters, initialising and testing the land component of carbon
671 cycle and Earth System models (ESMs), and quantifying the forest disturbance regime.

672 Differences between ESM forecasts of the carbon cycle are currently significant, and lead to major
673 uncertainties in predictions (Exbrayat et al., 2018). These differences have been linked to variations in
674 the internal processing of carbon, particularly in the large pools in biomass and soil organic matter
675 (Friend et al. 2014). Linking biomass mapping to estimates of net primary production (NPP) provides
676 a constraint on the turnover rate of the biomass pool, a critical model diagnostic (Carvalhais et al.,
677 2014; Thurner et al., 2014). A recent study (Thurner et al., 2017) found observed boreal and temperate
678 forest carbon turnover rates up to 80% greater than estimates from global vegetation models involved
679 in the Inter-Sectoral Impact Model Intercomparison Project (ISI-MIP) (Warszawski et al., 2014). The
680 relative difference between modelled and observed values is shown in Fig. 7, where the red boxes
681 indicate regions analysed in Thurner et al. (2017) in order to explain these discrepancies. In the boreal
682 zone (boxes b1 - 4) they were mainly attributed to the neglect of the effects of frost damage on

683 mortality in the models, while most of the models did not reproduce observation-based relationships
684 between mortality and drought in temperate forest transects (boxes t1 - 3).

685



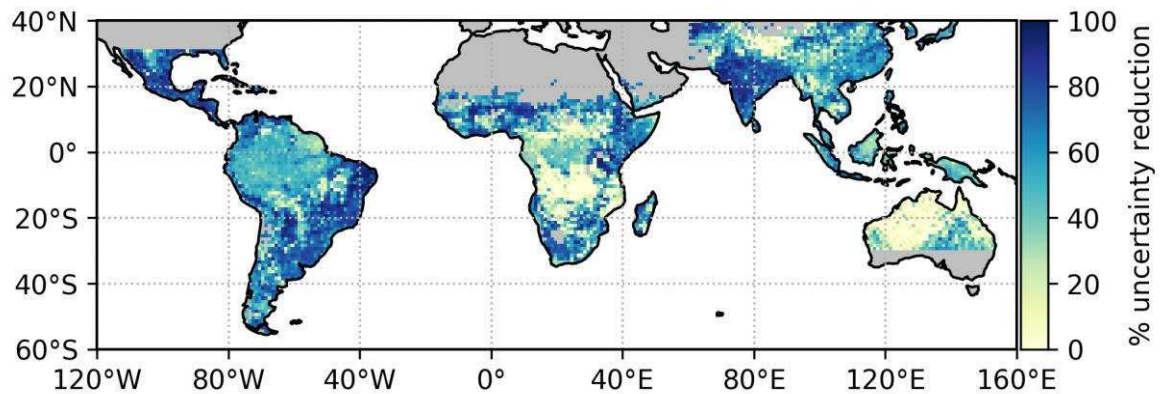
686

687 **Fig 7.** Relative difference between modelled carbon turnover rates and turnover rates inferred from
688 observations. 1.0 means modelled rate is 100% higher (from Thurner et al., 2017). Red boxes labelled
689 b (boreal) and t (temperate) were analysed further in Thurner et al. (2017) to explain these
690 discrepancies (figure reproduced courtesy of Martin Thurner).

691 The more accurate estimates from BIOMASS, particularly over the tropical belt, will greatly improve
692 estimation of turnover across the tropics (Bloom et al., 2016). This information will support improved
693 parameterisation of carbon cycling for ESMs, allowing identification of regional variations in carbon
694 turnover currently missing from tropical plant functional types (Exbrayat et al., 2018a). A sensitivity
695 analysis performed using the CARDAMOM system (Bloom et al., 2016; Exbrayat et al. 2018b)
696 indicates an average reduction of $49.5 \pm 29.2\%$ (mean \pm 2 std) in the 95% confidence interval of the
697 estimated vegetation carbon turnover time when the recent pan-tropical biomass map due to Avitabile
698 et al. (2016) is assimilated. The analysis shows how this error reduction has clear spatial variability
699 with latitude and between continents (Fig. 8).

700 Another component of uncertainty in ESMs is in their initialisation of biomass stocks, arising from
701 the paucity of data in the tropics, Land Use Change and internal model steady states. Data from
702 BIOMASS will provide the modelling community with a compelling resource with which to
703 understand both steady state and transient forest carbon dynamics. Observations of the disturbance
704 regime will constrain modelling of both natural processes of disturbance and mortality and the role of

705 humans (Williams et al., 2013). The potential for BIOMASS to monitor degradation (partial loss of
706 biomass) will be critical for modelling the subtle and slow processes of carbon loss associated with
707 forest edges, fires and human communities (Ryan et al, 2012; Brinck et al., 2017).



708

709 **Fig. 8.** The relative reduction in the size of the 95% confidence interval of estimated vegetation
710 carbon turnover times when using a prior value for biomass at each pixel compared to a run without a
711 biomass prior. Turnover times were estimated using the CARDAMOM system. The darker areas
712 show where reduction in relative uncertainty is largest.

713 Repeated measurements of biomass will allow significant improvements in global monitoring of
714 forest dynamics, and analysis of associated carbon cycling at fine spatial scales. Current biomass
715 maps (e.g., Saatchi et al., 2011) provide maps of stocks at a fixed time (or combine observations from
716 several times). While such data help to constrain the steady state biomass, relevant at regional scales
717 ($\sim 1^\circ$), they give little information on the dynamics of forests at finer (ha to km^2) scales over time.
718 BIOMASS will allow detailed, localised, and temporally resolved analyses of forest dynamics to be
719 constrained. The value of such detailed information has been illustrated in a site level analysis for an
720 aggrading forest in North Carolina (Smallman et al., 2017). Using in situ carbon stock information as
721 a baseline, the analysis showed that a model analysis constrained purely by assimilation of 9
722 sequential annual biomass estimates (corresponding to the BIOMASS scenario, with 1 estimate in the
723 Tomographic Phase and 8 in the Interferometric Phase) together with time series of Leaf Area Index
724 (LAI, e.g. from an operational satellite like Sentinel-2) led to significantly smaller bias and narrower
725 confidence intervals in biomass increment estimates than when LAI and just one biomass estimate, or

726 only management information, were assimilated. Bias in estimated carbon use efficiency (the ratio of
727 NPP to gross primary production) was also significantly reduced by repeated biomass observations.
728 This indicates the potential of BIOMASS to improve significantly our knowledge of the internal
729 processing of carbon in forests.

730 **9. Secondary objectives**

731 BIOMASS will be the first P-band SAR in space and thus will offer previously unavailable
732 opportunities for measuring properties of the Earth. As a result, mission planning includes provision
733 for several secondary objectives, including mapping sub-surface geology, measuring terrain
734 topography under dense vegetation, estimating glacier and ice sheet velocities and investigating
735 properties of the ionosphere.

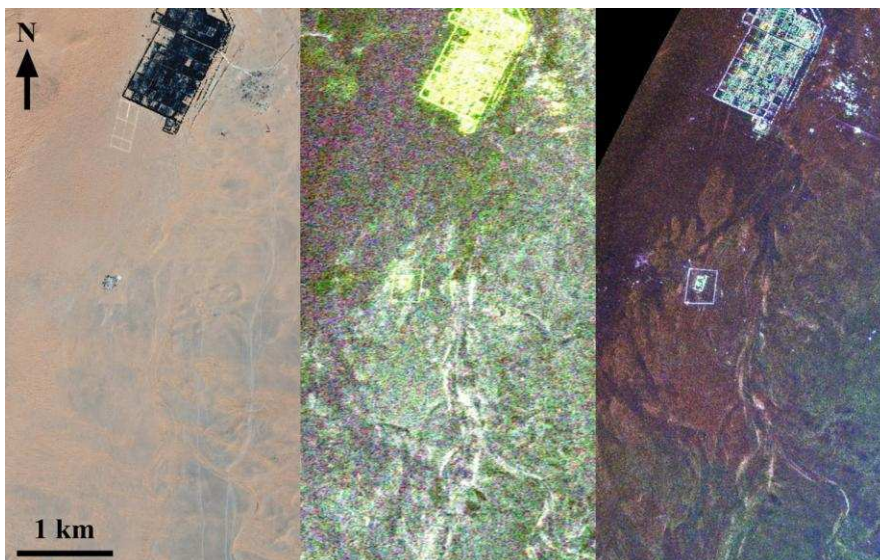
736 **9.1 Sub-surface geology**

737 In very dry environments, long wavelength SAR is able to probe the sub-surface down to several
738 metres, as was demonstrated at L-band (1.25 GHz) during the first Shuttle Imaging Radar SIR-A
739 mission (Elachi et al., 1984), which revealed buried and previously unknown palaeo-drainage
740 channels in southern Egypt (McCauley et al., 1982; Paillou et al., 2003). More complete L-band
741 coverage of the eastern Sahara acquired by the JAXA JERS-1 satellite was used to produce the first
742 regional-scale radar mosaic covering Egypt, northern Sudan, eastern Libya and northern Chad, from
743 which numerous unknown crater structures were identified (Paillou et al., 2006). In 2006, JAXA
744 launched the Advanced Land Observing Satellite (ALOS-1), carrying a fully polarimetric L-band SAR,
745 PALSAR, which offered higher resolution and much better signal to noise ratio than JERS-1. This
746 provided an unprecedented opportunity to study the palaeo-environment and palaeo-climate of
747 terrestrial deserts (Paillou et al., 2010), and led to the discovery of two major palaeo-rivers in North
748 Africa: the Kufrah river, a 900 km long palaeo-drainage system, which in the past connected
749 southeastern Libya to the Gulf of Sirt (Paillou et al., 2009; Paillou et al., 2012), and the Tamanrasset
750 River in Mauritania, which connected a vast ancient river system in the western Sahara to a large
751 submarine channel system, the Cap Timiris Canyon (Skonieczny et al., 2015). Besides its value in
752 studying the past climates of desert regions, the sub-surface imaging capability of L-band SAR also

753 helps to build more complete and accurate geological maps in support of future water prospecting in
754 arid and semi-arid regions (Paillou, 2017).
755
756 Deeper probing of the sub-surface requires longer radar wavelengths: while L-band can penetrate 1-2
757 m into dry sand, a P-band system should be able to probe down to more than 5 m. In June 2010, the
758 first ever airborne P-band SAR campaign over the Sahara was conducted at a desert site in southern
759 Tunisia using the SETHI system developed by ONERA (Paillou et al., 2011). Figure 9 shows a
760 comparison between an ALOS-2 L-band scene and a P-band scene acquired by SETHI over the Ksar
761 Ghilane oasis, an arid area at the border between past alluvial plains and present day sand dunes.. The
762 P-band data better reveal the sub-surface features under the superficial sand layer because of the higher
763 penetration depth and lower sensitivity to the covering sand surface. A two-layer scattering model for
764 the surface and sub-surface geometry is able to reproduce both the L- and P-band measured backscatter
765 levels, and indicates that the backscatter from the sub-surface layer is about 30 times weaker than from
766 the surface at L-band, while at P-band the sub-surface contribution is about 30 times stronger than that
767 from the surface. As a result, the total backscatter is comparable at P- and L-band, as the data show, but
768 the P-band return is dominated by the sub-surface layer (Paillou et al., 2017). Hence BIOMASS should
769 be a very effective tool for mapping sub-surface geological and hydrological features in arid areas,
770 offering a unique opportunity to reveal the hidden and still unknown history of deserts.

771

772



780
781
782
783
784
785
786
787
788
789
790
791
792
793
794
795
796
797
798
799
800
801
802
803
804
805
806

Figure 9. Left: SPOT image of the Ksar Ghilane oasis region in southern Tunisia: palaeo-channels are hidden by aeolian sand deposits. Middle: ALOS-2 L-band radar image, showing sub-surface features but blurred by the return from the superficial sand layer. Right: SETHI P-band radar image, clearly revealing sub-surface hydrological features.

9.2 Terrain topography under dense vegetation

As an integral part of its ability to make height-resolved measurements of the backscatter in forest canopies, the tomographic phase of the mission will gain access to the ground phase, and hence will be able to derive a true Digital Terrain Model (DTM) that is unaffected by forest cover (Mariotti d’Alessandro and Tebaldini, 2018) and expected to have a spatial resolution of ca. 100 m x 100 m. This contrasts with the Digital Elevation Models (DEMs) produced by radar sensors at higher frequencies, such as SRTM (Rodriguez et al., 2015) or Tandem-X (Wessel et al., 2018), in which attenuation and scattering by dense forest canopies cause biases. Since global tomographic acquisitions occupy the first phase of the mission, this improved DTM will be available early in the Interferometric Phase, and will be used to improve the products based on Pol-InSAR and PolSAR.

9.3 Glacier and ice sheet velocities

The velocity fields of glaciers and icesheets can be measured using two classes of SAR techniques: differential SAR Interferometry (DInSAR) (Massonnet et al., 1993) and offset tracking (Gray et al., 1998; Michel & Rignot, 1999). These techniques measure the ice displacement between two observations and require features in the ice or coherence between the observations. BIOMASS has the potential to supplement ice velocity measurements from other SAR missions, since its left-looking geometry with an inclination angle larger than 90° means that the polar gap in Antarctica will be smaller than for most other SAR missions, which are right-looking. The polar gap will be larger in Greenland, but the Greenland ice sheet cannot be mapped due to SOTR restrictions. The primary

807 advantage of BIOMASS is the higher coherence and longer coherence time resulting from the lower
808 frequency of BIOMASS compared to all other space-based SAR systems. Its longer wavelength with
809 deeper penetration into the firm ensures less sensitivity to snowfall, surface melt and aeolian processes
810 (Rignot, 2008). This is seen when comparing L-band and C-band results (Rignot, 2008; Boncori et al.,
811 2010), and explains the long coherence time observed in airborne P-band data acquired by the Danish
812 Technical University POLARIS SAR in the percolation zone of the Greenland ice sheet (Dall et al.
813 2013).

814 The range and azimuth components of the ice velocity field will most likely be measured with
815 differential SAR interferometry (DInSAR) and offset tracking, respectively. At lower latitudes two
816 velocity components might instead be obtained by combining DInSAR from ascending and
817 descending orbits, since the range resolution of BIOMASS is too coarse for offset tracking to provide
818 the range component (Dall et al. 2013). Generally DInSAR ensures less noisy results, and phase
819 unwrapping is facilitated by the fact that the fringe rate of BIOMASS DInSAR data will be 1/12 of
820 that of Sentinel-1 data, assuming a 6-day baseline in both cases. The very low ice velocities in the
821 interior of Antarctica call for a long temporal baseline, but a 70-day baseline has been successfully
822 used at C-band (Kwok et al., 2000), and therefore sufficiently high P-band coherence is not unlikely
823 with the 228-day baseline provided by the BIOMASS observation cycle. However, ionospheric
824 scintillation is severe at high latitudes, and without accurate correction will corrupt the ice velocity
825 maps, possibly prohibitively. Assessment of whether proposed correction techniques (Kim et al.,
826 2015; Li et al., 2015) are sufficiently accurate will only be possible when BIOMASS is in orbit.

827 **9.4 Ionospheric properties**

828 A major concern in initial studies for BIOMASS was the effect of the ionosphere on the radar signal,
829 and a crucial factor in the selection of the mission was demonstration that these effects could be
830 compensated or were negligible in the context of the mission primary objectives (Rogers et al., 2013;
831 Rogers and Quegan, 2014). However, correction of ionospheric effects (particularly Faraday rotation,
832 but also scintillation, as noted in Section 9.3) necessarily involves measuring them, which then
833 provides information on the ionosphere. The dawn-dusk BIOMASS orbit will cover major features of

834 the ionosphere, including the fairly quiescent ionosphere at low and mid-latitudes, steep gradients
835 around the dusk-side mid-latitude trough, and large irregularities in the auroral ovals and polar cap.
836 Measurements of ionospheric Total Electron Content, derived from Faraday rotation (Wright et al.,
837 2003) and/or interferometric measurements (Tebaldini et al., 2018), should be possible along the orbit
838 at spatial resolutions of around a km, giving an unprecedented capability to measure these spatial
839 structures and their changes, since they will be viewed every two hours as the orbit repeats.

840

841 **10. The role of BIOMASS in an overall observing system**

842 BIOMASS will have unique capabilities to map biomass in dense forests, but will form only part of
843 the overall system of sensors providing information on forest biomass and biomass change, and more
844 generally on the global carbon cycle. In fact, the next few years will see an unprecedented
845 combination of sensors either dedicated to or capable of measuring forest structure and biomass.
846 Particularly important for their links to BIOMASS will be the Global Ecosystem Dynamics
847 Investigation (GEDI) and NISAR missions.

848 GEDI will be a near infrared (1064 nm wavelength) light detection and ranging (lidar) sensor onboard
849 the International Space Station with a 2-year lifetime from deployment in late 2018. It is focusing on
850 tropical and temperate forests to address three key issues: 1) quantifying the above-ground carbon
851 balance of the land surface; 2) clarifying the role played by the land surface in mitigating atmospheric
852 CO₂ in the coming decades; 3) investigating how ecosystem structure affects habitat quality and
853 biodiversity. GEDI will provide the first sampling of forest vertical structure across all forests
854 between 51.5° S and 51.5° N, from which estimates of canopy height, ground elevation and vertical
855 canopy profile measurements will be derived. Further processing of the ~0.0625 ha footprint
856 measurements will then yield estimates of the mean and variance of AGB on a 1 km grid.

857 NISAR (launch 2021) is a joint project between NASA and ISRO (the Indian Space Research
858 Organization) to develop and launch the first dual-frequency SAR satellite, with NASA providing the
859 L-band (24 cm wavelength) and ISRO the S-band (12 cm wavelength) sensors. It will measure AGB
860 and its disturbance and regrowth globally in 1 ha grid-cells for areas where AGB does not exceed 100

861 t/ha, and aims to achieve an accuracy of 20 t/ha or better over at least 80% of these areas. Its focus is
862 therefore on lower biomass forests, which constitute a significant portion of boreal and temperate
863 forests and savanna woodlands. NISAR will give unprecedented L-band coverage in space and time,
864 being able to provide HH and HV observations every 12 days in ascending and descending orbits and
865 covering forests globally every 6 days. The mission is also designed to give global interferometric
866 SAR measurements for surface deformation and cryosphere monitoring.

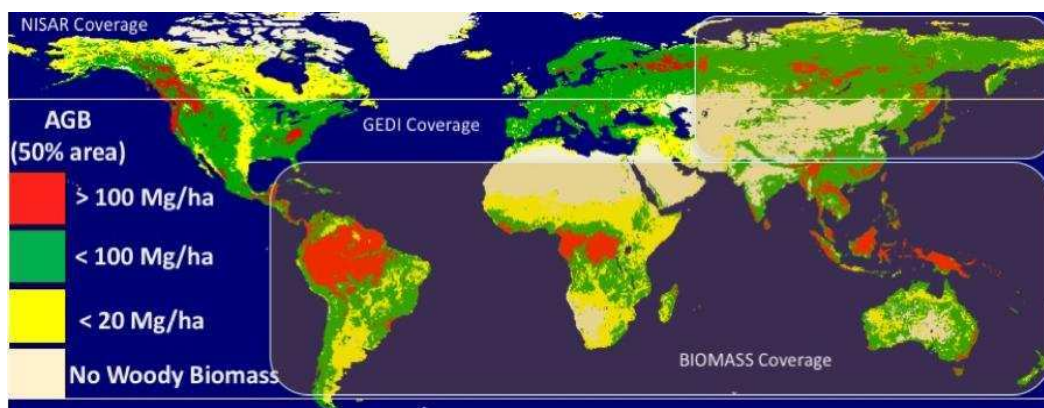
867 These three missions have significant overlaps in science objectives and products, but focus on
868 different observations, cover different regions, and retrieve different components of AGB at different
869 spatial and temporal scales. Their complementary nature is brought out by Fig. 10, which shows the
870 coverage of the three sensors on a map indicating approximate mean AGB. BIOMASS will focus on
871 tropical and sub-tropical woodlands at 4 ha resolution (though will also cover the temperate and
872 boreal forests of Asia and the southern hemisphere), NISAR will give global coverage at 1 ha
873 resolution but with AGB estimates limited to areas where $AGB < 100$ t/ha, and GEDI will cover the
874 full range of AGB, but with sample footprints limited to lie within $\pm 51.5^\circ$ latitude. Hence without the
875 data from all three missions, wall-to-wall estimation of global forest biomass will not be possible.
876 There will, however, still be lack of temporal and/or spatial coverage in regions where BIOMASS
877 cannot operate because of SOTR exclusions and where AGB exceeds the 100 t/ha threshold for
878 NISAR.

879 For lower values of AGB (less than about 50 t/ha) P-band measurements will be much more affected
880 by soil conditions than L-band, and NISAR should provide more accurate AGB estimates. The high
881 temporal frequency of NISAR observations will also allow the effects of soil moisture changes and
882 vegetation phenology to be mitigated. Currently the theoretical basis of the algorithms proposed for
883 NISAR and BIOMASS are the same (Truong-Loi et al., 2015), which offers the possibility of a
884 combined L- and P-band algorithm that optimises the capabilities of each. In addition, GEDI forest
885 height and biomass products will be available before the NISAR and BIOMASS missions, so can help
886 to initialize their algorithms and validate their products. GEDI estimates of the vertical structure of
887 forests will also be of enormous value in interpreting the BIOMASS Pol-InSAR and tomographic

888 measurements and in producing a consistent forest height and digital terrain model at fine spatial scale
889 (around 1 ha). Conversely, height or backscatter products from NISAR and BIOMASS missions can
890 provide information on the spatial variability of forest structure and biomass; this may be used in
891 future reprocessing to improve both the algorithms that form the GEDI gridded height and biomass
892 products and the resolution of these products.

893 Hence the three sensors will be highly complementary, and their combination will provide an
894 unparalleled opportunity to estimate forest AGB, height and structure globally with unprecedented
895 accuracy, spatial resolution and temporal and spatial coverage.

896



903

904 **Fig. 10.** Coverage of ESA and NASA-ISRO satellite measurements of forest structure and above-ground
905 biomass (AGB). The background shows the global coverage area of NISAR, which will be sensitive to AGB
906 values < 100 t/ha (green and yellow). BIOMASS coverage includes the tropical belt, the temperate and boreal
907 zones of Asia, and the southern hemisphere, while the GEDI Lidar will sample latitudes between $\pm 51.5^\circ$. These
908 two sensors will cover the full range of forest AGB providing measurements where AGB >100 t/ha (red), so
909 inaccessible to NISAR.

910

911 Discussion

912 Along with its role in quantifying the biomass and its change, it is important to realize that the
913 BIOMASS instrument, particularly in its interferometric and tomographic modes, is capable of
914 producing global measures of important forest properties that are simply unavailable for almost all of

915 the Earth. Some of these are practical measurements whose value has been known for years. For
916 example, in forestry the ability to predict yield or increase in biomass is increased greatly when one
917 knows both mass and height, so much so that tree height has been used in yield-table-based forestry to
918 quantify the so-called site-index, the quality of a site for forest enterprise. Hence the information from
919 the BIOMASS satellite and the modern digital offspring of classic forestry yield tables could be used
920 to make informed estimates of expected net production of forest biomass. In similar vein, Section 8
921 notes how the combination of biomass with NPP allows the turnover time of carbon within forest
922 vegetation to be estimated. Both examples illustrate that although forest biomass, height, structure and
923 change are all individually important, their full significance for climate, carbon cycle, biodiversity,
924 resource management, etc., is only fully realised when they are combined with each other and with
925 other sources of information.

926 This perception of biomass as a key variable within a wider information system is implicit in the
927 recognition of AGB as an ECV (GCOS, 2017). More explicit analysis of its function within a carbon
928 information and management system is provided by the Group on Earth Observations (GEO) (Ciais et
929 al., 2010) and the response to this report in the CEOS Strategy for Carbon Observations from Space
930 (CEOS, 2014). In particular, the CEOS report (Fig. 2.3 and Table 2.1 of the report) indicates where
931 biomass fits within the set of key GEO satellite requirement areas and core GEO observational
932 elements necessary to quantify the current state and dynamics of the terrestrial carbon cycle and its
933 components. Central to the GEO Carbon Strategy is the combination of data and carbon cycle models,
934 not least because models provide the only way in which the many available space-based and in situ
935 measurements can be integrated into a single consistent structure for performing carbon flux
936 calculations.

937 There are many possible forms for these models but data can interact with them in essentially four
938 ways: by providing estimates of current model state variables, estimates of model parameters, tracking
939 of processes and testing of model predictions. In addition, data and models can be even more tightly
940 bound by combining them in a data assimilation structure where both are regarded as sources of
941 information whose relative contribution to carbon flux estimates is weighted by their uncertainty.

942 There are already significant developments in exploiting biomass data in these ways, for example
943 initializing the age structure of forests when estimating the European carbon balance (Bellassen et al.,
944 2011), estimating carbon turnover time (Turner et al., 2017), testing Dynamic Global Vegetation
945 Models (Cantú et al., 2018), and full-scale data assimilation (Bloom et al., 2016). Further progress in
946 this direction is to be expected as we move towards launch in 2022.

947 **Conclusions**

948 BIOMASS mission will be the first space-based P-band radar, and this completely new view from
949 space will yield both predictable and unforeseen opportunities to learn about the Earth and its
950 dynamics. Within the operational constraints imposed by the Space Object Tracking Radar system
951 (Section 2) the 5-year mission will provide global mapping of forest AGB, height and change at 200
952 m spatial resolution by combining three different radar techniques, each of them innovative. This is
953 the first space-based radar mission for which all observations will be fully polarimetric, which is
954 necessary both to recover biomass information and to correct ionospheric effects. Even more
955 innovative will be this first systematic use of Pol-InSAR to measure forest height globally, and the
956 first use of SAR tomography to identify the vertical structure of forests globally. In parallel with these
957 major technological developments, considerable progress is being made in developing new
958 understanding and quantitative methods that will allow these measurements to be exploited in carbon
959 cycle and climate models. This link between measurements and models forms an essential part of
960 meeting the primary objective of the BIOMASS mission, which is to determine the worldwide
961 distribution of forest AGB in order to reduce the major uncertainties in calculations of carbon stocks
962 and fluxes associated with the terrestrial biosphere, including carbon fluxes associated with Land Use
963 Change, forest degradation and forest regrowth. Of major mutual advantage in meeting this objective
964 will be the information provided by other space missions flying within the next five years, for which
965 pride of place goes to GEDI and NISAR, but supplemented by optical and other radar missions. Of
966 great importance is that the structures for making use of these new data in carbon cycle and climate
967 models are being developed and implemented.

968 The physical and technical capabilities embedded in the BIOMASS mission in order to measure
969 biomass can be turned to many other uses. At present, known applications include sub-surface
970 imaging in arid regions, estimating glacier and icesheet velocities, and production of a true DTM
971 without biases caused by forest cover. An originally unforeseen application arising from the need to
972 correct the radar signal for ionospheric effects is to exploit the high sensitivity of the P-band signal to
973 Total Electron Content to estimate ionospheric properties and changes along the satellite's dawn-dusk
974 orbit. This is likely to be just one amongst many novel uses of the BIOMASS data, whose scope will
975 only become clear once BIOMASS is in orbit.

976 **Acknowledgements**

977 This work was in part supported by the UK National Environment Research Council National Centre
978 for Earth Observation (NCEO).

979

980 **References**

981

982 Antonarakis, A.S., Saatchi, S.S., Chazdon, R.L. & Moorcroft, P.R. (2011). Using Lidar and radar
983 measurements to constrain predictions of forest ecosystem structure and function. *Ecological*
984 *Applications*, 21(4), 1120–1137.

985 Askne, J. I. H., Soja, M. J., and Ulander, L. M. H. (2017). Biomass estimation in a boreal forest from
986 TanDEM-X data, lidar DTM, and the interferometric water cloud model, *Remote Sensing of Env.*,
987 196, 265-278, doi:org/10.1016/j.rse.2017.05.010.

988 Avitabile, V., Herold, M., Heuvelink, G. B. M., Lewis, S. L., Phillips, O. L., Asner, G. P., et al.
989 (2016). An integrated pan-tropical biomass map using multiple reference datasets, *Glob. Change Biol.*
990 22(4), 1406-1420, doi: 10.1111/gcb.13139.

991 Baccini, A., Goetz, S. J., Walker, W. S., Laporte, N. T., Sun M., Sulla-Menashe, D., et al. (2012).
992 Estimated carbon dioxide emissions from tropical deforestation improved by carbon-density maps.
993 *Nature Clim. Change*, 2, 182-185, doi:110.1038/nclimate1354.

994 Baccini, A., Walker, W., Carvalho, L., Farina, M., Sulla-Menashe, D., Houghton, R. A. (2017).
995 Tropical forests are a net carbon source based on aboveground measurements of gain and loss,
996 Science, 358(6360), 230-234, doi:10.1126/science.aam5962.

997 Bai, Y., Tebaldini, S., Ho Tong Minh, D., and Yang, W. (2018). An empirical study on the impact of
998 changing weather conditions on repeat-pass SAR tomography,” IEEE Jnl. Selected Topics in Applied
999 Earth Observations and Remote Sensing, 1–7.

1000 Bellassen, V., Viovy, N., Luyssaert, S., Le Maire, G., Schelhaas, M.-J. and Ciais, P. (2011).
1001 Reconstruction and attribution of the carbon sink of European forests between 1950 and 2000, Global
1002 Change Biology, 17, 3274–3292, doi: 10.1111/j.1365-2486.2011.02476.x.

1003 Bloom AA, Exbrayat J-F, van der Velde I.R., Feng L, Williams, M. (2016). The decadal state of the
1004 terrestrial carbon cycle: Global retrievals of terrestrial carbon allocation, pools, and residence times,
1005 PNAS, 113(5), 1285-1290, [doi:pnas.1515160113](https://doi.org/10.1073/pnas.1515160113).

1006 Boncori, J.P.M., Dall, J., Ahlstrøm, A.P., Andersen, S.B. (2010). Validation and operational
1007 measurements with SUSIE: a SAR ice motion processing chain developed within PROMICE
1008 (Programme for Monitoring of Greenland Ice-Sheet), Proc. ESA Living Planet Symposium, Bergen.

1009 Bouvet, A., Mermoz, S., Le Toan, T., Villard, L., Mathieu, R., Naidoo, L., and Asner, G. P. (2018).
1010 An above-ground biomass map of African savannahs and woodlands at 25 m resolution derived from
1011 ALOS PALSAR, Remote Sens. Env., 206, 156–173.

1012 Brinck, K., Fischer, R., Groeneveld, J., Lehmann, S., De Paula, M.D., et al. (2017). High resolution
1013 analysis of tropical forest fragmentation and its impact on the global carbon cycle. Nature
1014 Communications, 8, 14855

1015 Cairns, M.A., Brown, S., Helmer, E.H., & Baumgardner, G.A. (1997). Root biomass allocation in the
1016 world’s upland forests. Oecologia, 111, 1–11.

1017 Cantú, A. G., Friele, K., Reye, C. P.O., Ciais, P., Chang, J., Ito, A., et al. (2018). Evaluating changes
1018 of biomass in global vegetation models: the role of turnover fluctuations and ENSO events, Environ.
1019 Res. Lett., 13, 075002.

1020 Carreiras, J. M. B., Quegan, S., Le Toan, T., Ho Tong Minh, D., Saatchi, S., Carvalhais, N., et al.
1021 (2017). Coverage of high biomass forests by the ESA BIOMASS mission under defense restrictions,
1022 Remote Sensing of Environment, 196, 154-162, doi.org/10.1016/j.rse.2017.05.003.

1023 Carvalhais N, Forkel M, Khomik M, Bellarby J, Jung M, Migliavacca M, et al. (2014). Global
1024 covariation of carbon turnover times with climate in terrestrial ecosystems. Nature, 514, 213-217.

1025 CEOS (2014). CEOS Strategy for Carbon Observations from Space; The Committee on Earth
1026 Observation Satellites (CEOS) Response to the Group on Earth Observations (GEO) Carbon
1027 Strategy.

1028 Chave, J. (1999). Study of structural, successional and spatial patterns in tropical rain forests using
1029 TROLL, a spatially explicit forest model, Ecological Modelling, 124 (2–3), 233–254.

1030 Chave, J., Rejou-Mechain, M. , Burquez, A., Chidumayo, E., Colgan, M. S., Delitti, W. B., et al.
1031 (2014). Improved allometric models to estimate the aboveground biomass of tropical trees, Global
1032 Change Biology, 20, 3177–3190, doi: 10.1111/gcb.12629.

1033 Ciais, P., Dolman, A. J., Dargaville, R., Barrie, L., Bombelli, A., Butler, J., et al. (2010). GEO Carbon
1034 Strategy, GEO Secretariat Geneva/FAO, Rome, 48 pp.

1035 Cloude, S. R., and Pottier, E. (1996). A review of target decomposition theorems in radar polarimetry,
1036 IEEE Trans. Geosci. Remote Sens., 34(2), 498–518.

1037 Cloude, S. R., and Papathanassiou, K. P. (1998). Polarimetric SAR interferometry, IEEE Trans.
1038 Geosci. Remote Sensing, 36(5), 1551-1565.

1039 Cloude S. R. and Papathanassiou, K. P. (2003), Three-stage inversion process for polarimetric SAR
1040 interferometry, IEE Proc. Radar, Sonar and Navigation, 150(3), 125-134.

1041 Conradsen, K., Nielsen, A. A., Schou, J., and Skriver, H. (2003). A test statistic in the complex
1042 Wishart distribution and its application to change detection in polarimetric SAR data, IEEE Trans.
1043 Geosci. Remote Sensing, 41(1), 4-19.

1044 Conradsen, K., Nielsen, A. A., and Skriver, H. (2016). Determining the points of change in time series
1045 of polarimetric SAR data, *IEEE Trans. Geosci. Remote Sensing*, 54(5), 3007-3024.

1046 Dall, J., Nielsen, U., Kusk, A., van de Wal, R.S.W. 2013. Ice flow mapping with P-band SAR, *Proc.*
1047 *Int Geosci. Remote Sensing Symp. (IGARSS 2013)*, Melbourne.

1048 Dubois-Fernandez, P., Le Toan, T., Daniel, S., Oriot, H., Chave, J., Blanc, L., et al. (2012). The
1049 TropiSAR airborne campaign in French Guiana: Objectives, description and observed temporal
1050 behavior of the backscatter signal, *IEEE Trans. Geosci. Remote Sensing*, 50(8), 3228-3241.

1051 Elachi, C., Roth, L. E., and Schaber, G. G. (1984). Spaceborne radar sub-surface imaging in hyperarid
1052 regions, *IEEE Trans. Geosci. Remote Sensing*, vol. GE-22, pp. 383-388,.

1053 European Space Agency (2008). BIOMASS: Candidate Earth Explorer Core Missions - Reports for
1054 Assessment; ESA SP-1313-2, Mission Science Division, ESA-ESTEC, Noordwijk, the Netherlands,
1055 ISSN 0379-6566, 122 pp.

1056 European Space Agency (2012). Report for Mission Selection: Biomass. Science authors: Quegan, S.,
1057 Le Toan T., Chave, J., Dall, J., Perrera, A., Papathanassiou, et al., ESA SP 1324/1 (3 vol. series),
1058 European Space Agency, Noordwijk, the Netherlands, pp. 193.

1059 European Space Agency (2015). Biomass Mission Requirements Document, EOP-SM/1645.

1060 Exbrayat, J.-F., Bloom, A. A., Falloon, P., Ito, A., Smallman, T. L., & Williams, M. (2018a).
1061 Reliability ensemble averaging of 21st century projections of terrestrial net primary productivity
1062 reduces global and regional uncertainties. *Earth System Dynamics*, 9(1), 153–165,
1063 <https://doi.org/10.5194/esd-9-153-2018>.

1064 Exbrayat, J.- F., Luke Smallman, T., Anthony Bloom, A., Hutley, L. B., & Williams, M.
1065 (2018b). Inverse determination of the influence of fire on vegetation carbon turnover in the
1066 pantropics. *Global Biogeochemical Cycles*, 32, 1776–1789. <https://doi.org/10.1029/2018GB005925>.

1067 FAO. (2006). *Global Forest Resources Assessment 2005*. FAO Forestry Paper 147, United Nations
1068 Food and Agriculture Organization, Rome, Italy.

1069 FAO (2008). UN Collaborative Programme on Reducing Emissions From Deforestation And Forest
1070 Degradation in Developing Countries (UN-REDD). FAO, UNDP, UNEP.

1071 FAO (2009) Assessment of the status of the development of the standards for the Terrestrial Essential
1072 Climate Variables, GTOS Secretariat, UN Food and Agriculture Organisation, Rome, Italy.

1073 FAO. (2010). Global Forest Resources Assessment 2010, United Nations Food and Agriculture
1074 Organization, Rome, Italy. ISBN 978-92-5-106654-6.

1075 FAO (2016). Global Forest Resources Assessment 2015 Second Edition, Food and Agriculture
1076 Organization of the United Nations, Rome, ISBN 978-92-5-109283-5.

1077 FAO (2012). Global Ecological Zones for FAO Forest Reporting: 2010 Update. Forest Resources
1078 Assessment Working Paper 179, Food and Agriculture Organisation of the United Nations, Rome,
1079 Italy.

1080 Fransson, J. E. S., Walter, F., and Ulander, L. M. H. (2000). Estimation of forest parameters using
1081 CARABAS-II VHF SAR data, IEEE Trans. Geosci. Remote Sens., 38(2), 720–727.

1082 Freeman, A., and Durden, S. (1998). A three-component scattering model for polarimetric SAR data,
1083 IEEE Trans. Geosci. Remote Sens., 36(3), 963–973.

1084 Friend, A. D., Lucht, W., Rademacher, T. T., Keribin, R. M., Betts, R., et al. (2014). Carbon residence
1085 time dominates uncertainty in terrestrial vegetation responses to future climate and atmospheric CO₂.
1086 Proceedings of the National Academy of Sciences of the United States of America, 111, 3280 – 3285.

1087 Garestier, F., Dubois-Fernandez, P. C., and Papathanassiou, K. P. (2008). Pine forest height inversion
1088 using single-pass X-Band Pol-InSAR data, IEEE Trans. Geosci. Remote Sensing, 46(1), 59-68.

1089 GCOS (2015). Status of the Global Observing System for Climate, GCOS-195, WMO, Geneva,
1090 http://www.wmo.int/pages/prog/gcos/Publications/GCOS-195_en.pdf.

1091 GCOS (2017). The Global Observing System for Climate: implementation needs, GCOS-200, WMO,
1092 Geneva.

1093 Gray, A.L., Mattar, K.E., and Vachon, P.W. (1998). InSAR results from the RADARSAT Antarctic

1094 mapping mission data: estimation of data using a simple registration procedure, Proc. Int Geosci.
1095 Remote Sensing Symp. (IGARSS 1998), Seattle.

1096 Hajnsek I., Scheiber, R., Ulander, L., Gustavsson, A., Sandberg, G., Tebaldini, S., et al. (2008).
1097 BIOSAR 2007: Technical Assistance for the Development of Airborne SAR and Geophysical
1098 Measurements during the BioSAR 2007 Experiment, Final Report, ESA contract No.:
1099 20755/07/NL/CB.

1100 Hajnsek, I., Scheiber, R., Keller, M., Horn, R., Lee, S., Ulander, L., et al. (2009). BIOSAR 2008: Final
1101 Report, ESTEC Contract 22052/08/NL/CT-002, 302 pp.

1102 Hajnsek, I., Kugler, F., Lee, S.K., and Papathanassiou, K.P. (2009). Tropical forest parameter
1103 estimation by means of Pol-InSAR: The INDREX-II campaign, IEEE Trans. Geosci. Remote Sensing
1104 47(2), 481-493.

1105 Hansen, M. C., Potapov, P. V., Moore, R., Hancher, M., Turubanova, S. A., Tyukavina, A., et al.
1106 (2013). High-resolution global maps of 21st-century forest cover change, Science, 15(342), Issue
1107 6160, 850-853, doi: 10.1126/science.1244693.

1108 Ho Tong Minh, D., Tebaldini, S., Rocca, F., Albinet, C., Borderies, P., Koleček, T., et al. (2012).
1109 Tropiscat: multi-temporal multi-polarimetric tomographic imaging of tropical forest, Proc. 2012 IEEE
1110 International Geosci. Remote Sensing Symp., Munich, 22-27 July 2012, 7051-7054.

1111 Ho Tong Minh, D., Le Toan, T., Rocca, F., Tebaldini, S., d'Alessandro, M. M., and Villard, L.
1112 (2014). Relating P-band Synthetic Aperture Radar tomography to tropical forest biomass, IEEE Trans
1113 Geosci. Remote Sensing, 52(2), 967-979.

1114 Ho Tong Minh, D., Le Toan, T., Rocca, F., Tebaldini, S., Villard, L., Réjou-Méchain, M., Phillips,
1115 O.L., Feldpausch, T.R., Dubois-Fernandez, P., Scipal, K., Chave, J. (2016). SAR tomography for the
1116 retrieval of forest biomass and height: Cross-validation at two tropical forest sites in French Guiana,
1117 Remote Sensing of Environment, 175, 138-147.

1118 IPCC (2007). IPCC Fourth Assessment Report: Climate Change 2007, The Physical Science Basis.

1119 Cambridge University Press, Cambridge, UK.

1120 IPCC (2013). Climate Change 2013: The Physical Science Basis. Contribution of Working Group I to
1121 the Fifth Assessment Report of the Intergovernmental Panel on Climate Change (Stocker, T. F., D.
1122 Qin, G.-K. Plattner, M. Tignor, S. K. Allen, J. Boschung, A. Nauels, Y. Xia, V. Bex and P. M.
1123 Midgley (eds.)). Cambridge University Press, Cambridge, United Kingdom and New York, NY, USA,
1124 1535 pp.

1125 Kim, J.-S., Papathanassiou, K., Scheiber, R., and Quegan, S. (2015). Correction of ionospheric
1126 scintillation induced distortions on polarimetric SAR data, *IEEE Trans. Geosci. Remote Sensing*, doi:
1127 10.1109/TGRS.2015.2431856.

1128 Koleček, T., Borderies, P., Rocca, F., Albinet, C., Ho Tong Minh, D., Tebaldini, S., Hamadi, A., et al.
1129 (2012). TropiSCAT: A polarimetric and tomographic scatterometer experiment in French Guiana
1130 forests, *Proc. 2012 IEEE International Geosci. Remote Sensing Symp.*, Munich, 22-27 July 2012,
1131 7597-7600, doi: [10.1109/IGARSS.2012.6351869](https://doi.org/10.1109/IGARSS.2012.6351869)

1132 Kugler, F., Schulze, D., Hajnsek, I., Pretzsch, H., Papathanassiou, K. P. (2014). TanDEM-X Pol-
1133 InSAR performance for forest height estimation, *IEEE Trans. Geosci. Remote Sensing*, 52(10), 6404-
1134 6422.

1135 Kugler, F., Lee, S-K., Papathanassiou, K. P. (2015). Forest height estimation by means of Pol-InSAR
1136 data inversion: the role of the vertical wavenumber, *IEEE Trans. Geosci. Remote Sensing*, 53(10),
1137 5294-5311

1138 Kwok, R., Siegert, M.J., Carsey, F.D. (2000). Ice motion over Lake Vostok, Antarctica: constraints on
1139 inferences regarding the accreted ice, *Journal of Glaciology*, 46(155), 689-694.

1140 Labrière, N., Tao, S., Chave, J., Scipal, K., Le Toan, T., Abernethy, K., et al. (2018). In situ reference
1141 datasets from the TropiSAR and AfriSAR campaigns in support of upcoming spaceborne biomass
1142 missions, *IEEE Jnl. Selected Topics in Applied Earth Observations and Remote Sensing*, 11(10),
1143 3617-3627, doi: [10.1109/JSTARS.2018.2851606](https://doi.org/10.1109/JSTARS.2018.2851606).

1144 Le Quéré, C., Andrew, R. M., Friedlingstein, P., Sitch, S., Pongratz, J., Manning, A. C., et al. (2018).
1145 Global Carbon Budget 2017, *Earth Syst. Sci. Data*, 10, 405-448, doi: 10.5194/essdd-2017-123.

1146 Le Toan T., Quegan, S., Davidson, M., Balzter, H., Paillou, P., Papathanassiou, K., et al. (2011). The
1147 BIOMASS mission: Mapping global forest biomass to better understand the terrestrial carbon cycle,
1148 *Remote Sens. Env.*, 115, 2850–2860.

1149 Ledo, A., Paul, K. I., Burslem, D. F., Ewel, J. J., Barton, C., Battaglia, M., et al. (2018). Tree size and
1150 climatic water deficit control root to shoot ratio in individual trees globally, *New Phytologist*, 217(1),
1151 8-11.

1152 Lee, J.-S., Schuler, D., and Ainsworth, T. (2000). Polarimetric SAR data compensation for terrain
1153 azimuth slope variation, *IEEE Trans Geosci. Remote Sensing*, 38(5), 2153–2163.

1154 Lee, S.-K., Kugler, F., Papathanassiou, K. P., and Hajnsek, I. Quantification of temporal decorrelation
1155 effects at L-band for polarimetric SAR interferometry applications (2013). *IEEE Jnl. Selected Topics*
1156 *in Applied Earth Observations and Remote Sensing*, 6(3), 1351-1367.

1157 Lefsky, M. A., Harding, D. J., Keller, M., Cohen, W. B., Carabajal, C., Del Bom Espirito-Santo, F., et
1158 al. (2005). Estimates of forest canopy height and aboveground biomass using ICESat. *Geophysical*
1159 *Research Letters* 32, L22S02, doi:10.1029/2005GL023971.

1160 Lefsky, M. A. (2010). A global forest canopy height map from the Moderate Resolution Imaging
1161 Spectroradiometer and the Geoscience Laser Altimeter System, *Geophysical Research Letters* 37(15),
1162 doi.org/10.1029/2010GL043622

1163 Li, Z., Quegan, S., Chen, J., and Rogers, N. C. (2015). Performance analysis of Phase Gradient
1164 Autofocus for compensating ionospheric scintillation in BIOMASS P-band SAR data, *IEEE Trans.*
1165 *Geosci. Remote Sensing Letts.*, 12(6), 1367-1371, doi: 10.1109/LGRS.2015.2402833.

1166 Mariotti d'Alessandro, M., Tebaldini, S., Quegan, S., Soja, M. J., Ulander, L. M. H. (2018).
1167 Interferometric ground notching, *Proc. Int Geosci. Remote Sensing Symp. (IGARSS 2018)*, Valencia.

1168 Mariotti d'Alessandro, M. and Tebaldini, S. (2018). Retrieval of terrain topography in tropical forests
1169 using P-band SAR tomography, Proc. Int Geosci. Remote Sensing Symp. (IGARSS 2018), Valencia.

1170 Mariotti d'Alessandro, M., Tebaldini, S., and Rocca, F. (2013). Phenomenology of ground scattering
1171 in a tropical forest through polarimetric synthetic aperture radar tomography, IEEE Trans. Geosci.
1172 Remote Sensing, 51(8), 4430-4437.

1173 Meyer, V., Saatchi, S., Clark, D. B., Keller, M., Vincent, G., et al. (2018). Canopy area of large trees
1174 explains aboveground biomass variations across neotropical forest landscapes, Biogeosciences, 15,
1175 3377–3390.

1176 Massonnet, D., Rossi, M., Carmona, C., Adragna, F., Peltzer, G., Feigl, K., Rabaute, T. (1993). The
1177 displacement field of the Landers earthquake mapped by radar interferometry, Nature, 364, 138-142.

1178 McCauley, J. F., Schaber, G. G., Breed, C. S., Grolier, M. J., Haynes, C. V., Issawi, B., et al. (1982).
1179 Sub-surface valleys and geoarchaeology of the eastern Sahara revealed by Shuttle Radar, Science,
1180 218, pp. 1004-1020,.

1181 Michel, R. & Rignot, E. (1999). Flow of Glacier Moreno, Argentina, from repeat-pass Shuttle
1182 Imaging Radar images: comparison of the phase correlation method with radar interferometry.
1183 Journal of Glaciology, 45(149), 93–100.

1184 Mitchard, E. T. A., Saatchi, S. S., Woodhouse, I. H., Nangendo, G., Ribeiro, N. S., and Williams, M.
1185 (2009). Using satellite radar backscatter to predict above-ground woody biomass: A consistent
1186 relationship across four different African landscapes, Geophys. Res. Lett., 36, Article L23401,
1187 doi:[10.1029/2009GL040692](https://doi.org/10.1029/2009GL040692).

1188 Mitchard, E. T. A., Saatchi, S. S., Baccini, A., Asner, G. P., Goetz, S. J., Harris, N. L., et al., (2013).
1189 Uncertainty in the spatial distribution of tropical forest biomass: a comparison of pan-tropical maps.
1190 Carbon Balance and Management, 8(10), doi:10.1186/1750-0680-8-10.

1191 Mitchard, E. T. A., Feldpausch, T. R., Brienen, R. J. W., Lopez-Gonzalez, G., Monteagudo, A.,
1192 Baker, T. R., et al., (2014). Markedly divergent estimates of Amazon forest carbon density from
1193 ground plots and satellites. Global Ecol. Biogeogr., 23(8), 836-955, doi: 10.1111/geb.12168.

1194 Mokany, K., Raison, R.J., and Prokushkin, A.S. (2006). Critical analysis of root:shoot ratios in
1195 terrestrial biomes. *Global Change Biology*, 12(1), 84-96.

1196 Monteith, A. R., and Ulander, L. M. H. (2018). Temporal survey of P- and L-band polarimetric
1197 backscatter in boreal forests, *IEEE Jnl. Selected Topics in Applied Earth Observations and Remote*
1198 *Sensing*, 11(10), 3564 – 3577.

1199 Paillou, P., Grandjean, G., Baghdadi, N., Heggy, E., August-Bernex, T., and Achache, J. (2003). Sub-
1200 surface imaging in central-southern Egypt using low frequency radar: Bir Safsaf revisited, *IEEE*
1201 *Trans. Geosci. Remote Sensing*, 41(7), 1672-1684.

1202 Paillou, P., Reynard, B., Malézieux, J.-M, Dejax, J., Heggy, E., Rochette, P., et al. (2006). An
1203 extended field of crater-shaped structures in the Gilf Kebir region – Egypt: Observations and
1204 hypotheses about their origin, *Jnl. African Earth Sciences*, 46, 281-299.

1205 Paillou, P., Schuster, M., Tooth, S., Farr, T., Rosenqvist, A., Lopez, S., et al. (2009). Mapping of a
1206 major paleodrainage system in Eastern Libya using orbital imaging Radar: The Kufrah River, *Earth*
1207 *and Planetary Science Letters*, 277, 327-333, doi: 10.1016/j.epsl.2008.10.029.

1208 Paillou, P., Lopez, S., Farr, T. and Rosenqvist, A. (2010). Mapping sub-surface geology in Sahara
1209 using L-band SAR: first results from the ALOS/PALSAR imaging radar, *IEEE Journal of Selected*
1210 *Topics in Earth Observations and Remote Sensing*, 3(4), 632-636.

1211 Paillou, P., Ruault du Plessis, O., Coulombeix, C., Dubois-Fernandez, P., Bacha, S., Sayah, N., et al.
1212 (2011). The TUNISAR experiment: flying an airborne P-band SAR over southern Tunisia to map sub-
1213 surface geology and soil salinity,” *PIERS 2011, Marrakesh, Morocco*.

1214 Paillou, P., Tooth, S., and Lopez, S. (2012). The Kufrah paleodrainage system in Libya: a past
1215 connection to the Mediterranean Sea?, *C.R. Geoscience*, 344, 406-414.

1216 Paillou, P. (2017). Mapping palaeohydrography in deserts: contribution from space-borne imaging
1217 radar, *Water*, 9(194).

1218 Paillou, P. Dubois-Fernandez, P., Lopez, S., and Touzi, R. (2017). SAR polarimetric scattering
1219 processes over desert areas: Ksar Ghilane, Tunisia, POLINSAR, Frascati, Italy.

- 1220 Pan, Y., Birdsey, R.A., Fang, J., Houghton, R., Kauppi, P.E., Kurz, W. A., et al. (2011). A large and
1221 persistent carbon sink in the world's forests. *Science*, 333, 988-993.
- 1222 Papathanassiou, K. P., Cloude, S. R. (2001). Single-baseline polarimetric SAR interferometry. *IEEE*
1223 *Trans. Geosci. Remote Sensing*, 39(11), 2352-2363.
- 1224 Persson, H. J., Olsson, H., Soja, M. J., Ulander, L. M. H., and Fransson, J. E. S. (2017). Experiences
1225 from large-scale forest mapping of Sweden using TanDEM-X data, *Remote Sensing*, 9 (12),
1226 doi:10.3390/rs9121253.
- 1227 Philip, M.S. (1994). *Measuring Trees and Forests*, Second Edition, CAB International, Oxon, UK.
- 1228 Praks, J., Kugler, F., Papathanassiou, K. P., Hajnsek, I., Hallikainen, M. (2007). Tree height
1229 estimation for boreal forest by means of L- and X-band Pol-InSAR and HUTSCAT scatterometer,
1230 *IEEE Trans. Geosci. Remote Sensing Letts.*, 37(3), 466–470.
- 1231 Quegan, S., Lomas, M., Papathanassiou, K. P., Kim, J-S., Tebaldini, S., Giudici, D., et al. (2018).
1232 Calibration challenges for the BIOMASS P-band SAR instrument, *Proc. IEEE Int. Geosci. Remote*
1233 *Sensing Symp. (IGARSS 2018)*, Valencia.
- 1234 Rackham, O., & Moody, J. (1996). *The making of the Cretan landscape*. Manchester University Press.
- 1235 Rodriguez, E., Morris, C. S., Belz, J. E., Chapin, E. C., Martin, J. M., Daffer, W., et al. (2005). An
1236 assessment of the SRTM topographic products, Technical Report JPL D-31639, Jet Propulsion
1237 Laboratory, Pasadena, California.
- 1238 Radkau, J. (2012). *Wood: a history (Vol. 17)*. Polity.
- 1239 Rignot, E. (2008). Changes in West Antarctic ice stream dynamics observed with ALOS PALSAR
1240 data, *Geophysical Research Letters* **35**, L12505, doi:10.1029/2008GL033365, 1–5.
- 1241 Rogers, N. C., Quegan, S., Kim, J. S. and Papathanassiou, K. P. (2013). Impacts of ionospheric
1242 scintillation on the BIOMASS P-band satellite SAR, *IEEE Trans. Geosci. Remote Sensing*, 52(1), doi:
1243 10.1109/TGRS.2013.2255880.

1244 Rogers, N. C., and Quegan, S. (2014). The accuracy of Faraday rotation estimation in satellite
1245 Synthetic Aperture Radar images, *IEEE Trans. Geosci. Remote Sensing*, 52(8), 4799 – 4807, doi:
1246 [10.1109/TGRS.2013.2284635](https://doi.org/10.1109/TGRS.2013.2284635)

1247 Rosenqvist, A., Shimada, M., Suzuki, S., Ohgushi, F., Tadono, T., Watanabe, M., et al. (2014).
1248 Operational performance of the ALOS global systematic acquisition strategy and observation plans
1249 for ALOS-2 PALSAR-2, *Remote Sens. Env.* 155, 3-12, doi.org/10.1016/j.rse.2014.04.011.

1250 Ru, X., Liu, Z., Huang, Z., and Jiang, W. (2016). Normalized residual-based constant false-alarm rate
1251 outlier detection. *Pattern Recognition Letters*, 69, 1-7.

1252 Ryan C. M., Hill T. C., Woollen E., Ghee C., Mitchard E. T. A. , Cassells G, Grace J, Woodhouse IH,
1253 Williams M. (2012). Quantifying small-scale deforestation and forest degradation in African
1254 woodlands using radar imagery. *Global Change Biology* 18, 243-257.

1255 Saatchi, S., Marlier, M., Chazdon, R. L., Clark, D B., and Russell, A. (2011). Impact of spatial
1256 variability of tropical forest structure on radar estimation of aboveground biomass, *Remote Sensing of*
1257 *Environment*, 115(11), 2836-2849, doi.org/10.1016/j.rse.2010.07.015.

1258 Saatchi, S. S., Harris, N. L., Brown, S., Lefsky, M., Mitchard, E. T. A., Salas, W., et al., (2011).
1259 Benchmark map of forest carbon stocks in tropical regions across three continents, *Proceedings of the*
1260 *National Academy of Sciences*, **108** (24), 9899–9904.

1261 Sandberg, G., Ulander, L. M. H., Holmgren, J., Fransson, J. E. S., & Le Toan, T. (2011). L- and P-
1262 band backscatter intensity for biomass retrieval in hemiboreal forest, *Remote Sensing of the*
1263 *Environment* 115, 2874-2886.

1264 Sandberg, G., Ulander, L. M. H., Wallerman, J., and Fransson, J.E.S. (2014). Measurements of forest
1265 biomass change using P-band SAR backscatter, *IEEE Trans. Geosci. Remote Sensing*, 52(10), 6047-
1266 6061.

1267 Santoro, M., Beer, C., Cartus, O., Schmullius, C., Shvidenko, A., McCallum, I., et al. (2011).
1268 Retrieval of growing stock volume in boreal forest using hyper-temporal series of Envisat ASAR
1269 ScanSAR backscatter measurements. *Remote Sens. Environ.*, 115(2), 490-507.

1270 Santoro, M., Cartus, O., Fransson, J. E. S., Shvidenko, A. , McCallum, I., Hall, R. J., et al. (2013).
1271 Estimates of forest growing stock volume for Sweden, Central Siberia and Québec using Envisat
1272 Advanced Synthetic Aperture Radar backscatter data. *Remote Sensing*, 5(9), 4503-4532.

1273 Scharf, L. L. (1991). *Statistical signal processing: detection, estimation, and time series analysis*.
1274 [Boston: Addison-Wesley. ISBN 0-201-19038-9.](#)

1275 Schimel, D., Pavlick, R., Fisher, J.B., Asner, G.P., Saatchi, S. S., Townsend, P., et al. (2015).
1276 Observing terrestrial ecosystems and the carbon cycle from space, *Global Change Biology*, 21, 1762-
1277 1776.

1278 Schmullius, C., Matejka, E., Pathe, C., Santoro, M., Cartus, O., Wiesmann, A., et al. (2017). DUE
1279 GlobBiomass Final Report, ESA-ESRIN Contract No. 4000113100/14/I_NB.

1280 Schlund, M., Scipal, K., and Quegan, S. (2018). Assessment of a power law relationship between P-
1281 band SAR backscatter and aboveground biomass and its implications for BIOMASS mission
1282 performance, *IEEE Jnl. Selected Topics in Applied Earth Observations and Remote Sensing*, 11,
1283 3538-3547, doi: [10.1109/JSTARS.2018.2866868](https://doi.org/10.1109/JSTARS.2018.2866868).

1284 Skonieczny, C., Paillou, P., Bory, A., Bayon, G., Biscara, et al. (2015). African humid periods
1285 triggered the reactivation of a large river system in Western Sahara, *Nature Comm.*, Nov. 10th.

1286 Smallman, T. L., Exbrayat, J.-F., Mencuccini, M., Bloom, A., and Williams, M. (2017). Assimilation
1287 of repeated woody biomass observations constrains decadal ecosystem carbon cycle uncertainty in
1288 aggrading forests, *J. Geophys. Res. Biogeosciences*, 122, 528-545.

1289 Smith-Jonforsen, G., Folkesson, K., Hallberg, B., and Ulander, L. M. H. (2007). Effects of forest
1290 biomass and stand consolidation on P-band backscatter, *IEEE Geosci. Remote Sensing Letts.*, 4(4),
1291 669-673.

1292 Soja, M. J., Sandberg, G., and Ulander, L. M. H. (2013). Regression-based retrieval of boreal forest
1293 biomass in sloping terrain using P-band SAR, *IEEE Trans. Geosci. Remote Sens.*, 51(5), 2646-2665.

1294 Soja, M. J., Askne, J. I. H., and Ulander, L. M. H. (2017). Estimation of boreal forest properties from
1295 TanDEM-X data using inversion of the interferometric water cloud model, *IEEE Geosci. Remote*
1296 *Sensing Letts.*, 14(7), 997-1001.

1297 Soja, M. J., d'Alessandro, M. M., Quegan, S., Tebaldini, S., and Ulander, L. M. H. (2018). Model-
1298 based estimation of tropical forest biomass from notch-filtered P-band SAR backscatter, *Proc. IEEE*
1299 *Int. Geosci. Remote Sensing Symp. (IGARSS 2018)*, Valencia.

1300 Tang, S. (2018). Quantifying Differences in Forest Structures with Quantitative Structure Models
1301 from TLS Data, MSc Thesis, University College London.

1302 Tebaldini, S., Mariotti d'Alessandro, M., Kim, J.-S., Papathanassiou, K. (2017). Ionosphere vertical
1303 profiling from BIOMASS multisquint InSAR, *Proc. IEEE Int. Geosci. Remote Sensing Symp.*
1304 *(IGARSS 2017)*, Fort Worth (USA).

1305 Tebaldini S. and Rocca, F. (2012). Multibaseline polarimetric SAR tomography of a boreal forest at
1306 P- and L-bands, *IEEE Trans. Geosci. Remote Sens.*, 50(1), 232-246.

1307 Thomas, S. C., and Martin, A. R. (2012). Carbon content of tree tissues: a synthesis, *Forests*, 3, 332-
1308 352, doi:10.3390/f3020332.

1309 Thurner, M., Beer, C., Santoro, M., Carvalhais, N., Wutzler, T., Schepaschenko, D., et al. (2014).
1310 Carbon stock and density of northern boreal and temperate forests. *Global Ecology and*
1311 *Biogeography*, 23(3), 297-310.

1312 Thurner, M., Beer, C., Ciais, P., Friend, A.D., Ito, A., et al. (2017). Evaluation of climate-related
1313 carbon turnover processes in global vegetation models for boreal and temperate forests, *Global*
1314 *Change Biology*, 23, 3076–3091.

1315 Treuhaft, R. N., Madsen, S. N., Moghaddam, M., and van Zyl, J. J. (1996). Vegetation characteristics
1316 and underlying topography from interferometric data, *Radio Sci.*, 31, 1449-1495.

1317 Truong-Loi, M.-L., Saatchi, S., and Jaruwatanadilok, S. (2015). Soil moisture estimation under
1318 tropical forests using UHF radar polarimetry, *IEEE Trans. Geosci. Remote Sens.*, 53(4), 1718–1727.

1319 Ulander, L. M. H., Gustavsson, A., Flood, B., Murdin, D., Dubois-Fernandez, P., Dupuis, X., et al.
1320 (2011a). BioSAR 2010: Technical Assistance for the Development of Airborne SAR and Geophysical
1321 Measurements during the BioSAR 2010 Experiment, Final Report, ESA contract no.
1322 4000102285/10/NL/JA/ef.

1323 Ulander, L.M.H., Sandberg, G. & Soja, M.J. (2011b). Biomass retrieval algorithm based on P-band
1324 BioSAR experiments of boreal forest, Proc. 2011 IEEE International Geosci. Remote Sensing Symp.,
1325 Vancouver, Canada, 4245-4248.

1326 Ulander, L. M. H., Monteith, A. R., Soja, M. J., and Eriksson, L. E. B. (2018). Multiport vector
1327 network analyzer radar for tomographic forest scattering measurements, IEEE Geosci. Remote
1328 Sensing Letters, 15(12), 1897 – 1901.

1329 UNFCCC (2016). Key decisions relevant for reducing emissions from deforestation and forest
1330 degradation in developing countries (REDD+), Decision booklet REDD+, UNFCCC secretariat,
1331 February 2016.

1332 Villard, L., and Le Toan, T. (2015). Relating P-band SAR intensity to biomass for tropical dense
1333 forests in hilly terrain: γ^0 or t^0 ?, IEEE Jnl. Selected Topics in Applied Earth Observations and Remote
1334 Sensing, 8(1), 214-223.

1335 Warszawski, L., Frieler, K., Huber, V., Piontek, F., Serdeczny, O., and Schewe, J. (2014). The Inter-
1336 Sectoral Impact Model Intercomparison Project (ISI-MIP): Project framework, PNAS, 111(9), 3228-
1337 3232; <https://doi.org/10.1073/pnas.1312330110>.

1338 Wessel, B., Huber, M., Wohlfart, C., Marschalk, U., Kosmann, D., Roth, A. (2018). Accuracy
1339 assessment of the global TanDEM-X Digital Elevation Model with GPS data, ISPRS Jnl.
1340 Photogrammetry and Remote Sensing, 139, 171–182.

1341 Williams, M, Hill, T.C., and Ryan C.M. (2013). Using biomass distributions to determine probability
1342 and intensity of tropical forest disturbance, Plant Ecology and Diversity, 6, 87-99.

1343 World Bank, Wood-Based Biomass Energy Development for Sub-Saharan Africa: Issues and
1344 Approaches (2011). The International Bank for Reconstruction and Development, The World Bank
1345 Group, Washington, D.C., U.S.A.

1346 Wright, P., Quegan, S., Wheadon, N., and Hall, D. (2003). Faraday rotation effects on L-band
1347 spaceborne SAR data, IEEE Trans. Geosci. Remote Sensing, 41(12), 2735-2744.

1348

1349 **Figure captions**

1350 **Fig. 1.** Global ecological regions of the world (FAO 2012) with the area affected by Space Objects
1351 Tracking Radar (SOTR) stations highlighted in yellow. Only land areas between 65° South and 85°
1352 North are represented (figure reproduced courtesy of Joao Carreiras).

1353 **Fig. 2.** P-band backscatter at HV polarisation (γ_{HV}^0) over tropical and boreal forests against the
1354 biomass of in situ reference plots. Data from Paracou, French Guiana, were acquired by the SETHI
1355 SAR system in 2011 (Dubois-Fernandez et al., 2012), those from La Selva, Costa Rica, in 2004 by the
1356 AIRSAR system (Antonarakis et al., 2011) and those from Remningstorp, Sweden, by the E-SAR
1357 system in 2007 (Sandberg et al., 2011).

1358 **Fig. 3.** Estimated AGB using the approach described in the text against AGB estimated from in situ
1359 and airborne laser scanning at the La Lopé site in Gabon during the AfriSAR campaign. The running
1360 average given by the blue line indicates only a small positive bias across the whole range of AGB.
1361 ROI denotes Region of Interest.

1362 **Fig. 4.** Plot of HV backscatter intensity at height 30 m above the ground measured by tomography
1363 against in situ AGB in 1 ha plots at tropical forest sites investigated during the TropiSAR (Paracou
1364 and Nouragues) and AfriSAR (Lopé, Rabi, Mondah) campaigns.

1365 **Fig. 5.** Forest height map obtained from inverting P-band Pol-InSAR data acquired over the Pongara
1366 National Park, Gabon, in the framework of the AfriSAR campaign in February 2017.

1367 **Fig. 6.** (Top) Pair of repeat-pass PALSAR-2 images acquired on 8 August 2014 and 7 August 2015
1368 displayed in Pauli image format (red = HH + VV; blue = HH - VV; green = 2HV) and slant range

1369 geometry. (Bottom left) Detection of change at 99% significance level; changed pixels are marked as
1370 black. (Bottom right) Image from 8 August 2014 with changed pixels marked as red.

1371 **Fig 7.** Relative difference between modelled carbon turnover rates and turnover rates inferred from
1372 observations. 1.0 means modelled rate is 100% higher (from Thurner et al., 2017). Red boxes labelled
1373 b (boreal) and t (temperate) were analysed further in Thurner et al. (2017) to explain these
1374 discrepancies (figure reproduced courtesy of Martin Thurner).

1375 **Fig. 8.** The relative reduction in the size of the 95% confidence interval of estimated vegetation
1376 carbon turnover times when using a prior value for biomass at each pixel compared to a run without a
1377 biomass prior. Turnover times were estimated using the CARDAMOM system. The darker areas
1378 show where reduction in relative uncertainty is largest.

1379 **Figure 9.** Left: SPOT image of the Ksar Ghilane oasis region in southern Tunisia: palaeo-channels are
1380 hidden by aeolian sand deposits. Middle: ALOS-2 L-band radar image, showing sub-surface features
1381 but blurred by the return from the superficial sand layer. Right: SETHI P-band radar image, clearly
1382 revealing sub-surface hydrological features.

1383 **Fig. 10.** Coverage of ESA and NASA-ISRO satellite measurements of forest structure and above-
1384 ground biomass (AGB). The background shows the global coverage area of NISAR, which will be
1385 sensitive to AGB values < 100 t/ha (green and yellow). BIOMASS coverage includes the tropical belt,
1386 the temperate and boreal zones of Asia, and the southern hemisphere, while the GEDI Lidar will
1387 sample latitudes between $\pm 51.5^\circ$. These two sensors will cover the full range of forest AGB
1388 providing measurements where $AGB > 100$ t/ha (red), so inaccessible to NISAR.

Figure
[Click here to download high resolution image](#)

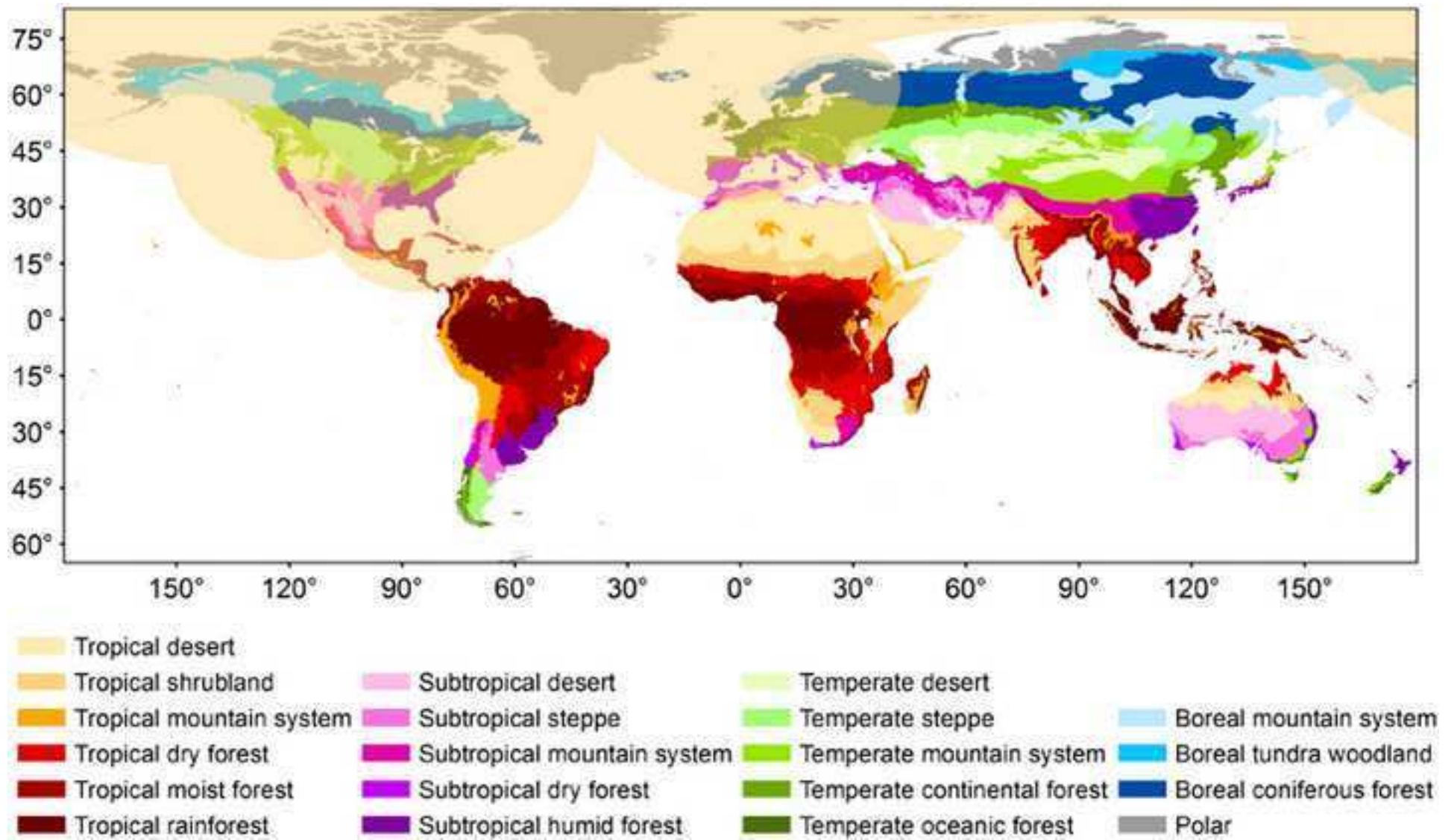
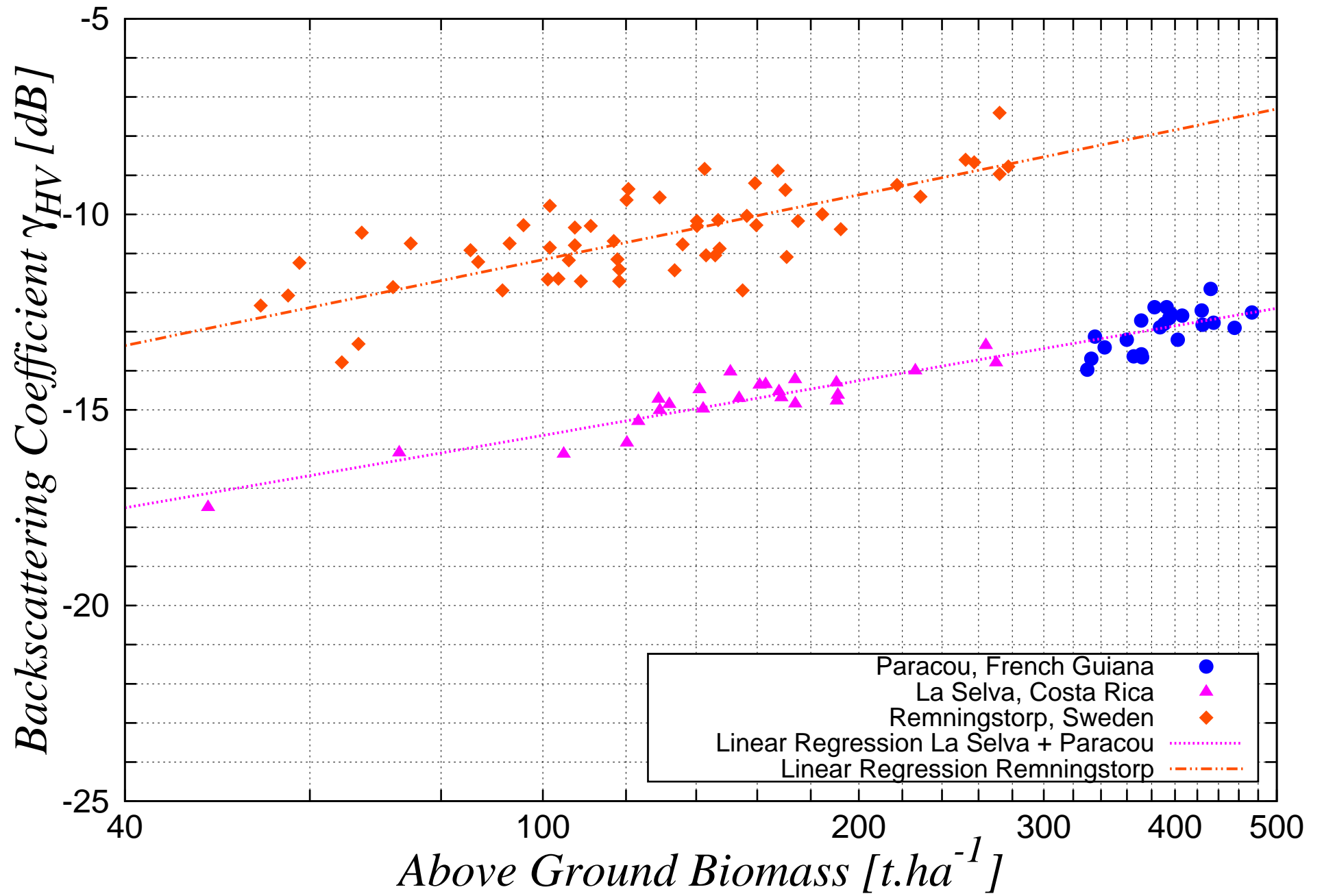


Figure
[Click here to download Figure: figure 2.pdf](#)



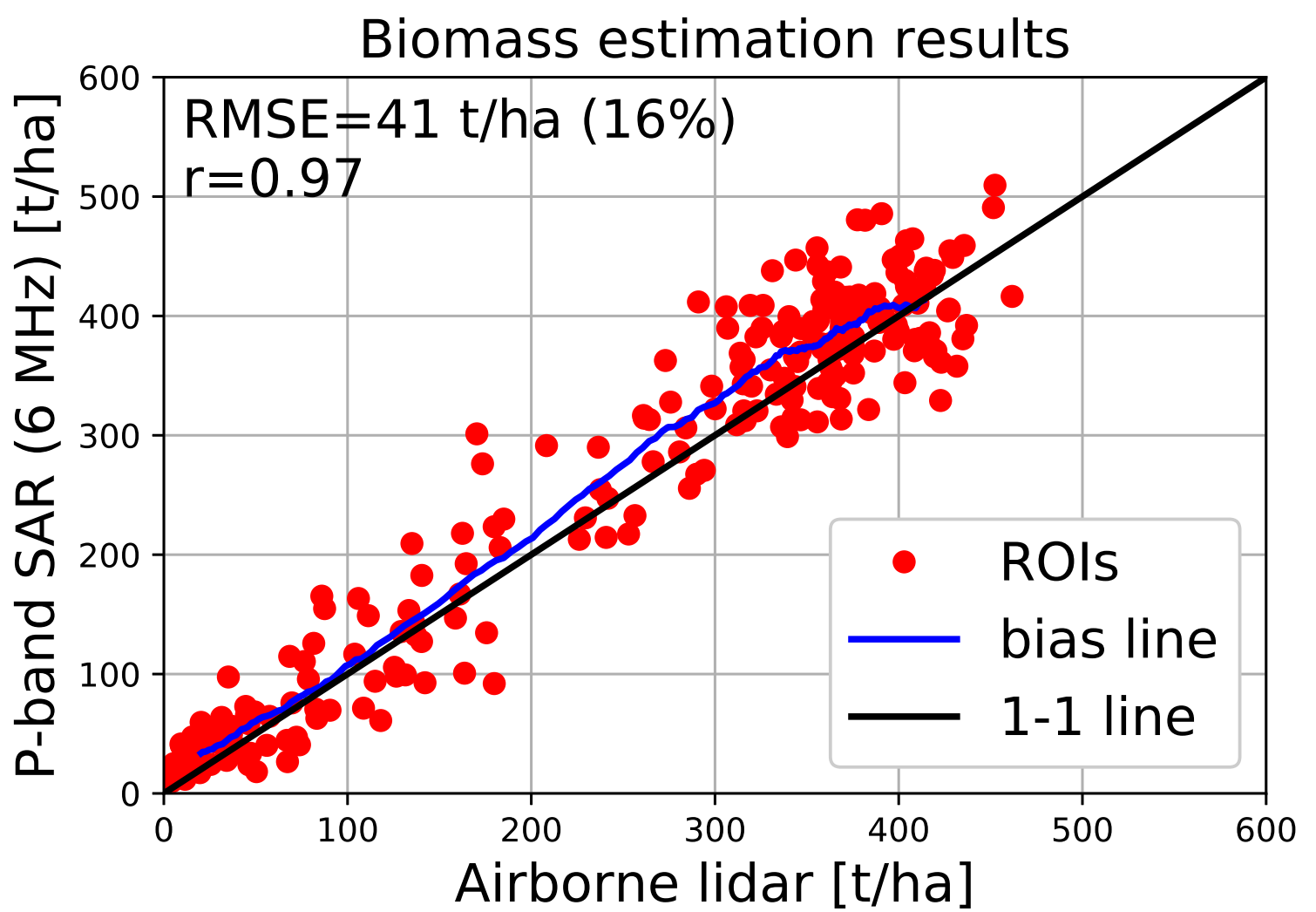


Figure
[Click here to download high resolution image](#)

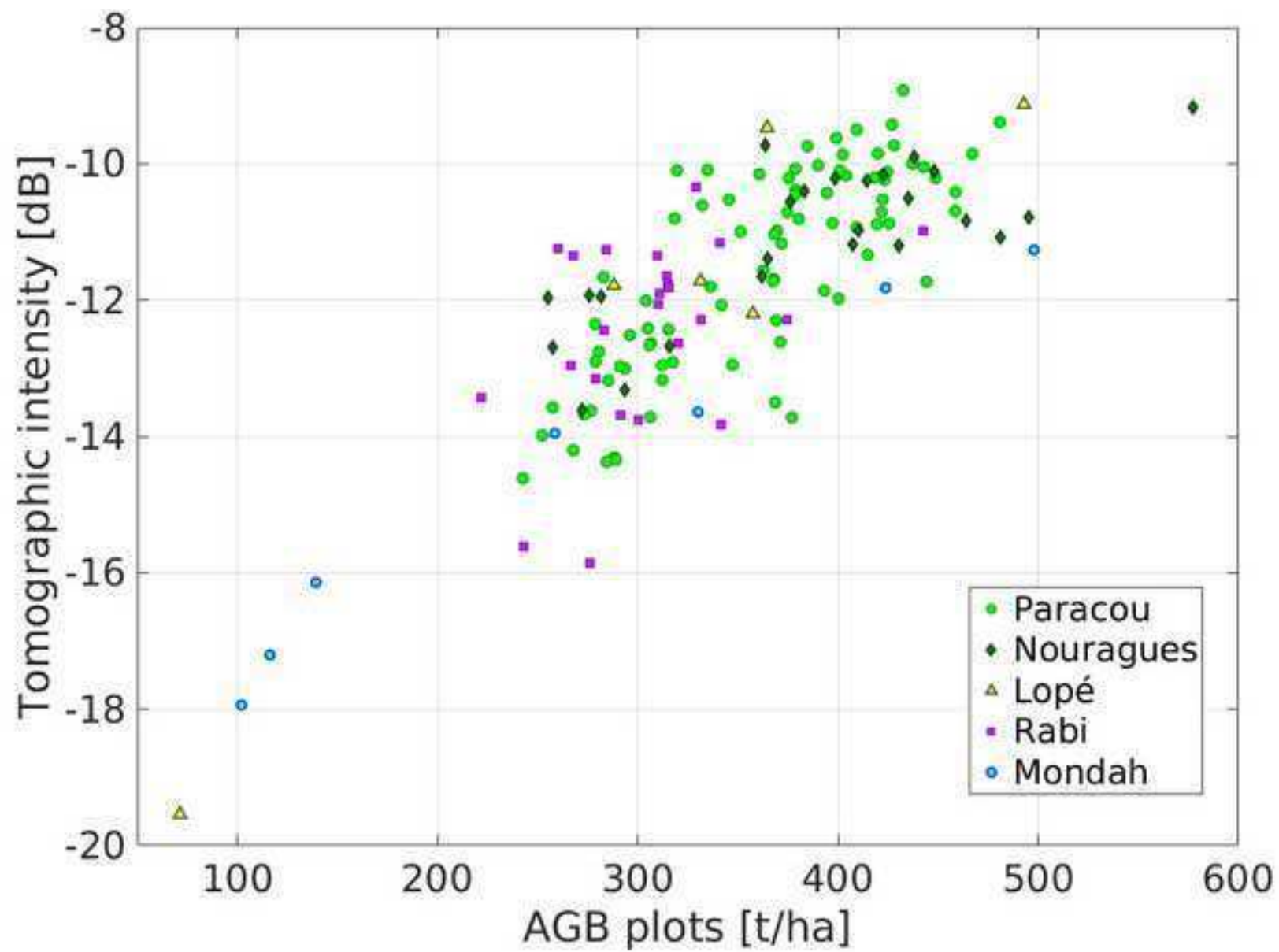
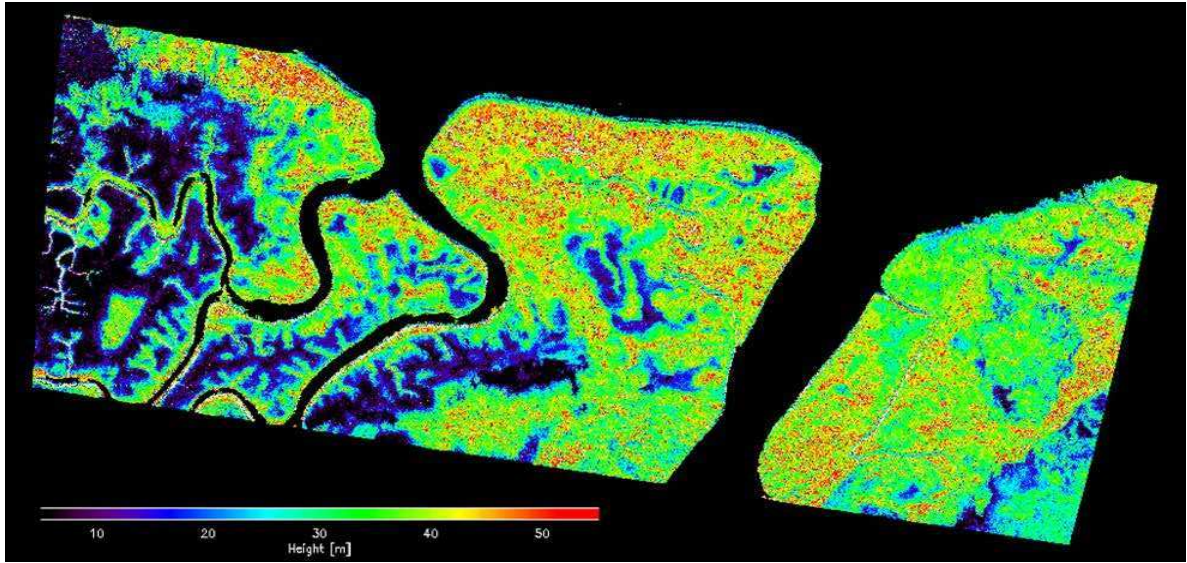


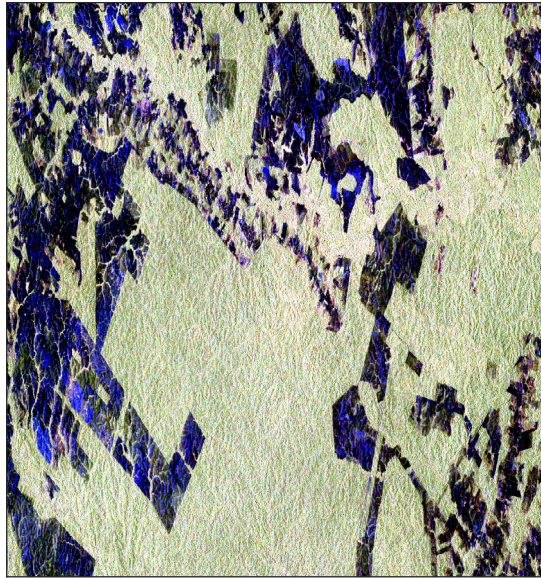
Figure
[Click here to download Figure: figure 5.pdf](#)



Figure

[Click here to download Figure: figure 6.pdf](#)

140808



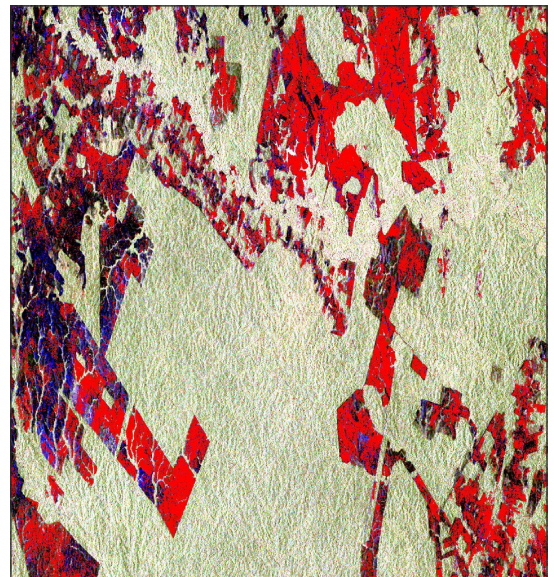
150807



Detection of Change: $P > 99\%$

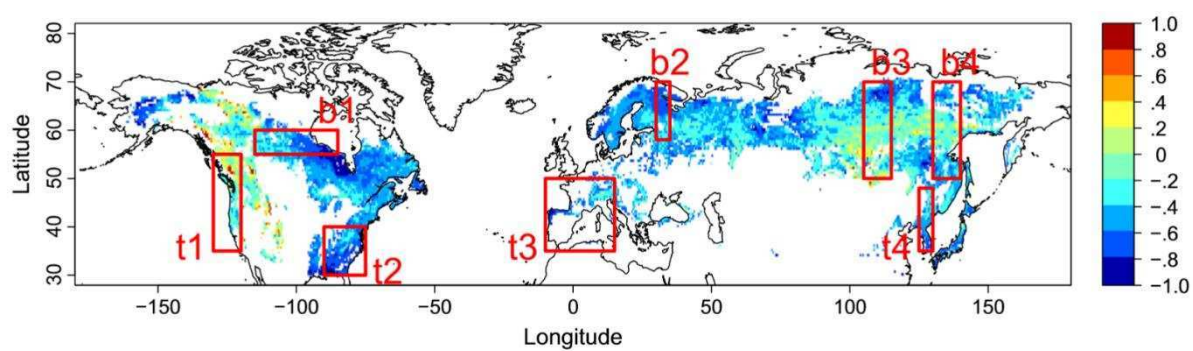


140808 + Change (red mask)



Figure

[Click here to download Figure: figure 7.pdf](#)



Figure

[Click here to download Figure: figure 8.pdf](#)

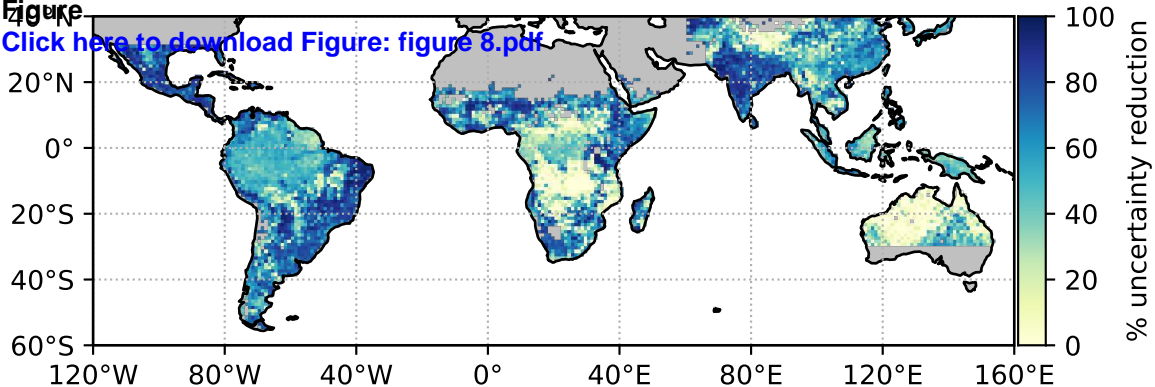
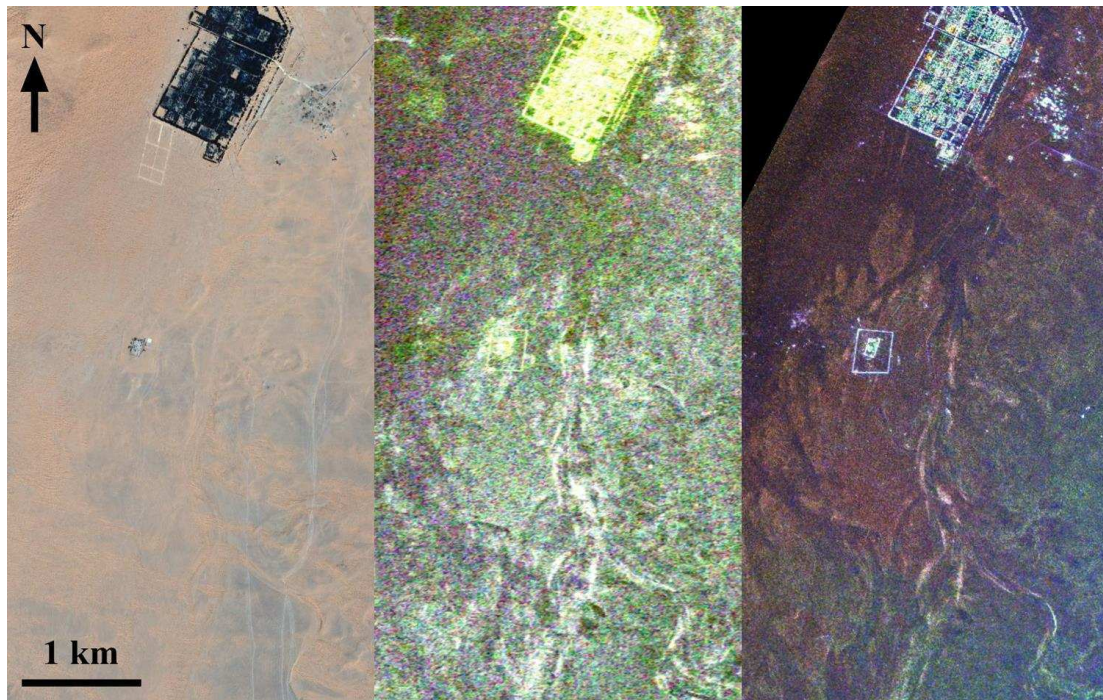


Figure
[Click here to download Figure: figure 9.pdf](#)



Figure

[Click here to download Figure: fig 10.pdf](#)

